

A NUMERICAL STUDY OF A TRIBOLOGICAL EXPERIMENT

Mariana Fernanda Neves da Silva

Dissertation developed at data M Sheet Metal Solutions in Germany and submitted to Faculdade de Engenharia da Universidade do Porto for the degree of Master of Science in Mechanical Engineering

Supervisors:

Dr. Thomas Dietl

Prof. Dr. Abel D. Santos

Co-supervisors:

Dipl.-Ing. Johann Harraßer

ir. André Abee

M.Sc. Miguel Pereira

M.Sc. Pedro Ferreira

Porto, September 2017

Abstract

Environmental awareness and rising energy prices are shaping the industry and demands for more efficient productions are emerging. Energy efficiency and waste reduction are some of the main driving forces of research. Roll forming industry is not an exception and better detection of manufacturing defects during the designing process, tool wear predictions and better set-up of the machine lines are a major concern. COPRA® FEA RF is a software used to simulate roll forming process. An optimisation of the contact representation in the roll forming simulations is fundamental to improve the torque and wear calculations in COPRA® FEA RF. However, in order to develop a good simulation of the contact in roll forming is, first of all, mandatory to understand the contact modelling using the finite element method.

A tribological experiment was modelled using the finite element method. The contact modelling was further investigated with the goal to optimise the FE model of the tribological experiment. The possible contact zone discretisation in the sheet longitudinal and transverse directions was investigated and its influence on the bending geometry and the contact representation was analysed. An analysis on the influence of the thickness discretisation on the bending geometry and contact representation was also performed. Additionally, different locations of the nodes with the roll axis were simulated in order to investigate its influence on the roll torque. Moreover, the different values for the parameters that define the contact search algorithm were considered and its influence on the nodes in contact, roll torque, roll force and the contact normal stress was investigated. Finally, the friction influence on the bending geometry and the contact representation was studied. Additionally, different numerical models were implemented and its influence on the bending geometry and the contact representation was investigated.

It was concluded that the mesh discretisation in the longitudinal and transverse direction has a high influence on the contact normal stress. The thickness discretisation influences the bending geometry, which, in turn, influences the contact representation. The ratio of the element dimensions was also proven to influence the contact normal stress and low aspect ratio elements provided a better representation. On the other hand, the numerical stability was very influenced by the contact search. The roll torque and contact normal stress calculated when the roll starts rotating was influenced by the contact search algorithm. Additionally, the friction influenced mainly the contact representation and has a minimal influence on the bending geometry.

Resumo

A crescente conscientização ambiental e o aumento do preço da energia têm vindo a moldar as necessidades da indústria e produções mais eficientes começam a ser exigidas. A eficiência energética e a redução de desperdícios tornaram-se um dos principais tópicos de investigação nos dias de hoje. A indústria de perfilagem não é exceção e uma melhor antecipação de defeitos de fabricação durante o processo de projeto, melhores previsões de desgaste das ferramentas e uma melhor configuração das linhas de produção são uma crescente preocupação. COPRA® FEA RF é um software usado para simular processos de perfilagem. Uma otimização da representação de contacto nas simulações é fundamental para melhorar os cálculos de momento e desgaste no COPRA® FEA RF. No entanto, para desenvolver uma boa simulação do contacto em perfilagem é necessário compreender a modelação do contacto com o método dos elementos finitos.

Um ensaio tribológico foi modelado usando o método dos elementos finitos e a modelação de contacto foi investigada com o objetivo de otimizar o modelo de elementos finitos. A discretização da possível área em contacto na direção longitudinal e transversal foi investigada e a sua influência na geometria da chapa e na representação do contacto foi analisada. A discretização da espessura da chapa foi também analisada e a sua influência na geometria da chapa e na representação de contacto foram tidas em consideração. Além disso, foram simuladas diferentes localizações dos nós com o eixo do rolo para investigar a sua influência no momento do rolo. Adicionalmente, foram considerados diferentes valores para os parâmetros que definem o algoritmo de deteção de contacto e a foi estudada a sua influência no número de nós em contacto, no momento do rolo, na força do rolo e na tensão normal de contacto. Finalmente, estudou-se a influência da modelação do atrito na geometria da chapa e na representação de contacto. Além disso, foram implementados diferentes modelos numéricos e verificar a sua influência na geometria de flexão e na representação de contacto.

Concluiu-se que a discretização da malha na direção longitudinal e transversal tem uma grande influência na tensão normal de contacto. A discretização da espessura influencia a geometria da chapa, que, por sua vez, influencia a representação do contacto. A proporção das dimensões do elemento também influenciou a tensão normal de contacto e elementos com baixa razão entre os lados proporcionaram melhores resultados. Por outro lado, a estabilidade numérica foi influenciada pela deteção de contacto. O momento do rolo e a tensão normal de contacto calculada no momento em que o rolo começa a rodar foi influenciada pelo algoritmo de deteção de contacto. Além disso, o atrito influenciou a representação do contacto e tem uma influência mínima na geometria da chapa.

Acknowledgments

The research work present in this Master's thesis has been carried out between February and June 2017 at data M Sheet Metal Solutions in Germany. These five months were a very enriching period in my engineering education, as well as in my personal development. The autonomy in the project accompanied by a wise guidance of my supervisors allowed me to improve my knowledge in the field of computational contact mechanics and numerical simulations of roll forming process. Thus, I would like to acknowledge all the people involved.

The company data M Sheet Metal Solutions and Dipl.-Ing. Albert Sedlmaier for the opportunity to develop this Master's Dissertation project at data M Sheet Metal Solutions and for all the support provided. My mentor at the company, Dr. Thomas Dietl, for guiding me through the right path and for the thoughtful advices. ir. André Abee and Dipl.-Ing. Johann Harraßer, for all the advices, help and teaching regarding numerical simulation and data analysis. Pedro Ferreira, M.Sc., and Miguel Pereira, M.Sc., for their all the help setting down in Munich and all the guidance during the internship.

My supervisor at University of Porto, Prof. Dr. Abel Santos, for all the support and encouragement to develop the project at data M SMS, and for his supervision during the writing process.

Dr. Lander Galdos for the discussing about the tribological experiment and for providing the necessary information.

Content

1 Introduction	1
1.1 data M Sheet Metal Solutions	1
1.2 Motivation and project context	2
1.3 Objectives	3
1.4 Project methodology.....	3
1.5 Dissertation structure	3
2 Literature review	5
2.1 Roll forming.....	5
2.2 Contact mechanics	11
2.3 FE contact analysis	21
3 Modelling of the tribological experiment.....	28
3.1 Physical experiment.....	28
3.2 FE numerical model	31
4 Optimisation of the FE model	45
4.1 Model sensitivity to the mesh discretisation.....	45
4.2 Contact search definition	75
4.3 Friction modeling.....	89
4.4 Optimised FE model.....	100
5 Conclusions and future perspectives.....	103
5.1 Conclusions.....	103
5.2 Future perspectives.....	104
6 References.....	106

List of figures

Figure 1.1 - Graphical interface in COPRA® RF.	1
Figure 1.2 - Graphical interface in COPRA® FEA RF. Retrieved from [Lindgren 2015].	1
Figure 2.1 - Forming of the sheet from an undeformed strip to a finished profile. Retrieved from [Halmos 2006].	6
Figure 2.2 - Section of a set of rolls in a roll former. Retrieved from [Marciniak 2002].	6
Figure 2.3 - Final profile and corresponding flower pattern. Retrieved from [Zeng 2009].	7
Figure 2.4 - Continuous strip bent along a line. Retrieved from [Marciniak 2002].	7
Figure 2.5 - Deformation of longitudinal fibres in bending and tension. Retrieved from [Marciniak 2002].	7
Figure 2.6 - Assumed strain distribution in sheet bending. Retrieved from [Marciniak 2002].	8
Figure 2.7 - Stress state on a section through the sheet in plane strain bending. Retrieved from [Marciniak 2002].	9
Figure 2.8 - Transversal (referred as transverse bending in the text) bending of metal strip during roll forming. Retrieved from [Halmos 2006].	9
Figure 2.9 - Additive redundant deformations of the metal strip during roll forming. Retrieved from [Halmos 2006].	9
Figure 2.10 - Design process of a roll forming line; in blue is the traditional process of trial and error; in red, the upgraded process with virtual testing; dashed lines represent the connection between the cycles. Retrieved from [Ferreira 2016].	10
Figure 2.11 - Non-conforming surfaces in contact at O . Retrieved from [Johnson 1985].	11
Figure 2.12 - Forces and moments acting on contact area S . Retrieved from [Johnson 1985].	13
Figure 2.13 - Contact conditions in 2D. Retrieved from [Kim 2015].	15
Figure 2.14 - Three different geometrical conditions of the slave point with respect to the master body.	16
Figure 2.15 - Physical interpretation of the penalty method: (a) initial configuration; (b) configuration after penetration; (c) equilibrium state. Retrieved from [Neto 2014].	18
Figure 2.16 - Application of the penalty method to the frictional contact problem: (a) regularised unilateral contact law; (b) regularised Coulomb's friction law. Adapted from [Neto 2014].	18
Figure 2.17 - Different possibilities to limit the frictional stress; FN denotes the contact normal force and FT denotes the contact tangential force. Retrieved from [Wriggers 2006].	20

Figure 2.18 - Continuous body and its discretised representation using a finite element mesh composed by finite elements and nodes. Retrieved from [Neto 2014].	23
Figure 2.19 - Schematic illustration of different types of contact discretization: (a) Node-to-Node; (b) Node-to-Segment; (c) Segment-to-Segment. Retrieved from [Neto 2014].	23
Figure 2.20 - Contact tolerance and detecting contact. Retrieved from [Kim 2015].	25
Figure 2.21 - The effect of load increment in contact detection. Retrieved from [Kim 2015].	25
Figure 2.22 - Definition of slave and master. Retrieved from [Kim 2015].	26
Figure 2.23 - Contact stress distribution under uniform pressure load. Retrieved from [Kim 2015].	27
Figure 2.24 - Variation of contact stress distribution as a function of block location. Retrieved from [Kim 2015].	27
Figure 3.1 - Longitudinal stress (σ_l) created in the sheet by the roll penetration.	28
Figure 3.2 - An increasing roll force (F_{roll}) applied to the roll creates a longitudinal stress (σ_l) in the sheet; as a result of the contact, a compressive contact normal stress (σ_n) is applied to the sheet.	29
Figure 3.3 - An increasing torque (T_{roll}) is applied to the roll; as a result of the contact, a compressive contact normal stress (σ_n).	29
Figure 3.4 - A constant angular velocity (ω) is applied to the roll; as a result of the contact, a compressive contact normal stress (σ_n) and a contact friction stress (σ_t) is applied to the sheet.	30
Figure 3.5 - Sheet and roll position in the tribotester with the roll force direction marked. Adapted from [Galdos 2017].	30
Figure 3.6 - Tribotester components. Retrieved from [Galdos 2017].	30
Figure 3.7 - Model geometry of the tribological experiment.	31
Figure 3.8 - Global coordinate system directions used in the simulation.	32
Figure 3.9 - Contact normal stress and friction symmetries for a contact with torque.	32
Figure 3.10 - Sheet and roll dimensions.	33
Figure 3.11 - Eight-node hexahedral isoparametric element with the its local coordinate system.	33
Figure 3.12 - Gauss integration points of the eight-node element. Retrieved from [MSC Software 2016b].	35
Figure 3.13 - Nomenclature adopted for he element dimensions.	36
Figure 3.14 - Global mesh discretisation with the different discretisation zones marked.	36

Figure 3.15 - Discretisation of the sheet thickness.....	36
Figure 3.16 - Possible contact zone mesh refinement and correspondent transition.....	37
Figure 3.17 - “Fixed” zone mesh refinement and correspondent transition.....	37
Figure 3.18 - Coarse mesh zone.....	38
Figure 3.19 - Elastic- plastic strain-hardening model of DP1000 used in the simulation in the model.....	39
Figure 3.20 - Boundary conditions assigned to the sheet.....	40
Figure 3.21 - Boundary conditions assigned to the roll during the penetration.....	41
Figure 3.22 - Boundary conditions assigned to the roll during the rotation.....	41
Figure 3.23 - Representation of the contact distance tolerance and contact status for nodes in a different position, using green for nodes in contact, red for non-contacting nodes and blue for penetrating nodes.....	42
Figure 3.24 - Biased contact tolerance.....	42
Figure 3.25 - Friction models and correspondent numerical implementation supported by COPRA® FEA RF.....	43
Figure 3.26 - Friction numerical models available in COPRA® FEA RF. Retrieved from [MSC Software 2016a].....	43
Figure 4.1 - Different discretisations studied for the possible contact zone.....	47
Figure 4.2 - Path used for the longitudinal bending representation.....	47
Figure 4.3 - Path used for the transverse bending representation.....	48
Figure 4.4 - Geometry of the longitudinal bending at the last increment of the penetration for the different mesh sizes.....	48
Figure 4.5 - Geometry of the longitudinal bending zone at the last increment of the penetration for the different mesh sizes; representation for the possible contact zone.....	48
Figure 4.6 - Geometry of the longitudinal bending at the last increment of the penetration for the different mesh sizes; representation for the “fixed” zone.....	48
Figure 4.7 – Geometry of the transverse bending at the last increment of the penetration for the different mesh sizes.....	49
Figure 4.8 - Roll force during the penetration for the different mesh sizes.....	49
Figure 4.9 – Relative error of the contact area (A), maximum contact normal stress (σ_{nmax}), mean contact normal stress (σ_{nmean}) and dynamic torque (Td) using the finer mesh as the reference.....	50
Figure 4.10 - Maximum contact normal stress during the penetration.....	51

Figure 4.11 - Contact normal stress distribution in the contact area for different mesh sized and with the maximum value pointed out; calculated at the last increment of the penetration...	52
Figure 4.12 - Axis used for the contact normal stress graphical representation.....	53
Figure 4.13 - Contact normal stress along the path crossing the nodes with the maximum normal stress.....	53
Figure 4.14 - Simulation computational time of the different sizes used in the possible contact zone.....	54
Figure 4.15 - Symmetry conditions used in the study of the maximum contact normal stress location.....	55
Figure 4.16 - Longitudinal bending geometry for the possible contact zone, at the penetration last increment, using different thickness discretisation and a 0.167 mm mesh size.....	56
Figure 4.17 - Longitudinal bending geometry in the “fixed zone”, at the penetration last increment, using different thickness discretisation and a mesh size of 0.167 mm.....	56
Figure 4.18 - Transverse bending geometry, at the last increment of the penetration, using different thickness discretisation and a mesh size of 0.167 mm.....	57
Figure 4.19 - Roll force during penetration for a mesh size of 0.167 mm.....	57
Figure 4.20 - Maximum contact normal stress during penetration for a mesh size of 0.167 mm and using different thickness discretisations.	58
Figure 4.21 - Contact normal stress at the last increment of the penetration, discretising the thickness into one and six elements and using a 0.167 mm mesh size; the maximum value location is pointed out in black.....	58
Figure 4.22 - Longitudinal bending geometry for the contact zone, at the last increment of the penetration and using six elements through the thickness.	59
Figure 4.23 - Longitudinal bending geometry for the fixed zone, at the last increment of the penetration and using six elements through the thickness.	59
Figure 4.24 - Transverse bending geometry for the contact zone, using a thickness discretisation into six elements; calculated at the penetration last increment.	60
Figure 4.25 - Roll force during penetration using a thickness discretisation into six elements. ...	60
Figure 4.26 - Maximum contact normal stress during penetration using a thickness discretisation of six elements.....	60
Figure 4.27 - Increments studied for the maximum contact normal stress during penetration using a thickness discretisation into six elements.	61
Figure 4.28 - Contact normal stress at increment 55 for 0.0.333 mm and 0.167 mm mesh size, respectively.....	61

Figure 4.29 - Contacting nodes for several increments, around the maximum contact normal stress discontinuity, for a mesh size of 0.333 mm.....	62
Figure 4.30 - Comparison of the contact normal stress for 0.333 mm and 0.167 mm mesh size using six a thickness discretisation into six elements; calculate at the penetration last increment.....	63
Figure 4.31 - Longitudinal bending geometry for the possible contact zone, at last increment of the penetration and using different thickness discretisation.....	64
Figure 4.32 - Longitudinal bending geometry in the “fixed” zone, at last increment of the penetration and using different thickness discretisation.....	64
Figure 4.33 - Transverse bending geometry, at the last increment of the penetration, using different thickness discretisation and a mesh size of 0.333 mm.....	65
Figure 4.34 - Roll force during penetration for a mesh size of 0.33 mm with different thickness discretisations.....	65
Figure 4.35 - Maximum contact normal stress during penetration using a different thickness discretisations.....	65
Figure 4.36 - Contact normal stress at the last increment of the penetration for different thickness discretisation and using a mesh size of 0.333 mm.....	66
Figure 4.37 - Axis used to represent the contact normal stress distribution.	67
Figure 4.38 - Contact normal stress variation for different thickness discretisations.	67
Figure 4.39 - Simulation computational time for the different thickness discretisation.....	68
Figure 4.40 - Sheet discretisation with a transition mesh.....	68
Figure 4.41 - Sheet discretisation with a homogenous fine mesh.....	69
Figure 4.42 - Longitudinal bending geometry for the possible contact zone at the last increment of the penetration.....	69
Figure 4.43 - Longitudinal bending geometry for the “fixed” zone at the last increment of the penetration.....	70
Figure 4.44 - Transverse bending geometry at last increment of the penetration.	70
Figure 4.45 - Roll force during penetration for a mesh with transitions and a homogeneous fine mesh.....	70
Figure 4.46 - Comparison of the maximum contact normal stress during penetration for a homogeneous mesh and a mesh with transitions.....	71
Figure 4.47 - Contact normal stress in the last increment of the penetration, with the maximum value location pointed out.	71

Figure 4.48 - Contact normal stress along a path with origin in the maximum value node.	72
Figure 4.49 - Roll torque during penetration when the roll axis is in line with a line of nodes.	73
Figure 4.50 - Displacement in the longitudinal direction along the sheet centre line on the inner surface at the last increment of the penetration.....	73
Figure 4.51 - Refinement of the mesh in the sheet centre.....	73
Figure 4.52 - Roll torque during penetration when the roll axis is in line with the elements middle plane.....	74
Figure 4.53 - Contact normal stress at the last increment of the penetration for different elements location with the roll axis.	74
Figure 4.54 - Number of nodes in contact during the simulation for different contact distance tolerances.....	76
Figure 4.55 - Number of nodes in contact during the penetration for different contact distance tolerances.....	76
Figure 4.56 - Number of nodes in contact during the roll rotation.	77
Figure 4.57 - Number of nodes in contact during the roll rotation instability.	77
Figure 4.58 - Roll rotation during the simulation.....	78
Figure 4.59 - Roll torque during the simulation.....	78
Figure 4.60 - Roll torque during the roll rotation.....	79
Figure 4.61 - Roll torque during the rotation phase for a contact detection of 0.01.....	79
Figure 4.62 - Roll force during the simulation.	80
Figure 4.63 - Maximum contact normal stress during the simulation.....	80
Figure 4.64 - Maximum contact normal stress during the roll rotation.....	81
Figure 4.65 - Contact normal stress distribution in penetration last increment for different contact distance tolerances.....	81
Figure 4.66 - Contact normal stress distribution in rotation last increment for different contact distance tolerances.....	82
Figure 4.67 - Simulation computational time for different contact distance tolerances.....	83
Figure 4.68 - Number of nodes in contact during the simulation for different bias factors.	84
Figure 4.69 - Number of nodes in contact during the roll rotation for different bias factors.	84
Figure 4.70 - Contact normal stress distribution at increment 140 for different bias factors.....	85
Figure 4.71 - Roll rotation during the simulation for different bias factors.	85
Figure 4.72 - Roll torque during the simulation for different bias factors.....	86

Figure 4.73 - Roll torque during the roll rotation for different bias factors.....	86
Figure 4.74 - Roll torque during the rotation phase for different bias factors.....	86
Figure 4.75 - Roll force during the simulation for different bias factors.....	87
Figure 4.76 - Maximum contact normal stress during the simulation for different bias factors...	87
Figure 4.77 - Maximum contact normal stress during the roll rotation for different bias factors.	88
Figure 4.78 - Contact normal stress distribution in penetration last increment for different bias factors.....	88
Figure 4.79 - Contact normal stress distribution in rotation last increment for different bias factors.....	89
Figure 4.80 - Friction models and correspondent numerical implementation supported by COPRA® FEA RF.....	90
Figure 4.81 - Friction numerical models available in COPRA® FEA RF. Retrieved from [MSC Software 2016a].....	90
Figure 4.82 - Rotation imposed t the roll t the roll during the rotation phase for the friction study.	91
Figure 4.83 - Angular velocity imposed to the roll during the rotation phase for the friction study.	91
Figure 4.84 - Longitudinal bending geometry for the possible contact zone using a model without friction and a bilinear Coulomb model; calculated at the penetration last increment.....	92
Figure 4.85 - Longitudinal bending geometry for the “fixed” zone using a model without friction and a bilinear Coulomb model; calculated at the penetration last increment.....	92
Figure 4.86 – Transverse bending geometry using a model without friction and a bilinear Coulomb model; calculated at the penetration last increment.....	93
Figure 4.87 - Longitudinal bending geometry for the possible contact zone using a model without friction and a bilinear Coulomb model; calculated at the rotation last increment.....	93
Figure 4.88 - Longitudinal bending geometry for the “fixed” zone using a model without friction and a bilinear Coulomb model; calculated at the rotation last increment.....	93
Figure 4.89 – Transverse bending geometry using a model without friction and a bilinear Coulomb model; calculated at the rotation last increment.....	94
Figure 4.90 - Roll force during the simulation for a model without friction and a model with a bilinear Coulomb friction model.....	94

Figure 4.91 - Maximum contact normal stress during the simulation for a model without friction and a model with a bilinear Coulomb friction model.....	95
Figure 4.92 - Contact normal stress distribution for a model without friction and a model with a bilinear Coulomb friction model; calculated at the penetration last increment.	95
Figure 4.93 - Contact normal stress distribution for a model without friction and a model with a bilinear Coulomb friction model; calculated at the rotation last increment.....	96
Figure 4.94 - Arctangent Coulomb friction law implemented in the model.	97
Figure 4.95 - Sliding velocity at the contact area during the rotation.....	97
Figure 4.96 - Roll force during rotation for different friction numerical implementations.....	98
Figure 4.97 - Roll torque during rotation for different friction numerical implementations.....	98
Figure 4.98 - Maximum contact normal stress during rotation for different friction numerical implementations.	99
Figure 4.99 - Contact normal stress distribution for the different friction models; calculated at the rotation last increment.....	99
Figure 4.100 - Contact friction stress distribution for the different friction models; calculated at the rotation last increment.	100
Figure 4.101 - Sheet discretisation in its thickness.	100
Figure 4.102 - Contact zone mesh refinement and correspondent transition.....	101
Figure 4.103 - Sheet centre mesh refinement.	101
Figure 4.104 - Arctangent Coulomb friction law implemented in the model.....	102

List of tables

Table 3.1 - Termination roll force (F_{roll}) for the different roll penetrations.....	29
Table 3.2 - Mechanical properties of DP1000 and friction coefficients [Galdos 2017].	31
Table 3.3 – DP 1000 material properties.....	38
Table 3.4 - DP1000 parameters used for the strain-hardening Swift law.	38
Table 3.5 - Purpose of the boundary conditions assigned to the model.....	41
Table 4.1 - Maximum contact normal stress calculated in the last increment of the penetration using a 0.167 mm mesh size.....	59
Table 4.2 - Roll force and maximum contact normal stress at increment 55.....	61
Table 4.3 - Roll force and maximum contact normal stress of the increments around the maximum contact normal stress discontinuity for 0.333 mm.	62
Table 4.4 - Maximum contact normal stress at the last increment of the penetration for a mesh with thickness discretisation of six elements.....	63
Table 4.5 - Maximum contact normal stress for the different number of elements along the thickness.....	67
Table 4.6 - Maximum contact normal stress at the last increment of the penetration for a mesh with transitions and a homogeneous fine mesh.....	71
Table 4.7 - Maximum contact normal stress for the different contact distance tolerances at the penetration last increment.....	82
Table 4.8 - Maximum contact normal stress for the different contact distance tolerances at the rotation last increment.....	83

List of acronyms

DOF	Degrees of Freedom
FE	Finite Element
FEA	Finite Element Analysis
NTS	Node-to-Segment
2D	Two Dimensional
3D	Three Dimensional
NTN	Node to Node
STS	Segment to Segment

List of symbols

μ_s	Static friction coefficient
μ_d	Dynamic friction coefficient
T_s	Static torque
T_d	Dynamic torque
σ_n	Contact normal stress
σ_l	Longitudinal strain
F_{roll}	Roll force
T_{roll}	Roll torque
w	Displacement in z direction
u	Displacement in x direction
v	Displacement in y direction
$R_{p\ 0.2}$	Yield strength
R_m	Tensile strength
A_{80}	percentage of elongation after fracture
σ_t	Contact friction stress

1 INTRODUCTION

This dissertation project was developed during a five-month internship at data M Sheet Metal Solutions (data M SMS), a company located in the south of Munich, Germany, developing software solutions for the roll forming industry. In this chapter the company is presented, as well as the motivation and dissertation context, the project goals, the followed methodology and the structure adopted for this dissertation.

1.1 DATA M SHEET METAL SOLUTIONS

The company data M Sheet Metal Solutions (data M SMS) is located in Oberlindern, about 40 km south of Munich, in Germany. Since its opening in 1987, data M SMS has always focused on developing software solutions for sheet metal forming. Their first product was a design software based on HP-UX ME10 and AutoCAD® that simplified the designing of tools for roll forming lines (COPRA® RF, Figure 1.1). Later, simulation solutions were developed using the finite element method (COPRA® FEA RF, Figure 1.2). The finite element analysis was developed using the software MSC Marc/Mentat, leading to the establishment of an OEM partnership between data M SMS and MSC [DATA M SMS 2012; FERREIRA 2016].

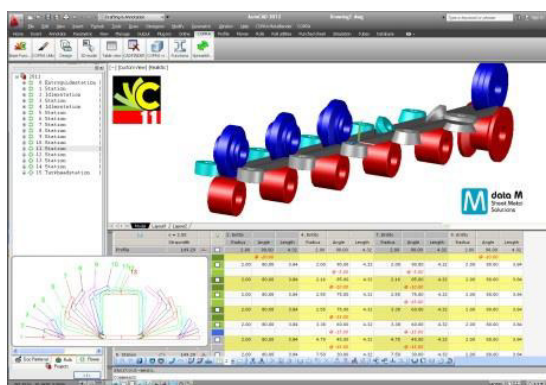


Figure 1.1 - Graphical interface in COPRA® RF.

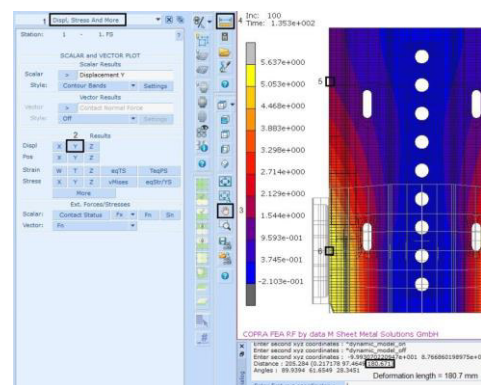


Figure 1.2 - Graphical interface in COPRA® FEA RF. Retrieved from [Lindgren 2015].

data M's mission is nowadays to develop knowledge in all areas of roll forming technology, from process design and development, the conception of roll forming lines, prototyping, to process control, defect analysis and troubleshooting. There is also a focus on user training and the development of new roll forming applications, such as flexible roll forming [ABEE 2010; FERREIRA 2016].

1.2 MOTIVATION AND PROJECT CONTEXT

The industry sector is responsible for 40 % of the total energy used globally and, within industry, manufacturing accounts for 98 % of the total direct carbon dioxide emissions. Worldwide, manufacturing is responsible for 35 % of the total used electricity and 20 % of carbon dioxide emissions [INGARAO 2017]. Furthermore, increasing energy demands, coupled with a restricted world supply, have resulted in rising energy prices. In fact, from 1993 to 2013, the energy prices in Germany increased by 100 % [APOSTOLOS 2013]. Thus, environmental awareness, simultaneously with high energy prices, are driving decision makers to put energy efficient productions at the top of their priorities. [SHROUF 2014].

Roll forming industry is not an exception and, nowadays, both energy consumption and waste are a major concern [LINDGREN 2007]. A roll forming operation consists of a long strip of metal sheet continuously bended by passing through a set of rolls mounted on consecutive stands. The incremental bending in each stand results from the contact between the set of rolls and the metal sheet [HALMOS 2006]. Thus, the energy required for the process, the rolls wear and possible manufacturing defects depend on the forces transmitted over the contact area and these forces need to be studied during the process design.

COPRA® FEA RF, developed by data M SMS, is a software used to simulate roll forming operations and assist the designer in the iterative process of improving the operation design. An optimisation of the contact representation in the roll forming simulations is essential to improve the torque and wear calculation in COPRA® FEA RF and, therefore, allow the designer to improve the energy distribution along the processing line, reduce the tool wear and better anticipate manufacturing defects during the designing phase. The development of a good simulation of the contact between rolls and sheet requires, firstly, an understanding of the contact modelling using the finite element method [SERVROLL 2017]. Given the complex sheet behaviour during a roll forming operation, a tribological experiment that represents the contact conditions in a generalised bending process was used to study the contact modelling.

1.3 OBJECTIVES

The primary objective of this dissertation was to develop a finite element model of a tribological experiment with an optimised contact representation. Given the contact inaccessibility for observation, one cannot be sure of the real contacting forces, however, when the same operation is simulated with different parameters and the calculated forces on each simulation converges to the same value, those parameters can be assumed to accurately represent the contact conditions. Thus, this dissertation aims to study the result's convergence with a set of parameters. The study focuses on the mesh discretisation, the contact search and the friction modelling. The influence of the mesh discretisation on the bending geometry and contact characterisation is investigated. Regarding the contact search, the study aims to investigate its influence on the contact detection, calculated forces and contact representation. Finally, the study of the friction modelling aims to analyse the friction influence on the bending representation and contact representation. Additionally, the influence of different numerical friction models is also investigated.

1.4 PROJECT METHODOLOGY

The first step of this study was the development of a finite element model of the physical tribological experiment. This model was then optimised by means of mesh discretisation, contact search and friction modelling. A possible contact zone was defined and different discretisations in the longitudinal and transverse direction were modelled. The longitudinal and transverse bending geometry, as well as the roll force and contact normal stress were studied in order to investigate the influence of this discretisation on the contact representation. An analysis of the results and its comparison with the computational time lead to an optimisation of the possible contact zone discretisation. A similar analysis was performed for different thickness discretisations and different locations of the element nodes with the roll axis. Having performed the optimisation of mesh discretisation, the contact search algorithm was investigated. Different models were created, each one with different values for the parameters included in the algorithm. The roll torque, roll force and the contact normal stress in each simulation were analysed. Finally, the friction models available in the finite element package were studied and the bending geometry, roll force and contact normal stress of each model were discussed.

1.5 DISSERTATION STRUCTURE

This dissertation consists of five main chapters: Chapter 1 is this introduction; Chapter 2, entitled Literature review, introduces the roll forming process and presents, as well, a review about contact mechanics and finite element contact analysis; Chapter 3, entitled Tribological test, explains the tribological experiment and outlines its finite element modelling; Chapter 4, entitled

Optimisation of the finite element model, presents the optimisation of the finite element model, considering the mesh descritisation, contact serach and friction modelling; finally, Chapter 6, entitled Conclusion and future work, presents the major findings of this work and sugested future developments.

2 LITERATURE REVIEW

In this chapter, a review of the literature is presented. Firstly, the roll forming process is introduced. It starts by an overview of the overall process, followed by a description of a sheet bending process, as well as a review of the sheet deformations during roll forming and roll forming computer simulations. Then, a review on contact mechanics is made considering the contact constraints, the constraints enforcement methods and the friction laws for metal forming. Finally, a review on FE contact analysis is made. Initially, a review on the time integration scheme is made, followed by a review on contact discretisation, contact search and, lastly, modelling issues.

2.1 ROLL FORMING

2.1.1 OVERVIEW

Roll forming is a highly productive process, forming up to $150 \text{ m} \cdot \text{min}^{-1}$, used in a wide range of industries, including the automotive and metallic construction industries. It is considered a complex sheet metal forming process and it is used to produce a broad range of profile cross-section [HALMOS 2006]. Even though roll forming is a common sheet metal forming process and used worldwide there are relatively few publications about the process. A reasonable explanation may be the complexity of the deformation behaviour in the process, despite its visual simplicity [LINDGREN 2007].

George T. Halmos [HALMOS 2006] defined the process as the forming of a “sheet metal strip along straight, longitudinal, parallel bend lines with multiple pairs of contoured rolls without changing the thickness of the material, at room temperature” [HALMOS 2006]. Figure 2.1 illustrates a roll forming process, in which the sheet passes through a defined number of stations leaving the manufacturing line with the desired U-profile.

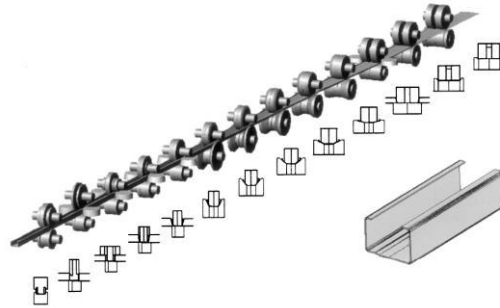


Figure 2.1 - Forming of the sheet from an undeformed strip to a finished profile. Retrieved from [HALMOS 2006].

During this sheet metal forming process, the consumed substance is a metal strip, which is progressively bent along the width direction by rollers in a forming line. Each set of rolls performs an incremental part of the forming process [BOMAN 2007]. In Figure 2.2 an example of a set of rolls is shown. A roll forming process can incorporate sweeping stations to produce curved profiles, punching or embossing stations and in-line welding for tube manufacturing. Thus, normally the profile comes out with the final desired shape [FERREIRA 2016; HALMOS 2006].

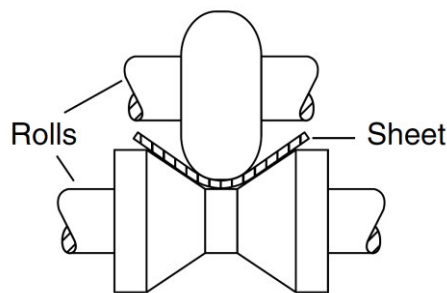


Figure 2.2 - Section of a set of rolls in a roll former. Retrieved from [MARCINIAK 2002].

The design of a roll forming process and the rolls for each station remains an experience-based art, rather than science. Even for a simple constant cross-section U-channel, the possible forming strategies are endless. As a matter of fact, nowadays different U-channel process designs are being commercially used [GÜLÇEKEN 2007]. The difficulty in developing consistent designing rules derives from the complex continuum bending process [FERREIRA 2016].

The number of rolls depends, usually, on the complexity of the profile geometry, planned to manufacture. Highly complex profiles require a larger number of rolls, usually associated with rotation axes in different planes [RODRIGUES 2010]. The overall production cost cannot be forgotten. When a large number of rolls are used in the forming line, the resultant applied bending is very gradual and unwanted deformations are reduced. However, due to economic constraints, the number of rolls must be minimised to reduce the overall cost. A compromise between tooling cost and section quality is the goal of the process design [BUI 2008].

The design of the process starts by defining the orientation of the part, followed by the definition of the number of passes needed to form each bend. This bending strategy is defined in a flower pattern (Figure 2.3). The flower pattern is defined in order to have a good forming path of the material [FERREIRA 2016; HALMOS 2006].

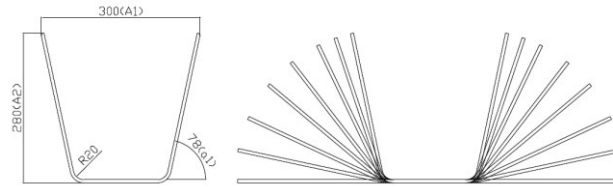


Figure 2.3 - Final profile and corresponding flower pattern. Retrieved from [ZENG 2009].

2.1.2 SHEET BENDING

In a roll forming process the profile is obtained by successive transverse bending. Thus, the fundamentals of bending along straight lines will be analysed. The case shown in Figure 2.4 will be considered, a unit width of a continuous sheet with a cylindrical bent region of radius of curvature ρ and bend angle θ . A moment per unit width M and a tension (force per unit width) T are applied. The tension is applied at the middle surface of the sheet [MARCINIAK 2002].

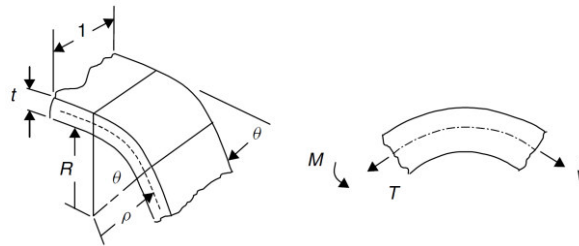


Figure 2.4 - Continuous strip bent along a line. Retrieved from [MARCINIAK 2002].

It is possible to assume that a normal plane section in the sheet will remain plane and normal, and converge on the centre of the curvature, as shown in Figure 2.5. This assumption is valid for a thin sheet with a bend radius approximately three or four times the sheet thickness [MARCINIAK 2002].

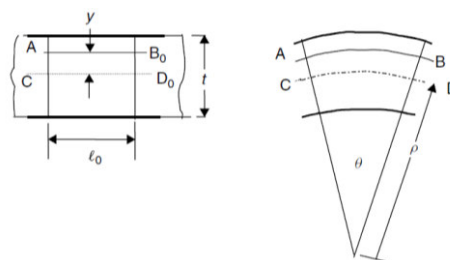


Figure 2.5 - Deformation of longitudinal fibres in bending and tension. Retrieved from [MARCINIAK 2002].

If, for example, the sheet is stretched during bending, the original line CD_0 may change its length to CD , becoming

$$l_s = \rho\theta \quad (2.1.1)$$

and the line AB_0 at a distance y from the middle surface will deform to a length given by equation [MARCINIAK 2002]

$$l = \theta(\rho + y) = \rho\theta \left(1 + \frac{y}{\rho}\right) = l_s \left(1 + \frac{y}{\rho}\right) \quad (2.1.2)$$

The axial strain of the fibre AB is given by

$$\varepsilon_1 = \ln \frac{l}{l_0} = \ln \frac{l_s}{l_0} + \ln \left(1 + \frac{y}{\rho} \right) = \varepsilon_a + \varepsilon_b \quad (2.1.3)$$

where

ε_a is the strain at the middle surface or the membrane strain

ε_b is the bending strain.

The bending strain can be approximated by equation (2.1.4) when the radius of curvature is large compared with the thickness of the sheet [MARCINIAK 2002].

$$\varepsilon_b = \ln \left(1 + \frac{y}{\rho} \right) \approx \frac{y}{\rho} \quad (2.1.4)$$

Therefore, the strain distribution is assumed to be approximately linear as represented in Figure 2.6.

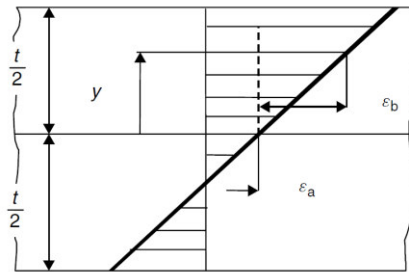


Figure 2.6 - Assumed strain distribution in sheet bending. Retrieved from [MARCINIAK 2002].

When the flat sheet, like the one of Figure 2.4, does not deform in either side of the bend, the material is constrained to deform in plane strain. In this case, the strain parallel to the bend line will be zero, and the deformation process in bending an isotropic sheet is given by equations (2.1.5-2.1.6) [MARCINIAK 2002].

$$\begin{aligned} \varepsilon_1 \\ \varepsilon_2 = 0 \end{aligned} \quad (2.1.5)$$

$$\varepsilon_3 = -\varepsilon_1$$

$$\begin{aligned} \sigma_1 \\ \sigma_2 = \frac{\sigma_1}{2} \end{aligned} \quad (2.1.6)$$

$$\sigma_3 = 0$$

In Figure 2.7 the stresses along the bend axis are represented. It is observed that the edge of the sheet curves as illustrated. This happens because, at the edge of the sheet, the stress along the bend axis is zero and plane strain does not exist. In the edges of the sheet, the stress state is approximately uniaxial. The minor strain will be negative near the outer surface and positive near the inner surface giving rise to the *anticlastic* curvature shown [MARCINIAK 2002].

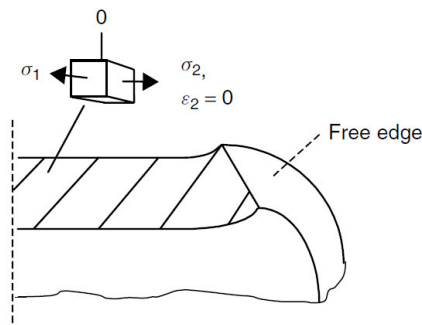


Figure 2.7 - Stress state on a section through the sheet in plane strain bending. Retrieved from [MARCINIAK 2002].

2.1.3 SHEET DEFORMATION DURING ROLL FORMING

During a roll forming process, the metal strip is subjected to a different type of deformations. The intended and most important deformation is the transversal bending deformation. This transverse bending is responsible for forming the metal strip into the product with the required cross-section [HALMOS 2006].

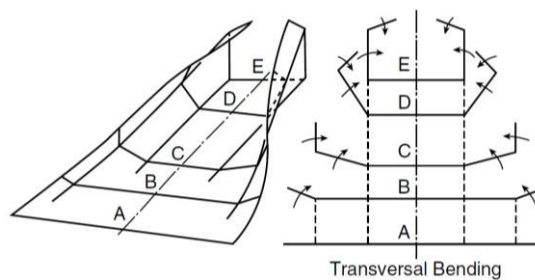


Figure 2.8 - Transversal (referred as transverse bending in the text) bending of metal strip during roll forming. Retrieved from [HALMOS 2006].

Other deformations are presented in the roll forming process. The metal strip is generally deformed into complicated 3D shapes by a series of contoured rolls, resulting in additive deformations introduced in the metal strip. These additive deformations are longitudinal bending and bending back, longitudinal elongation and/or shrinkage, transverse elongation and/or shrinkage, shear in the metal's plane, shear in the direction of the metal's thickness and various combinations of the previous (Figure 2.9) [HALMOS 2006].

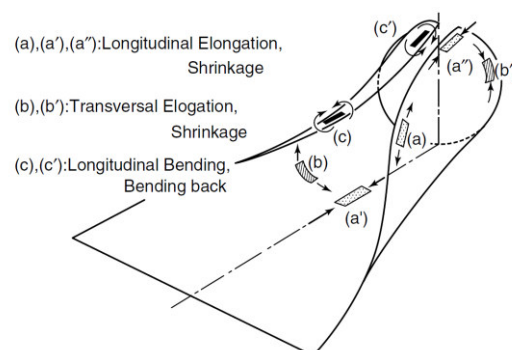


Figure 2.9 - Additive redundant deformations of the metal strip during roll forming. Retrieved from [HALMOS 2006].

Ideally, the strip should be subjected only to plane strain bending. However, as the sheet progressively deforms, it is formed a very complex 3D surface and the material is formed via different strain paths. Hence, the understanding of these strain paths would lead to better roll design and eliminate some of the common defects like edge wave, twist and longitudinal curvature [DUGGAL 1996]. These can be accomplished by an accurate computer simulation of the process.

2.1.4 ROLL FORMING COMPUTER SIMULATION

The use of finite element (FE) simulations to study the designing of the roll forming processes has been a crucial step in improving part quality and reducing manufacturing costs. Every designing decision can be checked and adjusted before taking place the manufacturing process. Nowadays finite element analysis (FEA) software allows the setup of a virtual roll forming line, where the iterative designing process can be carried out without the prohibitive retooling costs [ABEE 2010; FERREIRA 2016]. Figure 2.10 shows a schematic representation of a traditional designing process versus the one with virtual testing.

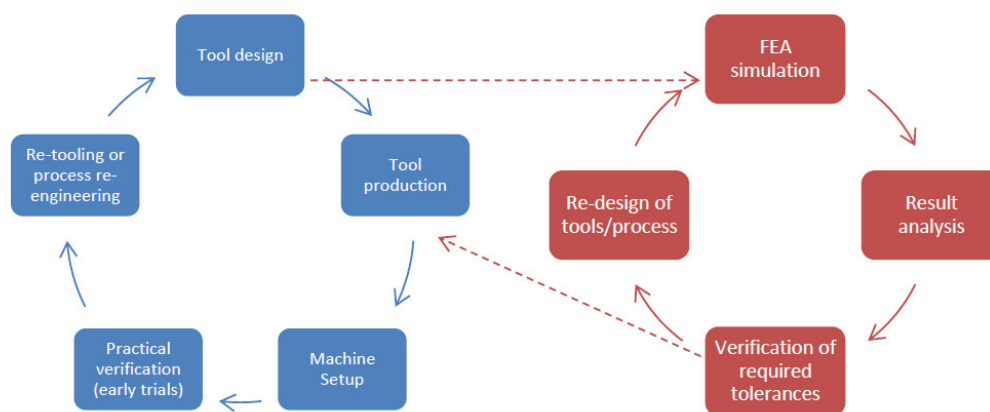


Figure 2.10 - Design process of a roll forming line; in blue is the traditional process of trial and error; in red, the upgraded process with virtual testing; dashed lines represent the connection between the cycles. Retrieved from [FERREIRA 2016].

The numerical simulation of a roll forming process involves macroscopic deformation of a deformable body – the metal strip -. Similarly to other plastic deformation processes, the continuum is modelled by a set of equations that define the relations between the variables involved in the body deformation. These equations are divided into i) the equilibrium equations and boundary conditions and ii) the constitutive material model. The first ensures the equilibrium of the continuum, compatible with the boundary conditions. The second establishes the relation between the stresses and strains, associated with the equilibrium conditions. The large deformations of the metal strip introduce a kinematic nonlinearity [OLIVEIRA 2005]. Besides that, the contact interaction between the rolls and the metal strip introduces a boundary nonlinearity [KIM 2015]. Consequently, the roll forming process is a highly nonlinear problem which is difficult to formulate.

2.2 CONTACT MECHANICS

In a standard nonlinear solid mechanics problem, both the displacements and the external forces prescribed in the body boundary are known *a priori*. The extension of this problem to a potential contact between multiple bodies requires an additional contact boundary. This contact boundary is unknown *a priori* and can change over time. Thus, the contact area, contact forces and motion of associated boundaries are a part of the solution [NETO 2014].

This section presents an introduction to contact mechanics and the continuum based formulation of frictional contact problems. This formulation involves the establishment of the contact constraints, a discussion of the different procedures that can be applied to incorporate the contact constraints into the variational principle and an overview of the friction laws appropriate for metal forming processes.

2.2.1 INTRODUCTION

When two bodies contact one another, stresses and deformations arise from the contact interaction. There are two types of contact: conforming and non-conforming contact. The contact is said conforming when the two surfaces of the body fit closely without deformation. On the other hand, when the bodies have different profiles, and at least one surface suffers deformation, the contact is classified as non-conforming. The contact area is usually small compared to the geometry of the bodies and the stresses are highly concentrated in the region close to the contact zone, not being influenced by the shape of the bodies at a distance from the contact zone [JOHNSON 1985].

When two non-conforming surfaces are brought into contact by a negligibly small force, the contact area is only one point [JOHNSON 1985]. This case is illustrated in Figure 2.11, where the lower body is denoted by the suffixes 1 and the upper body by 2, the Oz axis is chosen to coincide with the common normal with the two surfaces at O and the $x - y$ plane is the tangent plane of the two surfaces.

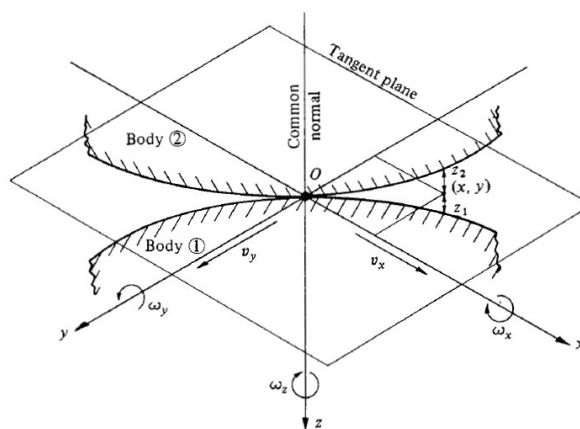


Figure 2.11 - Non-conforming surfaces in contact at O . Retrieved from [JOHNSON 1985].

At the point of contact, the absolute motion of body 1 is defined by the linear velocity V_1 and angular velocity Ω_1 , and body 2 is defined by the linear velocity V_2 and angular velocity Ω_2 . Considering that the contact point moves with the linear velocity V_O and rotates with angular velocity Ω_O , the relative motion of each body in the reference frame moving with the point O is defined by the equations [JOHNSON 1985]

$$v_1 = V_1 - V_O \quad (2.2.1)$$

$$v_2 = V_2 - V_O \quad (2.2.2)$$

$$\omega_1 = \Omega_1 - \Omega_O \quad (2.2.3)$$

$$\omega_2 = \Omega_2 - \Omega_O \quad (2.2.4)$$

where

- v_1 is the linear velocity of body 1 at the point of contact relative to the motion of point O ,
- v_2 is the linear velocity of body 2 at the point of contact relative to the motion of point O ,
- V_1 is the linear absolute velocity of body 1 at the point of contact ,
- V_2 is the linear absolute velocity of body 2 at the point of contact .

A continuous contact is defined as the contact of two surfaces neither separating or overlapping or, in another word, their velocity components along the common normal must be equal, stated as [JOHNSON 1985]

$$V_{z1} = V_{z2} = V_{zO} \quad (2.2.5)$$

where

- V_{z1} is the linear absolute velocity of body 1 at the point of contact in the z direction,
- V_{z2} is the linear absolute velocity of body 2 at the point of contact in the z direction,
- V_{zO} is the linear absolute velocity of the point of contact in the z direction.

Sliding is defined as the relative linear velocity between the two surfaces at point O and denote it by Δv , with components x and y , defined as [JOHNSON 1985]

$$\Delta v = v_1 - v_2 = V_1 - V_2 \quad (2.2.6)$$

where

- Δv is the linear sliding velocity between body 1 and 2,
- v_1 is the linear velocity of body 1 at the point of contact relative to the motion of point O ,
- v_2 is the linear velocity of body 2 at the point of contact relative to the motion of point O ,
- V_1 is the linear absolute velocity of body 1 at the point of contact ,
- V_2 is the linear absolute velocity of body 2 at the point of contact .

Rolling is defined as the relative angular velocities of the two bodies in an axis on the tangent plane, having x and y components, stated as [JOHNSON 1985]

$$\Delta\omega_x = \omega_{x1} - \omega_{x2} = \Omega_{x1} - \Omega_{x2} \quad (2.2.7)$$

$$\Delta\omega_y = \omega_{y1} - \omega_{y2} = \Omega_{y1} - \Omega_{y2} \quad (2.2.8)$$

where

$\Delta\omega_x$ is the rolling velocity between body 1 and 2 in the x direction,

ω_{x1} is the angular velocity of body 1 relative to the motion of point O in the x direction,

ω_{x2} is the angular velocity of body 2 relative to the motion of point O in the x direction,

Ω_{x1} is the absolute angular velocity of body 1 relative to the motion of point O in the x direction,

Ω_{x2} is the absolute angular velocity of body 2 relative to the motion of point O in the x direction.

Finally, the spin motion is defined as the relative angular velocity in the common normal axis, stated as [JOHNSON 1985]

$$\Delta\omega_z = \omega_{z1} - \omega_{z2} = \Omega_{z1} - \Omega_{z2} \quad (2.2.9)$$

where

$\Delta\omega_z$ is the rolling velocity between body 1 and 2 in the z direction,

ω_{z1} is the angular velocity of body 1 relative to the motion of point O in the z direction,

ω_{z2} is the angular velocity of body 2 relative to the motion of point O in the z direction,

Ω_{z1} is the absolute angular velocity of body 1 relative to the motion of point O in the z direction,

Ω_{z2} is the absolute angular velocity of body 2 relative to the motion of point O in the z direction.

Any contact interaction must satisfy the condition of continuous contact (2.2.5) and can be a combination of sliding rolling and spin [JOHNSON 1985].

The resultant force transmitted at a point of contact from one surface to another consists of a normal force \mathbf{P} and a tangential force \mathbf{Q} . The normal force acts along the common normal and, generally, is a compressive force, while the tangential force acts in the tangential plane with x and y components and is a result of the friction between the two surfaces, as it is represented in Figure 2.12 [JOHNSON 1985].

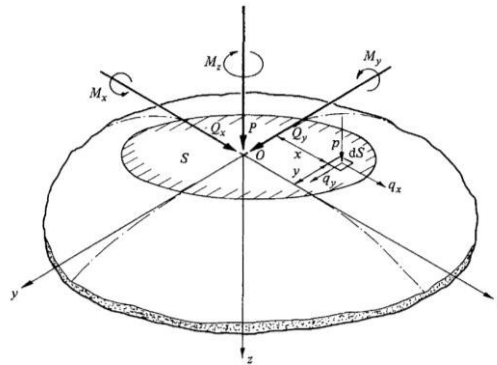


Figure 2.12 - Forces and moments acting on contact area S . Retrieved from [JOHNSON 1985].

The value of \mathbf{Q} must satisfy the condition [JOHNSON 1985]

$$Q \leq \mu P \quad (2.2.10)$$

where

Q is the tangential force,

μ is the coefficient of limiting friction,

P is the contact normal force.

The normal force transmitted in the contact has the effect of compress deformable solids creating a finite contact area and making possible to the contact to transmit also a moment. The components M_x and M_y are defined as rolling moments and are a resistance to the rolling motion,

as it is represented in Figure 2.12. Nevertheless, in most practical problems the rolling moments are small enough to be ignored [JOHNSON 1985].

The component of the moment along the common normal, M_z , is called the spin moment and, when it accompanies rolling, its energy dissipated together with the one dissipated by the rolling moments gives rise to the overall rolling resistance [JOHNSON 1985].

At this point, it is possible to define free rolling as the motion in which there is no spin, and the tangential force Q in the contact point is zero [JOHNSON 1985].

The forces \mathbf{P} and \mathbf{Q} and the moment \mathbf{M} depend on the normal traction p and tangential traction q . The distribution of p and q over the contact area S cannot be predicted at this stage, however a relation to determine \mathbf{P} and \mathbf{Q} [JOHNSON 1985] is given by the equilibrium equations stated as

$$P = \int_S p \, dS \quad (2.2.11)$$

$$Q_x = \int_S q_x \, dS \quad (2.2.12)$$

$$Q_y = \int_S q_y \, dS$$

where

P is the contact normal force,

S is the contact area,

p is the normal traction,

Q_x is the tangential force in the x direction,

q_x is the tangential traction in the x direction,

Q_y is the tangential force in the y direction,

q_y is the tangential traction in the y direction.

In non-conforming contact the contact area lies approximately in the $x - y$ plane, therefore the components of the moment \mathbf{M} can be calculated by equation [JOHNSON 1985]

$$M_x = \int_S py \, dS$$

$$M_y = - \int_S px \, dS \quad (2.2.13)$$

$$M_z = \int_S (q_y x - q_x y) \, dS$$

where

M_x is the moment along the x axis,

p is the normal traction,

M_y is the moment along the y axis,

M_z is the moment along the z axis.

2.2.2 CONTACT CONSTRAINTS

In the contact between a flexible body and a rigid surface, the flexible body is normally selected as the slave body and the rigid body as the master body. The contact constraints can be divided into normal impenetrability and tangential slip. The impenetrability conditions prevent the slave body from penetrating into the master body, whereas the tangential slip represents the friction behaviour on the contact surface [KIM 2015].

Figure 2.13 illustrates a general contact condition with a rigid surface in 2D. Contact boundary Γ_C denotes a part of the slave boundary and specified by the user. Although the actual contact region is a part of the solution, the boundary in which the contact can occur can be specified [KIM 2015].

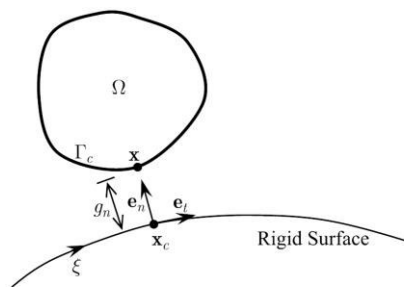


Figure 2.13 - Contact conditions in 2D. Retrieved from [KIM 2015].

A natural coordinate ξ (Figure 2.13) is used to represent the location of a point on the rigid surface – master surface – since its motion is prescribed during the analysis. Thus, the coordinates of the contact point \mathbf{x}_C on the master surface [KIM 2015] can also be represented as

$$\mathbf{x}_C = \mathbf{x}_C(\xi_C) \quad (2.2.14)$$

where

\mathbf{x}_C is the coordinate of the contact point on the master surface,

ξ_C is the natural coordinate of the contact point on the master surface.

In the 3D space, two natural coordinates are needed to describe the master surface [KIM 2015].

The contact analysis starts by searching for the contact point $\mathbf{x}_C(\xi_C)$ on the master surface corresponding to a slave point \mathbf{x} . Once identified, the two points on the master's surface are checked if they are in contact or not. Mathematically, this is called the orthogonal projection, or the closest point from the slave point \mathbf{x} (Figure 2.13) [KIM 2015]. For a general nonlinear curve, the following nonlinear equation [KIM 2015] is solved to find the contact point

$$\varphi(\xi_C) = (\mathbf{x} - \mathbf{x}_C(\xi_C))^T \mathbf{e}_t(\xi_C) = 0 \quad (2.2.15)$$

and

$$\mathbf{e}_t = \frac{\mathbf{t}}{\|\mathbf{t}\|} \quad (2.2.16)$$

$$\mathbf{t} = \frac{\partial \mathbf{x}_C}{\partial \xi} \tag{2.2.17}$$

where

- \mathbf{x} is a point on the slave surface,
- \mathbf{x}_C is the coordinate of the contact point in the master surface,
- ξ_C is the natural coordinate of the contact point on the master surface,
- \mathbf{e}_t is the unit tangential vector,
- \mathbf{t} is the tangential vector at the contact point,
- ξ is the location of a point on the master surface.

Equation (2.2.15) is called the contact consistency condition and $\mathbf{x}_C(\xi_C)$ is the closest projection point of $\mathbf{x} \in \Gamma_C$ onto the rigid surface that satisfies equation (2.2.15) [KIM 2015].

The contact can be checked measuring the distance between the two contact points. Moreover, the impenetrability condition can be imposed by using the same distance (Figure 2.13) [KIM 2015]. The normal gap function g_n [KIM 2015], which measures the normal distance, defines the impenetrability condition as

$$g_n \equiv (\mathbf{x} - \mathbf{x}_C(\xi_C))^T \mathbf{e}_n(\xi_C) \geq 0, \mathbf{x} \in \Gamma_C \tag{2.2.18}$$

where

- g_n is the gap function,
- \mathbf{x} is a point on the slave surface,
- \mathbf{x}_C is the coordinate of the contact point in the master surface,
- ξ_C is the natural coordinate of the contact point on the master surface,
- \mathbf{e}_n is the unit outward normal vector of the master surface at the contact point,
- Γ_C is the contact boundary.

A gap function greater than zero means that the points are separated, equal to zero means that the points are in contact and less than zero means that the slave point has penetrated the master body (FIGURE 2.14) [YASTREBOV 2013].

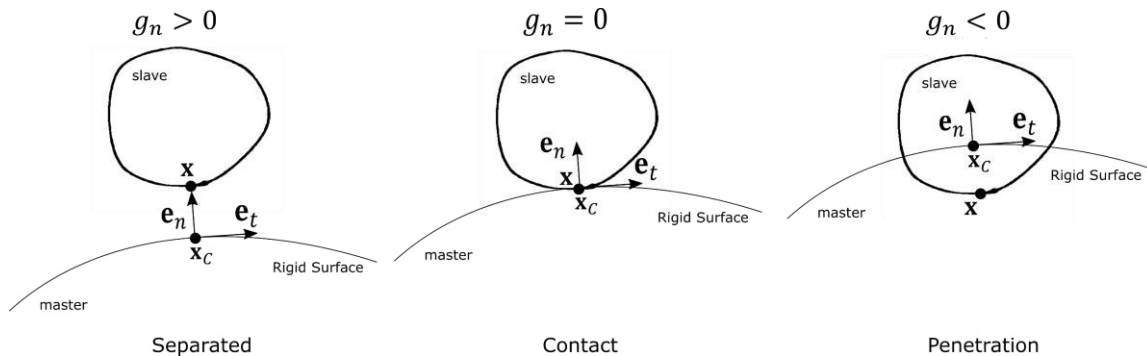


FIGURE 2.14 - Three different geometrical conditions of the slave point with respect to the master body.

As the contact point moves along the master boundary, a frictional force in a tangential direction to the master boundary resists the tangential relative movement [KIM 2015]. The tangential slip function g_t [KIM 2015] is the measure of the relative movement of the contact point along the rigid surface and is defined as

$$g_t \equiv \|\mathbf{t}^0\|(\xi_C - \xi_C^0) \quad (2.2.19)$$

where

g_t is the tangential slip function,

\mathbf{t}^0 is the tangential vector at the previously converged time increment,

ξ_C is the natural coordinate of the contact point on the master surface,

ξ_C^0 is the natural coordinate at the previously converged time increment.

2.2.3 CONSTRAINT ENFORCEMENT METHODS

This section contains a description of the different procedures that can be used to incorporate the contact constraints into the variational principle of the contact problem. The variational principle for contact problems can result in a variational inequality subjected to geometrical constraints. This formulation results in a nonlinear optimisation problem under inequality constraints [NETO 2014]. Nevertheless, the variational inequalities can be replaced by variational equality if the active contact area is known. Thus, the assumption of a known active contact area leads us to an unconstrained or partly unconstrained problem [WRIGGERS 2006]. This assumption makes possible to apply the regular methods from optimisation theory.

Some of the most popular and widely used resolution methods in contact mechanics are [NETO 2014]:

- The penalty method;
- The barrier method;
- The Lagrange multiplier method;
- The perturbed Lagrangian method;
- The augmented Lagrangian method;
- The Nitsche method.

In this section, the attention is focused on the ones most found in applications to sheet metal forming processes.

PENALTY METHOD

The penalty method is one of the most extensively used methods for treating contact problems in commercial and scientific FE codes [YASTREBOV 2013]. The contact constraints are removed explicitly from the variational formulation introducing a penalisation of the constraint violation. The constraint penalization magnitude is proportional to the extent of the constraint violation. Hence, it can be physically interpreted as a series of springs in the contact area with zero initial length, as represented in Figure 2.15 [NETO 2014].

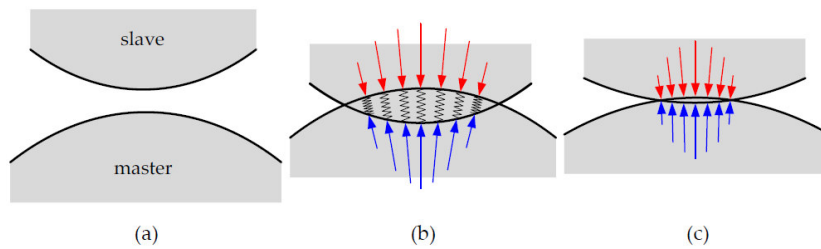


Figure 2.15 - Physical interpretation of the penalty method: (a) initial configuration; (b) configuration after penetration; (c) equilibrium state. Retrieved from [NETO 2014].

Once the contact constraints are explicitly removed from the variational formulation, the contact problem is formulated as a regular unconstrained optimisation problem. This optimisation is a minimization problem where the unknown variables are the displacements [NETO 2014].

The penalty regularisation dictates that the impenetrability condition (2.2.18) is only approximately fulfilled and the contact pressure is assumed to be a continuous function dependent on the penetration. Figure 2.16 illustrates the regularisation of the non-penetration constraint and the Coulomb's friction law. The parameters ε_n and ε_t denote the penalty parameter for normal and tangential contact, respectively [NETO 2014].

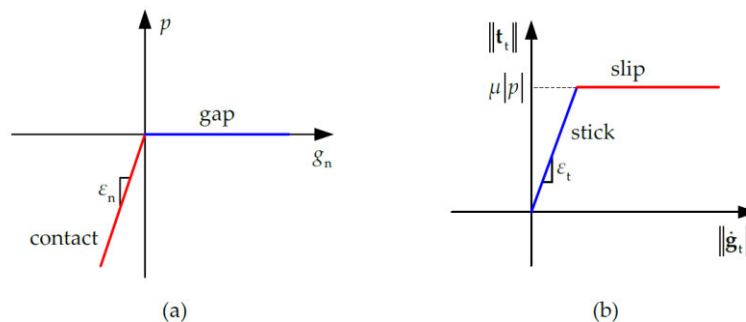


Figure 2.16 - Application of the penalty method to the frictional contact problem: (a) regularised unilateral contact law; (b) regularised Coulomb's friction law. Adapted from [NETO 2014]

The non-penetration contact condition is strictly fulfilled for non-negative gaps (Figure 2.16). On the contrary, the linear relation between contact pressure and the gap function dictates that the contact arises only for negative gap values, allowing penetration of the bodies. Therefore, the impenetrability condition (2.2.18) is only precisely represented if an infinite penalty method is used, resulting in an approximately straight line $g_n = 0$. This implementation is practically impossible in real calculations [NETO 2014].

Some tangential movement is allowed in a stick condition when using the penalty method (Figure 2.16). Consequently, a very low penalty value can result in an incorrect representation of the physical behaviour of the interface [NETO 2014]. However, significant experimental evidence shows that the stick to slip transition is not abrupt, and the penalty regularisation can be used to better model the frictional behaviour [LAURSEN 2002].

LAGRANGE MULTIPLIER METHOD

The Lagrange multiplier method is commonly used in optimisation problems to find the maximum/minimum of a function subjected to equality constraints. In the Lagrange multiplier method, a vector of additional unknowns λ , called Lagrange multipliers, is introduced. The Lagrange multiplier replaces the original constrained optimization problem by a saddle point of the function, called Lagrangian $\mathcal{L}(\mathbf{u}, \lambda)$. This method allows an exact fulfilment of the contact constraints (2.2.18) and (2.2.19) by introducing additional degrees of freedom (Lagrange multipliers). This practice increases the computational effort in comparison with the penalty method [NETO 2014].

In the case of the Lagrange multiplier method, the minimization problem with inequality constraints is not entirely unconstrained. The constraint $\lambda_n \leq 0$ has still to be satisfied. The parameter λ_n represents a continuous set of values (Lagrange multipliers) on the active contact zone. This parameter is interpreted as the contact pressure necessary to prevent interpenetration of the bodies. Due to this inequality constraint in the Lagrange multiplier method, the method need to be coupled with an active set strategy. In fact, the variational equality is only integrated in the points where the contact constraint is active. Generally, these points are unknown *a priori*. Therefore, the solution of the variational equality involves an iterative procedure to determine the active contact zone [NETO 2014].

AUGMENTED LAGRANGIAN METHOD

The Augmented Lagrangian method combines the advantages of both the penalty and the Lagrange multiplier methods and avoids their drawbacks. Thus, an exact enforcement of the contact constraints for a finite value of the penalty parameter is accomplished. It can be expressed as a Lagrange multiplier formulation regularised by penalty functions. In the case of an exact satisfaction of the contact constraints, the penalty term disappears, leading to the same solution as the Lagrange multiplier method. On the other hand, when λ is set to zero, the penalty functional is recovered. The main advantage of this combination is the achievement of a fully unconstrained problem, which makes it better than the Lagrange multiplier method for practical applications [NETO 2014].

2.2.4 FRICTION LAWS FOR METAL FORMING

Friction conditions are a major factor in the quality of sheet metal formed parts [HOL 2016]. In metal forming simulations, friction has been assumed to follow the Coulomb friction law or the constant shear friction law. For the Coulomb friction law, the frictional stress is proportional to the normal stress or force. On the other hand, the constant shear friction law states that the frictional stress is a certain fraction of the shear yield stress of the material. On the contact shear friction law, the effects of the normal stress on the frictional stress are not considered. It is

clear that frictional stress is related to the normal stress, and that the Coulomb friction law or its variants can describe the real behaviour of friction better than the constant shear friction law [JOUN 2009].

The limitation of Coulomb's law is related to the fact that the frictional stress predicted can reach very high values. Thus, in most practical applications, a threshold value (k) is introduced to limit the friction stress, as represented in Figure 2.17 [WRIGGERS 2006].

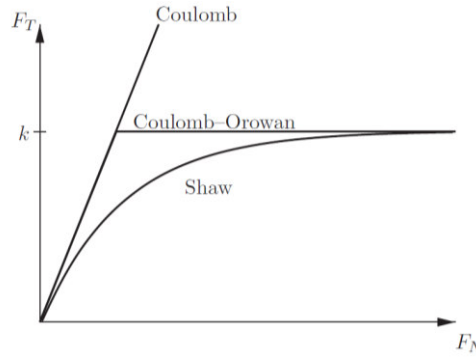


Figure 2.17 - Different possibilities to limit the frictional stress; F_N denotes the contact normal force and F_T denotes the contact tangential force. Retrieved from [WRIGGERS 2006].

The simplest approach to account for a limit stress is to write the slip function [WRIGGERS 2006] as

$$f_s(\boldsymbol{\sigma}_t) = \|\boldsymbol{\sigma}_t\| - h < 0 \quad (2.2.20)$$

where

- f_s is the slip function,
- $\boldsymbol{\sigma}_t$ is the contact tangential stress,
- h is a limiting function.

Two possible choices for the function h are available: the Coulomb-Orowan law and the Shaw law (Figure 2.17) [WRIGGERS 2006].

The Coulomb-Orowan law [WRIGGERS 2006] is formulated as

$$h = \min(\mu|p_n|, Y_0) \quad (2.2.21)$$

where

- h is a limiting function,
- μ is the friction coefficient,
- p_n is the contact normal stress,
- Y_0 is the elastic limit.

The Shaw law [WRIGGERS 2006] is formulated as

$$h = \beta Y_0 \quad (2.2.22)$$

with

$$\beta = \frac{A_r}{A_a} \quad (2.2.22)$$

where

- h is a limiting function,
- A_r is the real contact area,
- A_a is the nominal contact area.

The Shaw law, compared to the Coulomb–Orowan law, leads to a smooth function between the normal pressure and the tangential stress. Thus, the Shaw law is more adequate for numerical purposes [WRIGGERS 2006].

More recently, researchers have demonstrated that, typically in sheet metal forming, the friction coefficient strongly depends on the contact normal stress, the slip-rate between the interacting partners and on the contact temperature [KLOCKE 2015]. Filzek and Ludwig [FILZEK 2013] proposed a friction model considering these variables in the friction coefficient determination. The friction coefficient is determined from experimental data by the relation

$$\mu = \mu_0 \cdot \left(\frac{p}{p_0}\right)^{l-1} \cdot \left(\frac{v}{v_0}\right)^{m-1} \cdot \left(\frac{T}{T_0}\right)^{n-1} \quad (2.2.23)$$

where

- μ is the friction coefficient,
- μ_0 is a reference friction value determined using a defined contact pressure p_0 and a slip-rate v_0 at the reference temperature T_0
- v is the slip-rate
- T is the temperature
- l , m and n are scalar coefficients determined using a regression analysis to fit the presented friction model to experimental data.

An adaptation of Fielzek’s law has already been successfully implemented by Klocke et al. [KLOCKE 2015] in the FEA software ABAQUS using a user subroutine.

2.3 FE CONTACT ANALYSIS

In general, contact analysis is used to find the contact point and the contact force at the contact point, including contact pressure and frictional force. In finite element analysis, either displacement or force is known at the boundary and the other unknown variable is solved through the equilibrium requirements. In contact analysis, however, both the contact point x_c and the contact force at that point are unknown, which makes the contact problem challenging. Usually, a trial-and-error approach is taken in which the contact point is found from the current geometry, and the contact constraint is imposed once the point is in contact.

Contact analysis aims to answer the following questions: where is the location of the contact, how much contact force occurs at the contact area and is there a relative motion after contact in the interface. Given the inaccessibility of the contact for observation, a numerical model is one of the few options available to study in detail these contact conditions.

2.3.1 TIME INTEGRATION SCHEMES

A material having a mechanical behaviour dependent on the deformation history is called path-dependent. The metal strip of a roll forming operation is also path-dependent due to its plastic behaviour at large strains. Moreover, the contact conditions dictate a continuous change of the contact areas during the time interval of interest, imposing different boundary conditions at each instant. When the friction phenomena are taken into account, the solution becomes path-dependent due to the dissipative effect of the friction process. Therefore, a temporal discretisation is necessary to capture all these time dependent effects [NETO 2014].

Iterations are used to calculate the solution through a sequence of steps from the starting state to the final converged state. The numerical solutions schemes available can be divided into explicit and implicit. An explicit solution is applied when a direct computation of the dependent variables can be made regarding known quantities. An implicit solution is applied when coupled sets of equations define the dependent variables, and either a matrix or iterative technique is needed to obtain the solution. [FLOW SCIENCE 2017].

The choice of a time integration algorithm is an important criterion to ensure efficiency and robustness of numerical simulations. Implicit algorithms require iterative solutions for each time increment (time step), contrarily to explicit ones. However, for stability reasons, explicit methods use smaller time steps than implicit ones. Explicit methods, avoiding iterations and convergence problems, are therefore generally used for highly nonlinear problems with many degrees of freedom. On the other hand, for slower dynamics problems with fewer nonlinearities, implicit algorithms allow working with larger time step size, resulting in more numerical stability and accuracy. However, a real sheet metal forming process, such as roll forming, has time intervals governed by high nonlinear dynamics and others governed by slower nonlinear dynamics [NOELS 2004]. A time integration scheme that combines both explicit and implicit algorithms are believed to increase computability and efficiency and have already been proposed by [NOELS 2004] and [OLIVER 2008].

2.3.2 CONTACT DISCRETISATION

Although tool and metal sheet are usually discretised using mesh (with element and nodes) it should be mentioned that other strategies can be used. As an example Santos et al. [SANTOS 1995] presented studies using different forms of 3-D complex shape descriptions of tool geometries in finite-element analysis and corresponding consistent contact strategies. Such strategies included tool descriptions defined by parametric surfaces (NURBs), mesh description and the point data description. In the current work, the tools were discretised using a mesh description.

The spatial discretisation of the contacting bodies using a finite element mesh gives rise to differences between the continuous ($\partial\Omega$) and the discretised boundary geometry ($\partial\Omega^h$), as represented in Figure 3.2 [NETO 2014].

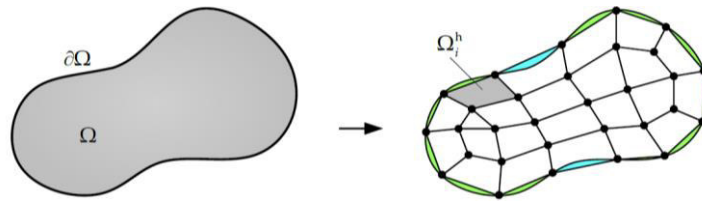


Figure 2.18 - Continuous body and its discretised representation using a finite element mesh composed by finite elements and nodes. Retrieved from [NETO 2014].

Indeed, the surface of the finite element mesh only approximates the real surface of the body. The finite element mesh surface boundary is defined by the reunion of each finite element surface boundary [NETO 2014] as

$$\partial\Omega \approx \partial\Omega^h = \bigcup_{i=1}^N \partial\Omega_i^h \quad (2.2.23)$$

where

$\partial\Omega$ is the continuous surface of the body,

$\partial\Omega^h$ is the discretised surface of the body.

Due to inaccurate contact surface description some mathematical and numerical difficulties can arise in the contact treatment [NETO 2014].

The contact discretisation establishes the contact elements structure that transfers the forces involved in the contact interaction [YASTREBOV 2013]. Contact elements can be geometrically interpreted as the connection between separated surfaces, sharing components (nodes or segments) from both surfaces. Normally, the discretization of the contact area is classified into three main types (Figure 2.19): (i) Node-to-Node (NTN); (ii) Node-to-Segment (NTS) and (iii) Segment-to-Segment (STS) [NETO 2014]

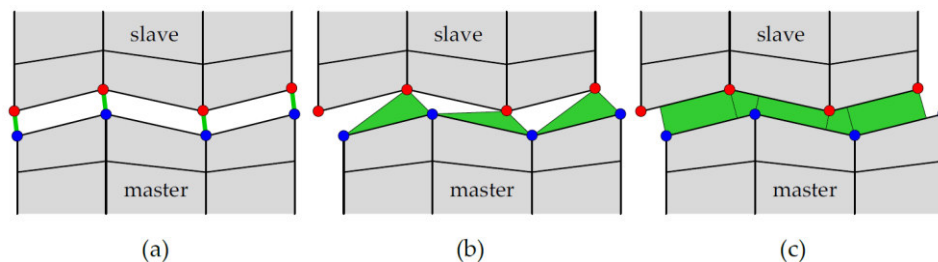


Figure 2.19 - Schematic illustration of different types of contact discretization: (a) Node-to-Node; (b) Node-to-Segment; (c) Segment-to-Segment. Retrieved from [NETO 2014].

The NTN discretisation technic is the simplest one and incorporates the contact constraints directly on the nodal pairs. However, this contact discretisation can only be applied to small deformation problems and does not allow for finite sliding. Besides, drawbacks on mesh generation are associated to NTN discretisation technics due to the requirement of conforming meshes along the contacting surface. In another word, each node of one contacting surface needs to have a single corresponding node on the opposite surface. On the other hand, due to the imposed conforming contact area, the NTN discretization passes the contact patch test proposed

by Taylor and Papadopoulos [TAYLOR 1991] - uniform pressure transferred correctly through the contact area.

The NTS discretisation technic is more adequate for large deformation and large sliding problems [WRIGGERS 1990]. This contact discretisation can be applied in non-conforming meshes (nodes at the contact area located at different positions). This situation can happen when the meshes are generated independently in each body or when sliding occurs in the contact area. The contact pairs are composed of a node of the slave surface and a corresponding segment of the master surface (Figure 2.19) [NETO 2014].

The STS contact discretisation technic has recently been successfully coupled with the mortar method. The mortar method was originally developed in the context of domain decomposition techniques for non-conforming meshes. Although the mortar-based STS discretisation is more robust and accurate than the standard NTS, its implementation is a great challenge. In fact, for the general three-dimensional case, the mortar interface coupling and numerical integration for arbitrary surface meshes is a complex task due to the surface segmentation [NETO 2014].

2.3.3 CONTACT SEARCH

After creating the contact elements, the solution procedure continues with the contact search. This solution step aims to determine the contacting pairs on the discretized surfaces. The easiest way of performing a contact search is for the user to specify the master element with which the slave node will contact. This is only possible when deformation is small and no relative motion exists in the contact area (NTN discretisation). However, this approach works for an insufficient number of cases and the contact surface must be simple enough so that the user knows the exact contact region in advance [HONG 2001].

Normally, the user does not know what contact pairs are actually in contact. Instead, the user specifies all possible candidates. During the contact analysis, the program searches for all contact pairs and determines those pairs that are actually in contact. The pair is in contact if the impenetrability condition is violated. Since contact pairs include all possible pairs, the number of pairs is considerably large. The program will perform this search for each iteration. Consequently, it is important to have an efficient search for contact pairs [KIM 2015].

To reduce the computational cost of the contact searching process and, thus, optimise the contact analysis, some commercial programs usually introduce a contact tolerance. This contact tolerance is defined as the minimum distance to search for contact. Its default value is 1 % of the contact element length. If two contact surfaces are inside the distance tolerance, they are considered to be in contact and the contacting force is then calculated. Figure 2.20 illustrates the contact searching process when a distance tolerance is defined. The contact tolerance is defined in two values: d_1 for separation and d_2 for penetration.

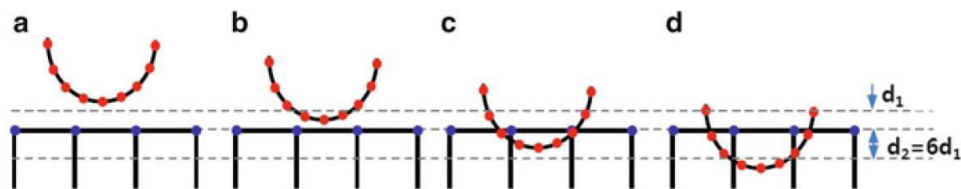


Figure 2.20 - Contact tolerance and detecting contact. Retrieved from [KIM 2015].

In cases (b) and (c), the initial separation or penetration is within the tolerance, so the contact pair is established. Then, a contact force is calculated, and a convergence analysis is performed. In cases (a) and (d), the initial separation or penetration is larger than the contact tolerance. Thus, contact is not detected [KIM 2015].

An appropriate load increment is crucial to ensure that the body does not cross the distance tolerance and penetrates the body without being in contact (Figure 2.21). If the load increment is too large, then the contact search algorithm fails to detect contact because the movement is larger than the contact tolerance (as in Figure 2.21c). In the case (b), the contact surface is within the contact tolerance. Even if for a significant penetration, the contact pair will be generated, and the impenetrability condition will be satisfied through bisecting the load increment [KIM 2015].

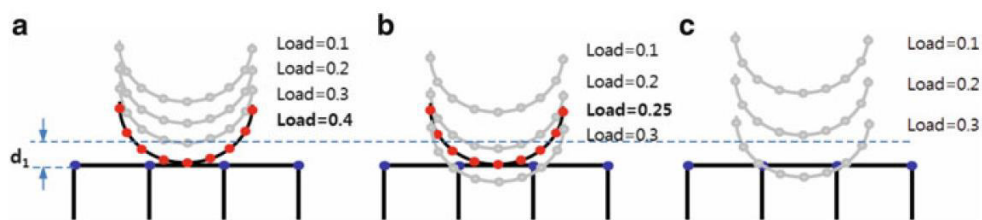


Figure 2.21 - The effect of load increment in contact detection. Retrieved from [KIM 2015].

2.3.4 MODELLING ISSUES

DEFINITION OF SLAVE AND MASTER

When two bodies are in contact, the slave-master concept distinguishes the two. One body is the slave body, and the other is the master. The contact condition is imposed on the slave body, ensuring that it does not penetrate the master body. Hypothetically, the master body can penetrate the slave body. This is physically impossible, but numerically possible since only the slave body is checked. Figure 2.22 illustrates a comparison of the two alternative definitions of slave and master body for a contact between a curved and a flat surface. When a curved boundary with a fine mesh is selected as the master and a flat boundary with a coarse mesh as the slave (Figure 2.22a), a significant amount of penetration is visible without a slave node penetrating the master body. Switching the slave-master definition, this situation is prevented (Figure 2.22b). Thus, to minimise numerical errors, a flat and stiff body should be selected as the master and a concave and soft body as the slave. Ideally, the master should also have the coarse mesh, and the

slave should have the finer mesh. In the case of flexible–rigid body contact, the rigid body is selected as a master body and the flexible one as a slave body [KIM 2015].

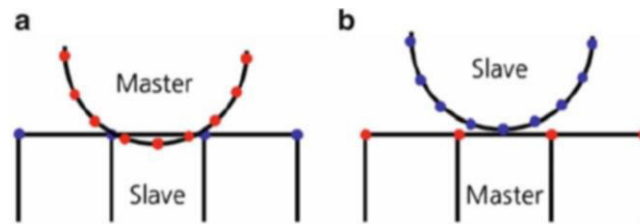


Figure 2.22 - Definition of slave and master. Retrieved from [KIM 2015].

DEFORMABLE CONTACT VS. DEFORMABLE-RIGID CONTACT

All bodies are deformable from a mechanical point of view, so it would be natural to model everything as a deformable body. However, since modelling is an abstraction of physical phenomena, it is possible to consider a body as a rigid body, which, sometimes, brings numerical advantages [KIM 2015].

A deformable-deformable contact is typically applied when two bodies have a similar stiffness, and both can deform, as, for example, a metal-metal contact. However, when stiffness is significantly different, the deformation of the stiff body can be neglected in comparison with the soft body. The choice of adopting a deformable-rigid contact can also be related to the system's physical behaviour [KIM 2015].

When two bodies have a large difference in stiffness, the stiffness matrix becomes ill-conditioned, and the matrix equation loses many significant digits. Thus, it becomes difficult to perform an accurate calculation. Also, the numerical implementation of deformable–rigid body contact formulation is much easier than multi-body contact formulation. Thus, a deformable-rigid contact has numerical advantages over a deformable-deformable contact [KIM 2015].

SENSITIVITY OF MESH DISCRETISATION

At the continuum level, it is assumed that the contact boundary varies smoothly. However, in the numerical model, the contact boundary is approximated by piecewise continuous curves or straight lines and only C^0 continuity is ensured across the element boundary. Thus, the contact boundary slope is not continuous. Furthermore, the contact force is very sensitive to the boundary discretisation and strongly depends on this slope, since it acts in the normal direction of the contact boundary. Therefore, if the actual contact point is near the boundary of two elements with a large slope change, it is possible that the Newton–Raphson iteration may have difficulty to converge [KIM 2015].

The contact normal stress distribution depends strongly on the mesh discretisation. If a uniform pressure is applied on top of a slave body, it would be expected that a uniform contact normal stress acts on the bottom surface. However, because of a large master surface at the

bottom, the contact normal stress is, actually, non-uniform and has its maxima on the edge of the contacting region (Figure 2.23). Theoretically, the contact stress on the edge can be twice the inside contact stress [KIM 2015].

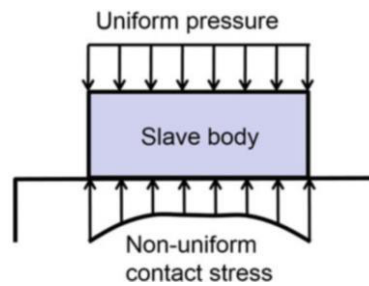


Figure 2.23 - Contact stress distribution under uniform pressure load. Retrieved from [KIM 2015].

The contact normal stress distribution is also influenced by the location of the nodes in relation to the slave body and the applied external loads. Figure 2.24 illustrates contact normal stress distributions for different locations of the block. This mesh sensitivity, suggests that a mesh discretisation study needs be performed [KIM 2015].

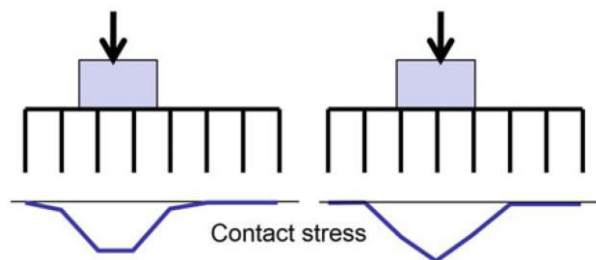


Figure 2.24 - Variation of contact stress distribution as a function of block location. Retrieved from [KIM 2015].

3 MODELLING OF THE TRIBOLOGICAL EXPERIMENT

In this chapter, the modelling of the tribological experiment is outlined. Firstly, section 3.1 explains the physical experiment, which consists of a servo controlled roll that is pressed against a metal sheet. The finite element (FE) model of this experiment is presented in section 3.2.

3.1 PHYSICAL EXPERIMENT

This experiment was developed by Galdos et al. [GALDOS 2017] from University of Mondragon, a data M SMS partner in several projects. The experiment aims to study the contact conditions in a generalised bending process. As seen in Figure 3.1, by pressing the roll against the metal sheet, the sheet is forced to bend and a longitudinal stress is induced [GALDOS 2017].

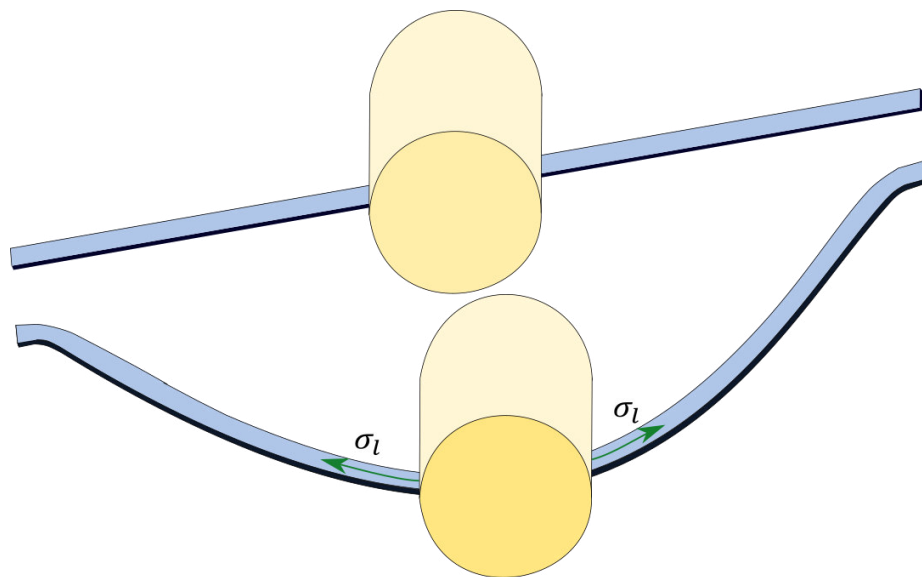


Figure 3.1 - Longitudinal stress (σ_l) created in the sheet by the roll penetration.

This tribological experiment is divided into three phases: roll penetration, application of an increasing torque and rotation with a constant angular velocity.

PENETRATION PHASE: an increasing force is applied to the roll (F_{roll}), forcing it to move against the sheet (Figure 3.2). This movement creates a longitudinal stress (σ_l) and the contact between the bodies generates a contact normal stress (σ_n) over the contact area.

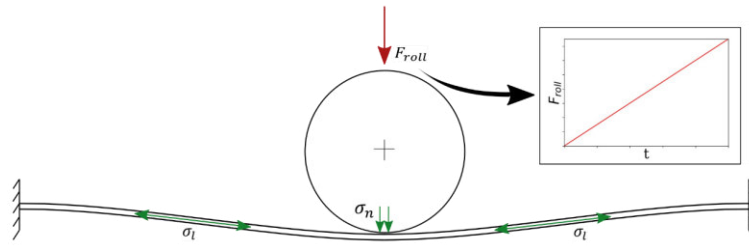


Figure 3.2 - An increasing roll force (F_{roll}) applied to the roll creates a longitudinal stress (σ_l) in the sheet; as a result of the contact, a compressive contact normal stress (σ_n) is applied to the sheet.

The penetration phase stops when a certain roll force is reached. This roll force is calculated in order to ensure a certain longitudinal strain level.

Table 3.1 summarises the roll forces, for the different longitudinal stresses tested, at which the penetration phase is stopped.

Table 3.1 - Termination roll force (F_{roll}) for the different roll penetrations.

Test	F_{roll} [N]
low	1103
mid	2567
high	3289

TORQUE PHASE: an increasing torque is applied to the roll (T_{roll}) (Figure 3.3). When the torque reaches a certain value, which is called the static torque, the roll starts rotating. At this point the torque is measured to be used to determine the static friction coefficient. The roll rotation marks the end of torque phase.

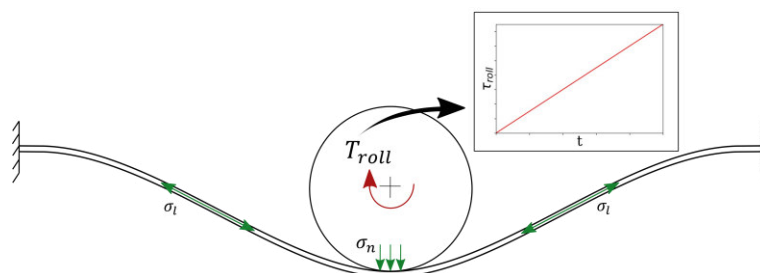


Figure 3.3 - An increasing torque (T_{roll}) is applied to the roll; as a result of the contact, a compressive contact normal stress (σ_n).

ROTATION PHASE: the roll rotates with a constant angular velocity (ω) (Figure 3.4).

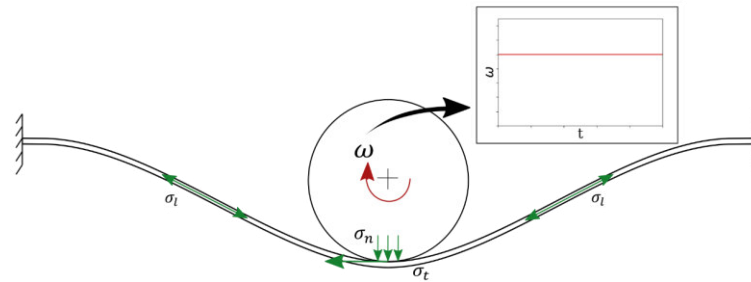


Figure 3.4 - A constant angular velocity (ω) is applied to the roll; as a result of the contact, a compressive contact normal stress (σ_n) and a contact friction stress (σ_t) is applied to the sheet.

The sheet is positioned in the tribotester with its extremities fixed, while the roll is tangent to the sheet and aligned with the sheet centre (Figure 3.5).

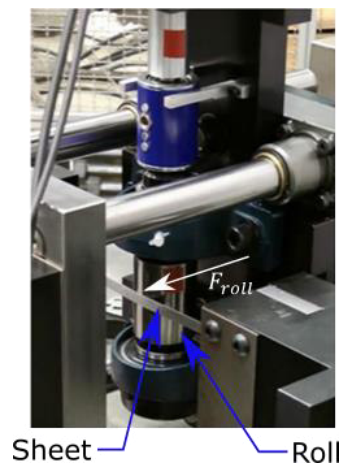


Figure 3.5 - Sheet and roll position in the tribotester with the roll force direction marked. Adapted from [GALDOS 2017].

Figure 3.6 shows the assembly of the tribotester components. The roll is positioned in the table with two bearings. It is connected to a torque sensor, being controlled by an electric servo motor coupled with a reducer. The bearings ensured that the roll can only rotate along its axial axis. The displacements of the roll are prevented in all directions. The penetration is obtained making the table move in the direction of the roll force represented in Figure 3.5 [GALDOS 2017].

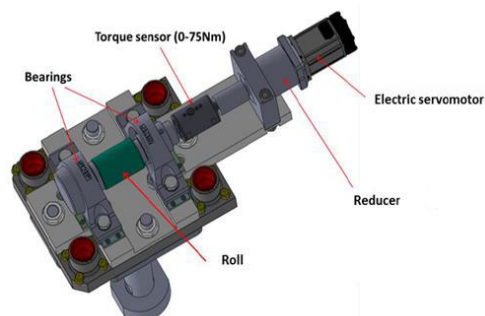


Figure 3.6 - Tribotester components. Retrieved from [GALDOS 2017].

The sheet material used in the experiment was DP1000 steel, which is being increasingly used in the automotive industry [GALDOS 2017]. The Young's modulus (E), yield strength ($R_{p\ 0.2}$), tensile strength (R_m) and the percentage of elongation after fracture (A_{80}), as well as the static (μ_s) and dynamic (μ_d) friction coefficient for this contact conditions are shown in Table 3.2.

Table 3.2 - Mechanical properties of DP1000 and friction coefficients [Galdos 2017].

E [GPa]	$R_{p\ 0.2}$ [MPa]	R_m [MPa]	A_{80} [%]	μ_s [-]	μ_d [-]
202	928	1060	8	0.1475	0.1325

3.2 FE NUMERICAL MODEL

In the physical experiment, the contact area is inaccessible for observation and the acting forces over that contact area are difficult to be measured over time. A FEM simulation of the physical experiment overcomes this barrier and allows to access that contact area and calculate the acting forces at any instant. The FE model presented in this section aims to study the contact conditions in the tribological experiment and was modelled considering that purpose.

This section outlines the FE modelling of the tribological experiment using the FEA software COPRA® FEA RF, developed by data M SMS. First, the model geometry is presented, followed by the element type used, the discretisation of the metal sheet, the material modelling, the load cases simulated, the boundary conditions assigned to the model, the contact conditions and, finally, the solution procedures.

3.2.1 MODEL GEOMETRY

The roll was modelled as a rigid body and the metal sheet as a deformable body. A rigid body neglects its deformations. Inertia was also not considered because it does not have an influence on the result, since the roll does not accelerate. This deformable-rigid model is shown in Figure 3.7.

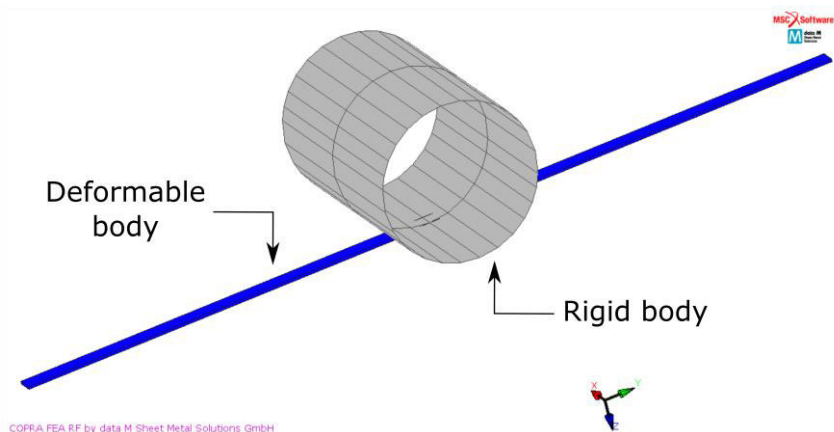


Figure 3.7 - Model geometry of the tribological experiment.

Figure 3.8 shows the global coordinate system used in the model, where x is referred as the transverse direction, y as the longitudinal direction and z as the thickness direction.

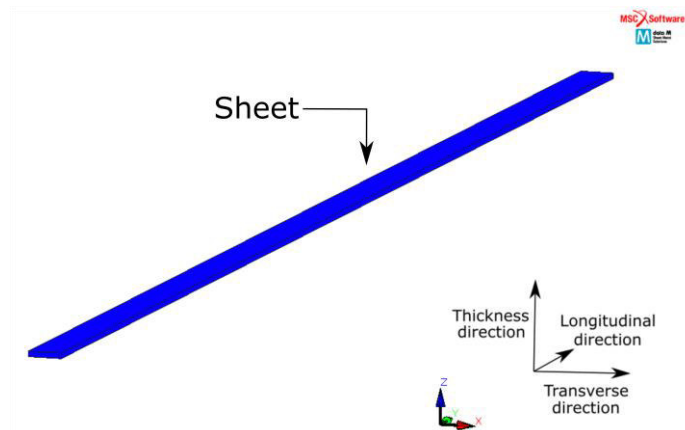


Figure 3.8 - Global coordinate system directions used in the simulation.

A 3D representation was adopted in order to capture the curvature in the transverse direction [MARCINIAK 2002]. In addition, a 3D representation allows to access the full contact area and study the contacting forces distributions along both longitudinal and transverse directions of the sheet surface.

Figure 3.9 represents the acting forces over the contact area for a contact with a torque applied to the roll. The contact normal stress was expected to have a non-uniform distribution but, still, symmetric in the longitudinal and transverse directions [KIM 2015]. The longitudinal and transverse curvatures originate a relative movement between the surfaces in these directions, which, in turn, creates friction forces acting over the contact area. These friction forces were, also, expected to be symmetric in the longitudinal and transverse directions. However, when the roll is sliding over the contact area, a friction force against the movement of the roll is created and the longitudinal symmetry is no longer valid. Therefore, the model is only symmetrical in the transverse direction. Taking advantage of this symmetry, the computational time was reduced by only modelling half of the sheet width. This symmetry has ensured by means of a boundary condition that is outlined in section 3.2.6.

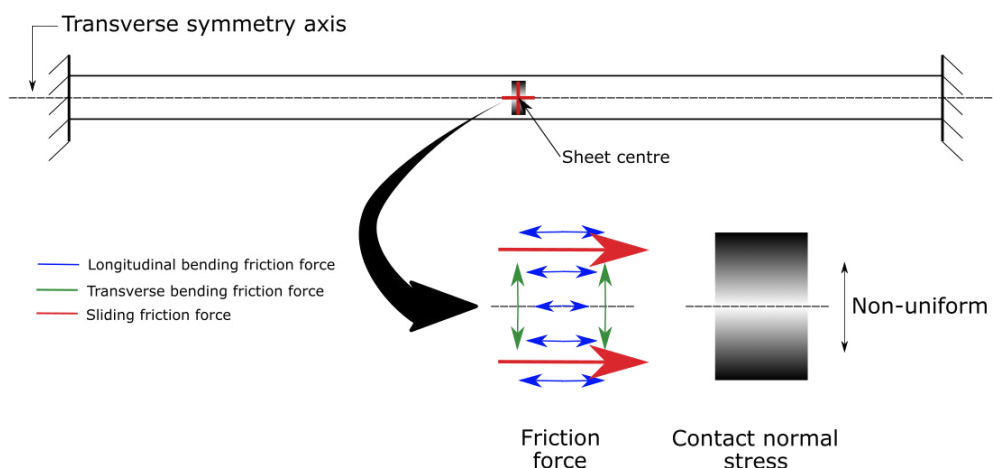


Figure 3.9 - Contact normal stress and friction symmetries for a contact with torque.

The sheet and the roll dimensions are the values used by Galdos et al. [GALDOS 2017] in the physical tribological experiment. These dimensions and the position of the roll with the sheet are illustrated in Figure 3.10. It is worth noticing that the sheet width in the model is 6 mm due to the fact that only half of the sheet width was modelled, as explained above.

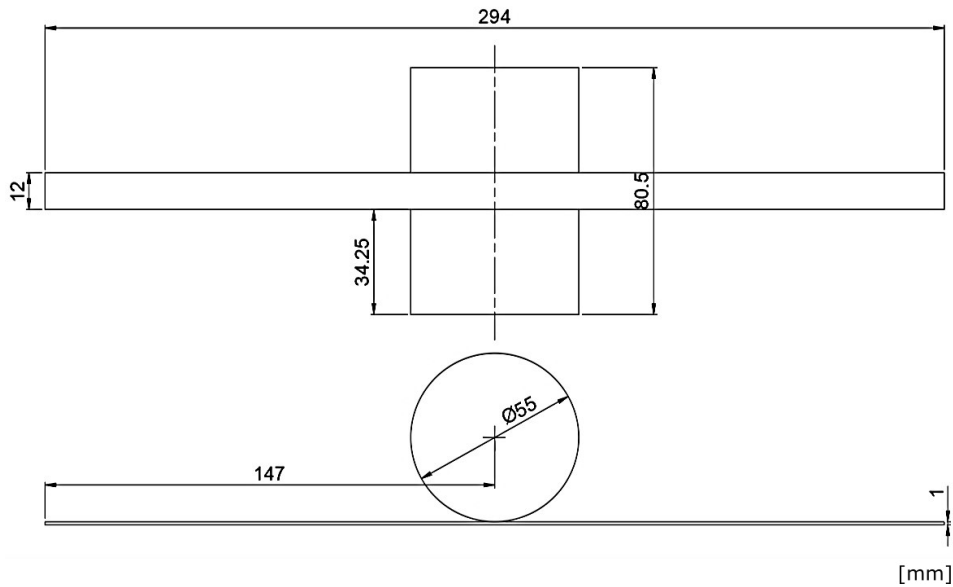


Figure 3.10 - Sheet and roll dimensions.

3.2.2 ELEMENT TYPE

Before introducing the sheet discretisation, the element used for that discretisation is introduced in this section. The 3D deformable body could be discretised using shell or 3D solid elements. The shell elements available in the FEA software used are based in the Kirchhoff plate theory, Raissner-Mindlin plate theory or Koiter-Sanders plate theory [MSC SOFTWARE 2016A]. All theories assume a zero normal stress along the thickness direction [OÑATE 2009], which is not a valid assumption for small bending radii [MARCINIAK 2002]. Therefore, a 3D solid hexahedral isoparametric element with eight nodes (Figure 3.11) was used.

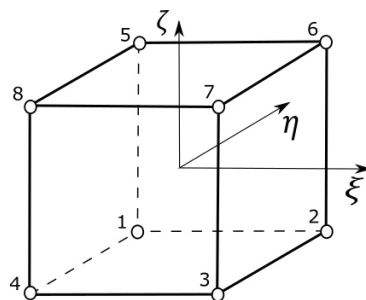


Figure 3.11 - Eight-node hexahedral isoparametric element with its local coordinate system.

The motion of each point in a 3D solid is defined by three components of the displacement vector [OÑATE 2009]

$$\mathbf{u} = [u \quad v \quad w]^T \quad (3.2.1)$$

where

\mathbf{u} is the displacement vector,

u , v and w are the displacement in the cartesian axis x , y and z , respectively.

Discretizing the solid in eight node hexahedral elements, as the one of Figure 3.11, the displacement of a point in the element [OÑATE 2009] is interpolated by

$$\mathbf{u} = \sum_{i=1}^8 \mathbf{N}_i \mathbf{a}_i^{(e)} = \mathbf{N} \mathbf{a}^{(e)} \quad (3.2.2)$$

and the displacement vector for the element [OÑATE 2009] is given by

$$\mathbf{a}^{(e)} = [\mathbf{a}_1^{(e)} \quad \mathbf{a}_2^{(e)} \quad \mathbf{a}_3^{(e)} \quad \mathbf{a}_4^{(e)} \quad \mathbf{a}_5^{(e)} \quad \mathbf{a}_6^{(e)} \quad \mathbf{a}_7^{(e)} \quad \mathbf{a}_8^{(e)}]^T \quad (3.2.3)$$

$$\mathbf{a}_i^{(e)} = [u_i \quad v_i \quad w_i]^T \quad (3.2.4)$$

where

\mathbf{u} is the displacement vector,

\mathbf{N}_i is the shape function matrix of node i ,

\mathbf{N} is the shape function matrix of the element,

$\mathbf{a}_i^{(e)}$ is the displacement vector of node i ,

$\mathbf{a}^{(e)}$ is the displacement vector of the element,

u_i , v_i and w_i are the displacement of node i in the cartesian axis x , y and z , respectively.

The element shape function matrix [OÑATE 2009] is given by

$$\mathbf{N} = [N_1 \quad N_2 \quad N_3 \quad N_4 \quad N_5 \quad N_6 \quad N_7 \quad N_8] \quad (3.2.5)$$

$$\mathbf{N}_i = \begin{bmatrix} N_i & 0 & 0 \\ 0 & N_i & 0 \\ 0 & 0 & N_i \end{bmatrix} \quad (3.2.6)$$

where

\mathbf{N} is the shape function matrix of the element,

\mathbf{N}_i is the shape function matrix of node i ,

N_i is the shape function of node i .

The eight-node element is a Lagrange prism and the shape functions for the element are given by the Lagrange polynomial [OÑATE 2009] function

$$N_i(\xi, \eta, \zeta) = \frac{1}{8} (1 + \xi_i \xi) (1 + \eta_i \eta) (1 - \zeta_i \zeta) \quad (3.2.7)$$

where

N_i is the shape function of node i ,

ξ , η and ζ are the local coordinate axis of the element,

ξ_i , η_i and ζ_i are the coordinates of the node i .

The strain field of the eight-node element is defined by the standard 3D strain elasticity [OÑATE 2009]

$$\boldsymbol{\varepsilon} = [\varepsilon_x \quad \varepsilon_y \quad \varepsilon_z \quad \gamma_{xy} \quad \gamma_{xz} \quad \gamma_{yz}]^T \quad (3.2.8)$$

where

$\boldsymbol{\varepsilon}$ is the strain field vector,

ε_x , ε_y and ε_z are the normal strains,

γ_{xy} , γ_{xz} and γ_{yz} are the shear strains.

The stress field is composed of the six non-zero strains [OÑATE 2009]

$$\boldsymbol{\sigma} = [\sigma_x \quad \sigma_y \quad \sigma_z \quad \sigma_{xy} \quad \sigma_{xz} \quad \sigma_{yz}]^T \quad (3.2.9)$$

where

$\boldsymbol{\sigma}$ is the stress field vector,

σ_x , σ_y and σ_z are the normal stresses,

σ_{xy} , σ_{xz} and σ_{yz} are the shear stresses.

This element uses eight-point Gaussian integration (Figure 3.12).

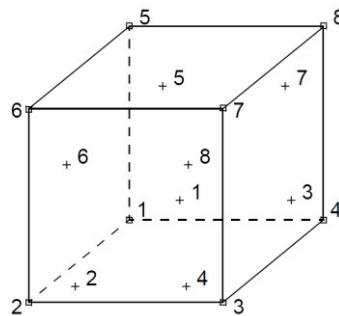


Figure 3.12 - Gauss integration points of the eight-node element. Retrieved from [MSC SOFTWARE 2016B].

A constant dilatation strain in the element was imposed. This was accomplished by a selective integration where the eight Gaussian points are used for the deviatoric contribution of strain and the centroid for the dilatation contribution [MSC SOFTWARE 2016B]. The assumed strain formulation was used to improve the bending characteristics of the element [OÑATE 2009; MSC SOFTWARE 2016B].

3.2.3 METAL SHEET DISCRETISATION

The adopted discretisation has an important influence on the results, as well as on the computational time. In order to find a good relation between accuracy and computational time, a coarse mesh was used and only in the “critical zones” a fine mesh was used. “Critical zones” are the zones with larger variations of the variables involved in the FEA calculations, such as the displacements and acting forces.

In order to better explain the dimension of the elements, in Figure 3.13 the element dimensions nomenclature is defined.

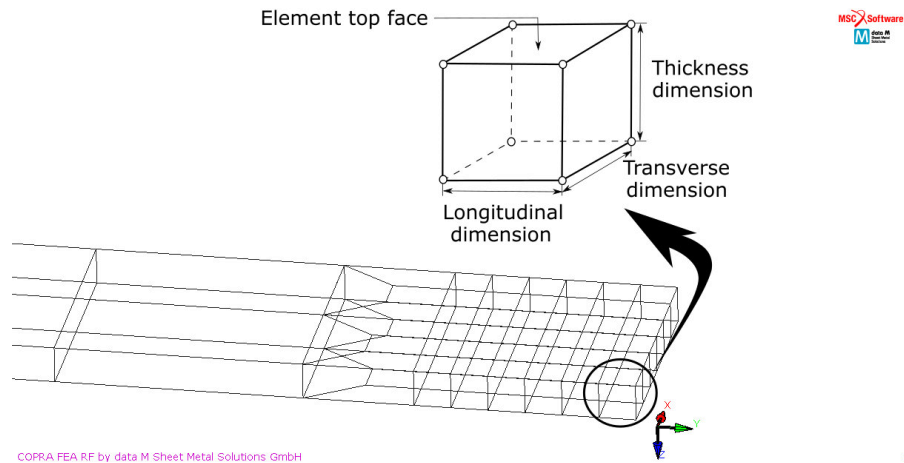


Figure 3.13 - Nomenclature adopted for the element dimensions.

Figure 3.14 shows the global discretisation of the sheet. The displacements of the nodes located in the end faces of the sheet are fixed, which results in a local bending in the “fixed zone”. In the possible contact zone, the sheet will be subjected to contact normal stress and friction stresses. Thus, these zones need a finer mesh to represent these phenomena.

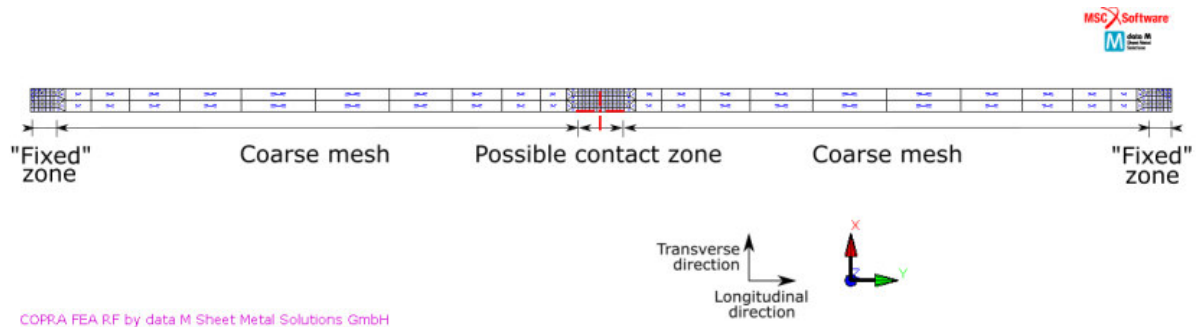


Figure 3.14 - Global mesh discretisation with the different discretisation zones marked.

The thickness discretisation is contact in the longitudinal and transverse and only one element was used (Figure 3.15). However, the thickness discretisation influences the bending representation [OÑATE 2009] and, consequently, the contact description is also expected to be influenced. Therefore the thickness discretisation was investigated in and is presented in section 4.1.3.

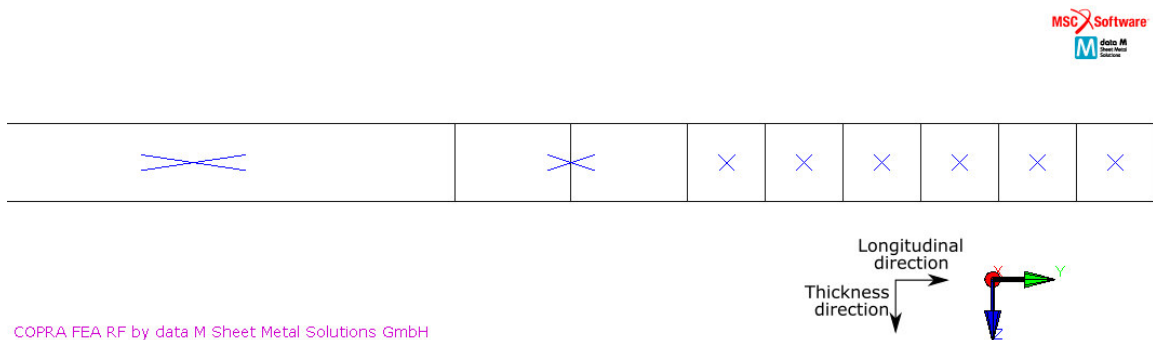


Figure 3.15 - Discretisation of the sheet thickness.

The discretisation of the zone predicted to be in contact – referred as possible contact zone – plays a key role in the study of the contact. This possible contact zone was defined with a length of 12 mm in the longitudinal direction and centred with the sheet centre (Figure 3.16). A contact analysis requires a good discretisation of the contact zone, however, without performing some studies was difficult to define a good discretisation. For this reason, the possible contact zone discretisation was investigated and is presented in section 4.1.1. As a starting point, elements with a transverse and longitudinal dimension of 1 mm were used. This corresponding to twelve elements in the longitudinal direction and six elements in the transverse direction.

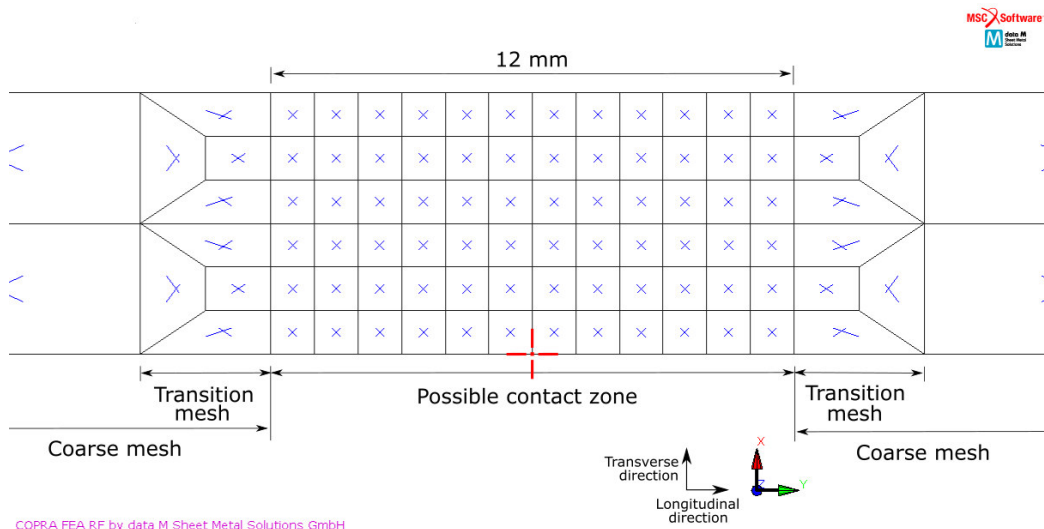


Figure 3.16 - Possible contact zone mesh refinement and correspondent transition.

The “fixed” was defined with a length of 6 mm in the longitudinal direction (Figure 3.17). Elements with a transverse and longitudinal dimension of 1 mm were used, which corresponds to six elements in the longitudinal and transverse direction.

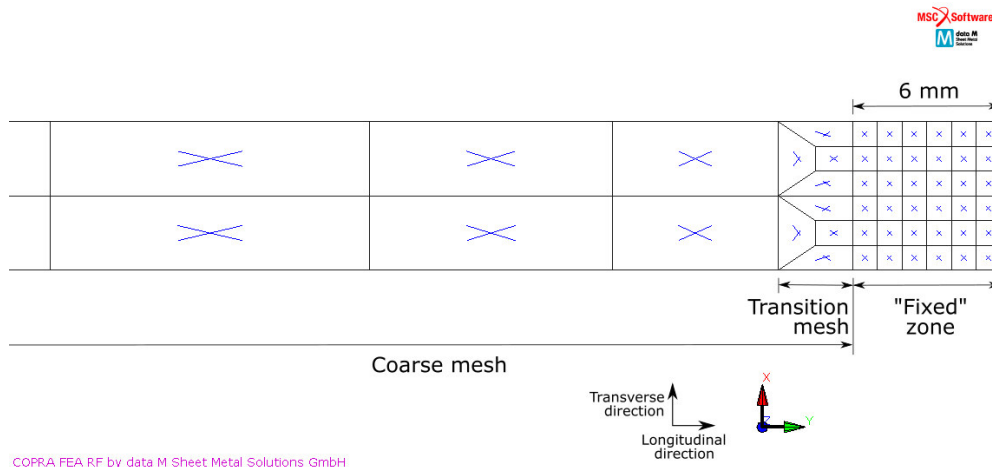


Figure 3.17 - “Fixed” zone mesh refinement and correspondent transition.

For the coarse mesh two elements were used in the transverse direction. Along the longitudinal direction the coarse zone was divided into ten elements with different longitudinal dimensions in order to ensure a smoother transition, as shown in Figure 3.18.

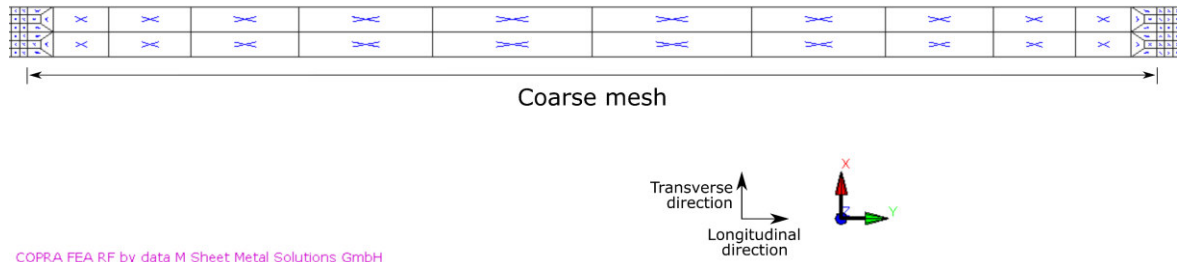


Figure 3.18 - Coarse mesh zone.

3.2.4 MATERIAL MODELLING

A DP 100 steel was used in this model, which was the same material used by Galdos et al. [GALDOS 2017] in the physical tribological experiment. DP 100 is a high-strength steel that has been increasingly used in the automotive industry [GALDOS 2017]. This material was modelled as an elastic-plastic isotropic. Elasticity was modelled using the Hook's law and plasticity using the strain-hardening Swift law. Hooke's law [TIMOSHENKO 1991] is formulated as

$$\bar{\sigma} = E \cdot \bar{\varepsilon}_e \quad (3.2.10)$$

and Swift's law [SWIFT 1952] as

$$\bar{\sigma} = K(\varepsilon_0 + \bar{\varepsilon}_p)^n \quad (3.2.11)$$

where

$\bar{\sigma}_e$ is the equivalent total elastic stress,

$\bar{\varepsilon}_e$ is the equivalent total elastic strain,

E is the Young's modulus,

$\bar{\sigma}_p$ is the equivalent total plastic stress,

$\bar{\varepsilon}_p$ is the equivalent total plastic strain,

K , ε_0 and n are material constants given by the uniaxial tensile test data.

Swift's law parameters were calculated using COPRA® FEA RF software. The Young's modulus (E), Poisson's coefficient (ν), yield strength ($R_{p0.2}$), ultimate tensile strength (R_m) and the percentage of elongation after fracture (A_{80}) given as input data in COPRA® FEA RF for the calculations are stated in Table 3.3.

Table 3.3 – DP 1000 material properties.

E [GPa]	ν [-]	$R_{p0.2}$ [MPa]	R_m [MPa]	A_{80} [%]
202	0.3	928	1060	8

The resulting parameters obtained for the Swift law are shown in Table 3.4.

Table 3.4 - DP1000 parameters used for the strain-hardening Swift law.

K [MPa]	n [-]	ε_0 [-]
1394.57	0.076961	0.0051616

The FEA software used calculates the final curve of the material implementing the elastic behaviour until the elastic limit is reached. This elastic limit is defined as the initial equivalent plastic stress and is determined by making $\bar{\varepsilon}_p = 0$ in equation (3.2.11). The correspondent strain is 0.0046033, therefore, the total equivalent stress [MSC SOFTWARE 2016B] is given by

$$\bar{\sigma} = \begin{cases} E \cdot \bar{\varepsilon} & \text{if } 0 \leq \bar{\varepsilon} \leq 0.0046033 \\ K(\varepsilon_0 + (\bar{\varepsilon} - 0.0046033))^n & \text{if } 0.0046033 < \bar{\varepsilon} \end{cases} \quad (3.2.12)$$

where

$\bar{\sigma}$ is the equivalent total stress,

E is the Young's modulus,

$\bar{\varepsilon}$ is the equivalent total strain,

K , ε_0 and n are material constants given by the uniaxial tensile test data.

The final curve of the material, including the linear elastic and plastic behaviour, is shown in Figure 3.19.

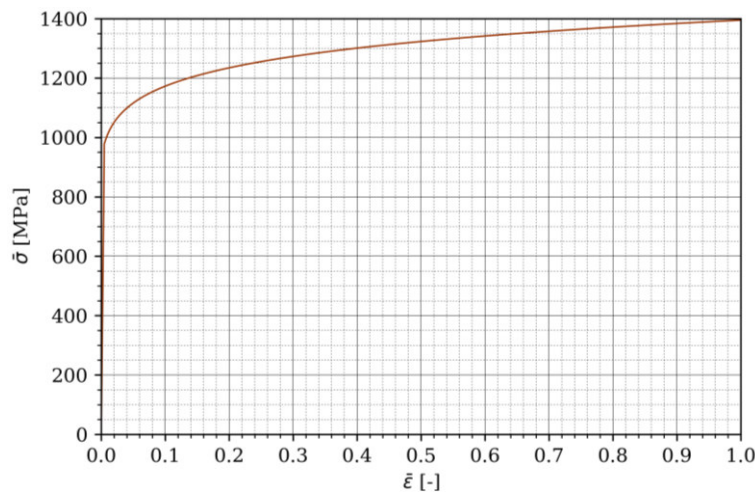


Figure 3.19 - Elastic-plastic strain-hardening model of DP1000 used in the simulation in the model.

3.2.5 LOAD CASES

Different load cases were used for the distinct phases simulated. In this FE model, only the penetration and rotation phases were modeled. Delaying the roll rotation or, in other words, maintaining the roll static in the initial instants of the rotation load case and only applying a constant speed after these instants, both main contact conditions were simulated. These conditions are a contact without sliding friction forces and a contact with sliding friction forces. These sliding friction forces are the forces in the opposite direction of the roll's movement that arise at the contact interface when the roll slides over the contacting surface. Considering that the purpose of this study was to study the contact modelling, the torque load case would not bring additional information. Besides, by only simulating these two load cases, the computational time was reduced.

A prescribed velocity of $1.5 \text{ mm} \cdot \text{s}^{-1}$, equivalent to $0.15 \text{ mm} \cdot \text{increment}^{-1}$ was applied to the roll during the penetration load case. A termination criterion was used to stop the load case

when the roll force reached the values tested in the experiment described in chapter 3.1. In this model, was simulated the mid penetration level and the value was set to 1283.5 N – half of the real value – given the sheet transverse symmetry used in the model.

In the first 0.1 seconds of the rotation loadcase, neither a displacement or a force was applied to the roll. After the 0.1 s, a contact angular velocity is applied to the roll. The roll rotates during 6.3 s at a contact speed of $1\text{ rad} \cdot \text{s}^{-1}$, equivalent to $0.1\text{ rad} \cdot \text{increment}^{-1}$.

The prescribed displacements are applied to the roll by a boundary condition. These boundary conditions and the boundary conditions needed to hold the roll and the sheet are introduced in the following chapter.

3.2.6 PRESCRIBED BOUNDARY CONDITIONS

Boundary conditions to hold the sheet and to ensure the transverse symmetry needs to be applied. These boundary conditions are geometrically represented in Figure 3.20.

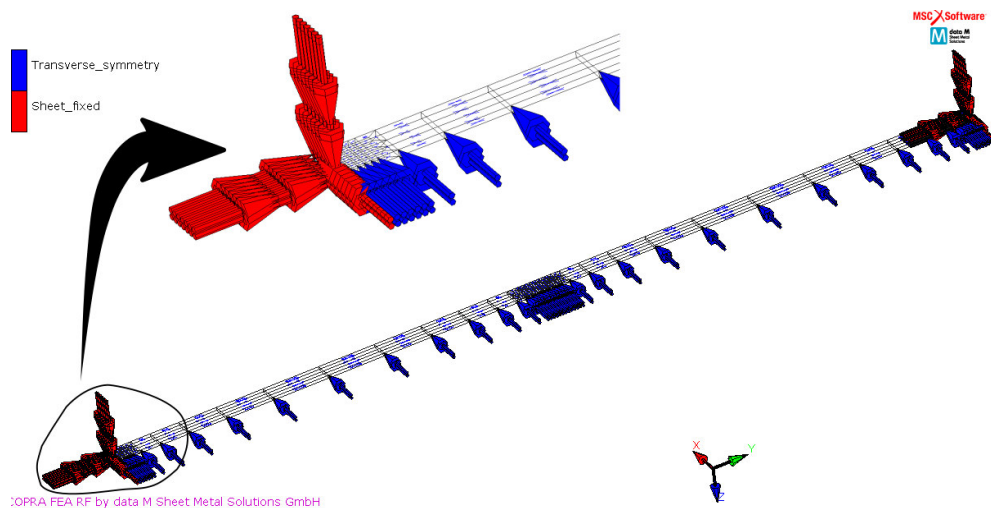


Figure 3.20 - Boundary conditions assigned to the sheet.

The roll is under different conditions during the penetration and the rotation load case. Accordingly, different boundary conditions were applied in each load case, dissimilar to the sheet that is under the same boundary conditions during the entire simulation. During the penetration a prescribed displacement in the perpendicular direction of the sheet – thickness direction – was applied, while, the rotations and displacement in the x and y directions were fixed (Figure 3.21).

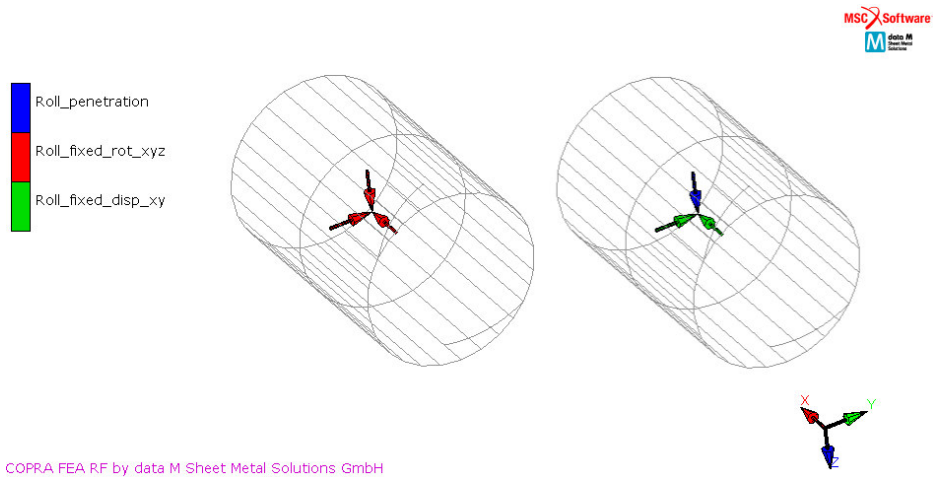


Figure 3.21 - Boundary conditions assigned to the roll during the penetration.

During rotation loadcase, a prescribed rotation was applied in roll axial direction, while the rotation in the y and z directions and the displacements were fixed (Figure 3.22).

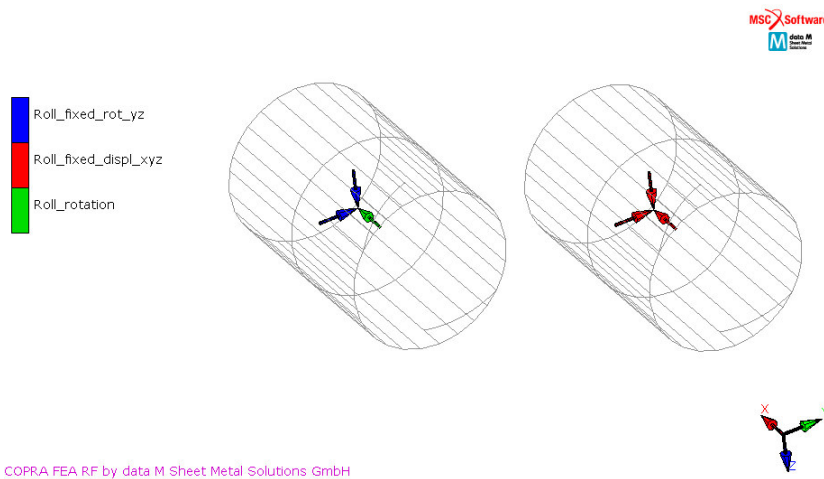


Figure 3.22 - Boundary conditions assigned to the roll during the rotation.

The boundary conditions are summarized in Table 3.5.

Table 3.5 - Purpose of the boundary conditions assigned to the model.

Sheet_fixed	Fixes the DOF of the nodes in the end.
Transverse_symmetry	Fixes the displacement in the transverse direction of the nodes in the symmetry plane.
Roll_fixed_rot_yz	Fixes the rotation of the roll along the y and z axis.
Roll_fixed_rot_xyz	Fixes the rotation of the roll along the x, y and z axis.
Roll_fixed_disp_xy	Fixes the displacement of the roll in the x and y direction.
Roll_fixed_disp_xyz	Fixes the displacement of the roll in the x, y and z direction.

3.2.7 CONTACT CONDITIONS

The FEA software used allows to use a segment to segment (STS) or a node to segment (NTS) contact. Since the STS algorithm is still under development [MSC SOFTWARE 2016A], the NTS was adopted in this modelling. The NTS algorithm is based on nodes being in contact with a segment [MSC SOFTWARE 2016A]. In this simulation, the nodes are part of the sheet mesh and the segments belongs to the roll's surface. In other words, the mesh was selected as the slave body and the roll as the master body. Additionally, only a contact between the sheet and the roll was selected as possible.

In COPRA® FEA RF the contact search is based on a contact tolerance. The contact distance tolerance defines the distance normal to the surface at which a node is in contact with a segment, as shown in Figure 3.23. The value specified by the user is a percentage of the smallest element edge, in another word, a defined value of 0.05 means a contact distance tolerance is equal to 0.05 times the smallest element edge [MSC SOFTWARE 2013].

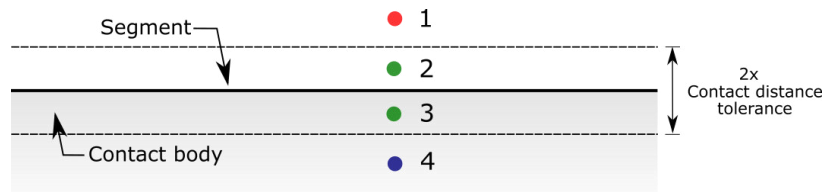


Figure 3.23 - Representation of the contact distance tolerance and contact status for nodes in a different position, using green for nodes in contact, red for non-contacting nodes and blue for penetrating nodes.

Node number 1 of Figure 3.23 is outside the body and outside the distance tolerance, so it is not in contact. Nodes number 2 and 3 are inside the contact distance tolerance, so they are in contact and are projected onto the segment. Once in contact, contact constraints are applied, and the node remains in contact if the necessary force to keep the node in contact is less than the user defined separation force. Node number 4 is penetrating the body and, in such cases, the increment is recycled with modified time step [MSC SOFTWARE 2013].

For models with areas where nodes are almost touching the surface – for example, the entry and exit of the rolls in a rolling analysis – it is recommended to use a smaller distance on the outside and a larger distance in the inside of the surface. This difference in the contact tolerance is accomplished by defining a biased tolerance, as shown in Figure 3.24. The bias factor is a value between 0 and 0.99 defined by the user [MSC SOFTWARE 2016A].

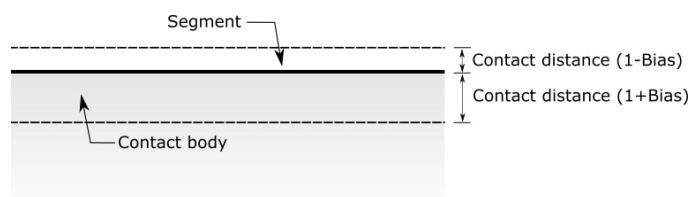


Figure 3.24 - Biased contact tolerance.

The contact distance tolerance and the bias factor can be defined as a parameter of the model. However, no information about these values was found in previous studies. At this point it

is not possible to draw a conclusion, but, considering its importance in the contact representation, a study of these parameters was performed. This study is presented in section 4.2. As a starting point for the study, the default values of the FEA software were adopted. Thus, a contact distance tolerance of 0.05 and a bias factor of 0.95 were used.

The friction models available in the FEA software used are stated in Figure 3.25. As previously mentioned in section 2.2.4, in metal forming simulations the friction is assumed to follow Coulomb friction law or the constant shear friction law. The constant shear friction law neglects the effects of the normal stress on the frictional stress. Since it is clear that frictional stress is related to the normal stress, the Coulomb friction law can describe better the real behaviour of friction [JOUN 2009].

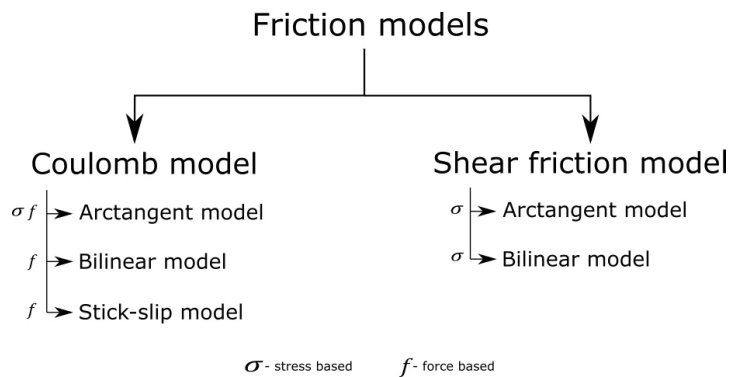


Figure 3.25 - Friction models and correspondent numerical implementation supported by COPRA® FEA RF.

Within the Coulomb friction law, the FEA software used allows three different numerical implementations (Figure 3.26Figure 4.81). In this model, a Coulomb stick-slip model was adopted with a static and dynamic friction coefficient of 0.1325 and 0.1475, respectively. Given the importance of the friction model in the contact modelling, this parameter was studied in more detail. This study is presented in section 4.3.

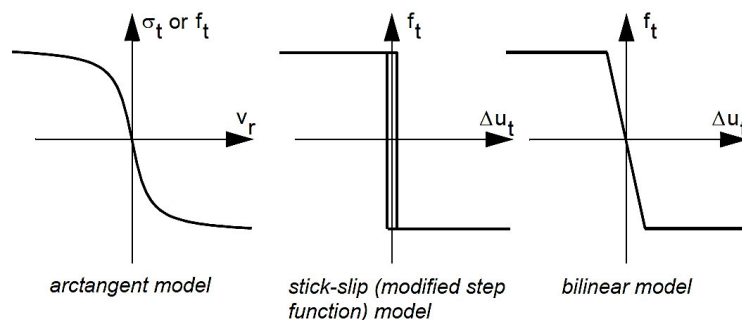


Figure 3.26 - Friction numerical models available in COPRA® FEA RF. Retrieved from [MSC SOFTWARE 2016A]

3.2.8 SOLUTION PROCEDURES

The tribological experiment was modelled as a nonlinear analysis. Therefore, a nonlinear solution procedure needs to be established. The formulation of the continuum mechanics

incremental equations of motion was performed using the large strain updated Lagrange formulation. The integration procedure used to solve the set of nonlinear equations was the Newton-Raphson method. Firstly, this root-finding algorithm is applied locally to solve the consistency condition and find the nodes in contact. Then, the boundary contact forces – contact normal stress and contact friction stress – are determined and computed in the equilibrium equations. This nonlinear system of equation is solved iteratively using the Newton-Raphson method to calculate a possible solution for the problem. The solution convergence during the iteration process was checked based on the relative residual forces with a relative residual force tolerance set to 0.1.

4 OPTIMISATION OF THE FE MODEL

Chapter 3.2 presents the finite element (FE) modelling of the physical experiment. An FE model provides a FEM simulation of this experiment and make it possible to study the process. In the physical experiment, the contact area is inaccessible for observation and the acting forces over this contact area are not possible to be measured at each instant. A FEM simulation of the experiment overcomes this barrier and allows to access that contact area and calculate the contacting forces at any instant. However, the model needs to be optimised in order to have a good representation

This chapter presents the optimisation of the FE model with a focus on the contact representation. The study is divided in three parts: mesh discretisation, contact search and friction modelling. The mesh discretisation study aims to improve the contact representation by optimising the mesh discretisation. The contact search aims to study the influence of the contact detection in the contact representation. Finally, the friction modelling aims study the friction influence on contact representation and compare different friction models.

4.1 MODEL SENSITIVITY TO THE MESH DISCRETISATION

The mesh discretisation may have an influence on the contact characterisation, therefore, the sensitivity of the results to the mesh discretisation was studied.

As a starting point, the model presented in chapter 3.2 was used. Firstly, the possible contact zone discretisation in the longitudinal and transverse directions is analysed in section 4.1.1. Following the results of this study, section 4.1.2 presents a study of the maximum contact normal stress location. Then, section 4.1.3 presents the optimisation of the thickness discretisation. Additionally, the influence of adopting a mesh with transitions is presented in 4.1.4 and, lastly, the study of the nodes location with the roll axis is presented in 4.1.5.

4.1.1 CONTACT ZONE DISCRETISATION IN THE LONGITUDINAL AND TRANSVERSE DIRECTIONS

This section presents the study of the contact zone discretisation in the longitudinal and transverse directions. This study aims to understand the influence of this parameter in the contact representation and find an optimal value. The optimal value was assumed to be the one providing an accurate representation of the contact without implicating an unsustainable computational cost. Given the contact inaccessibility for observation, it was not possible to be sure about the right contact representation. However, when the tribological experiment is simulated with different parameters and the calculated forces on each simulation converge to the same value, those parameters can be assumed to accurately represent the contact conditions.

Initially, the bending geometry and the evolution of the roll force during the penetration phase were analysed in order to, first of all, understand this parameter influence on the bending representation. Then, the study focused on the results with a direct influence on the contact representation. Thus, the convergence of the contact area, maximum contact normal stress, mean contact normal stress and dynamic torque were analysed. Furthermore, the maximum contact normal stress evolution during the penetration phase was also studied, followed by a comparison of the contact normal stress distribution in each simulation.

The model presented in 3.2 was used in this study and only the possible contact zone discretisation was changed. Six different discretisations of the possible contact zone (defined in Figure 3.14) were modelled. The top face of the elements (defined in Figure 3.13) were modelled as a square, meaning that the elements have an equal longitudinal and transverse dimension. The size of that square is defined will be referred in this paper as the mesh size. The different mesh sizes studied were 0.167 mm , 0.250 mm , 0.333 mm , 0.429 mm , 0.500 mm and 1.000 mm , which the correspondent discretisations are illustrated in Figure 4.1. The thickness was discretised into one element in all models (1 mm).

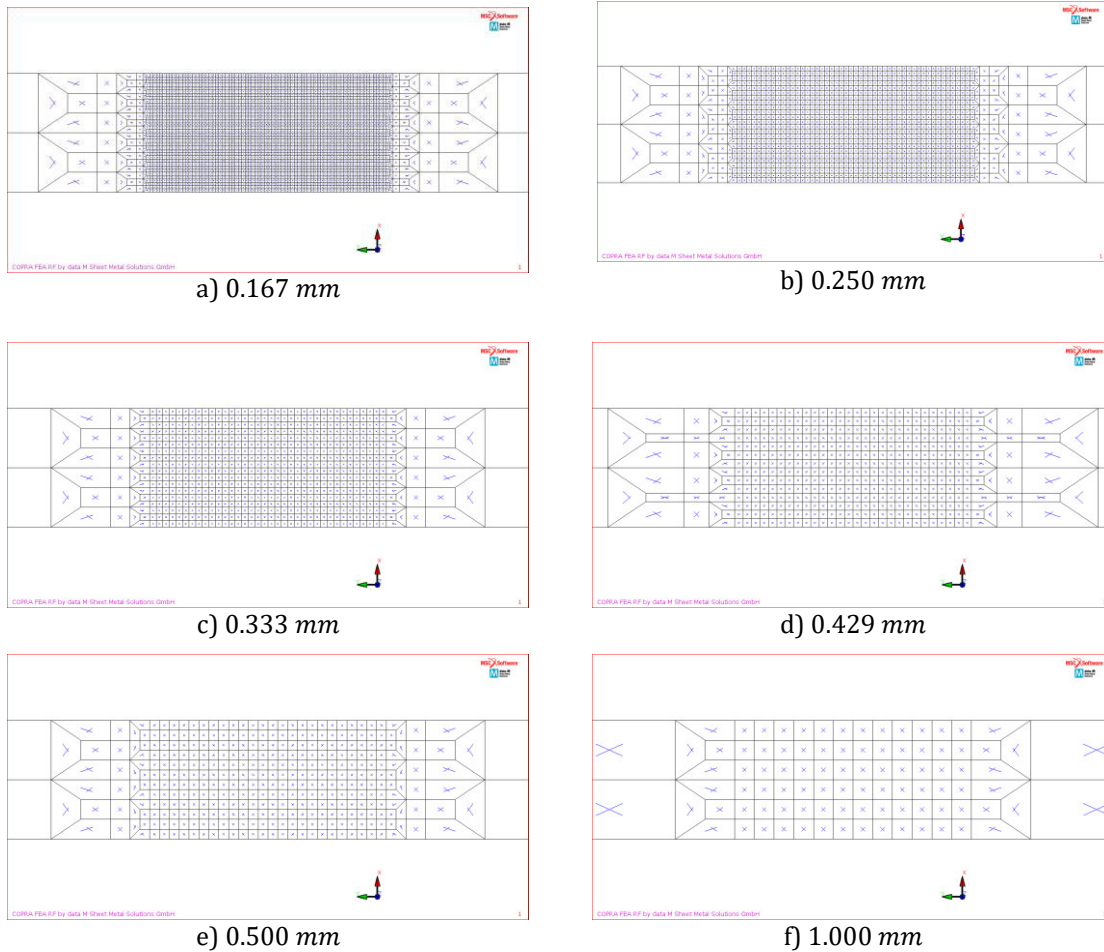


Figure 4.1 - Different discretisations studied for the possible contact zone.

The bending geometry was studied by analysing both the longitudinal and transverse bending geometry. Figure 4.2 illustrated the path used for the longitudinal bending representation. This path corresponds to the set of nodes of which the position y and the displacement w (z direction) were collected. The path is located in the inner surface of the sheet and over the transverse symmetry plane.

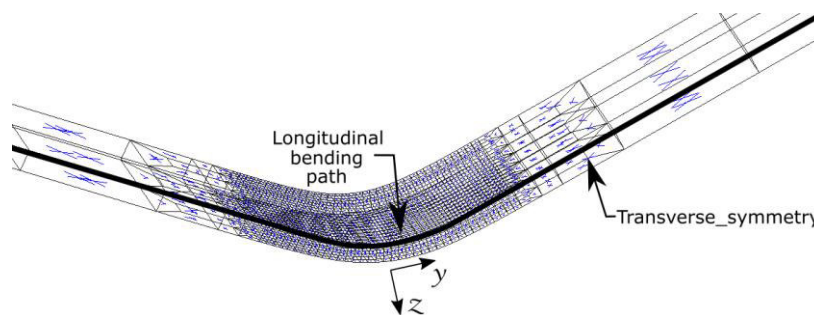


Figure 4.2 - Path used for the longitudinal bending representation.

Figure 4.3 illustrates the path used for the transverse bending representation, which is located in the inner surface and over the bending axis.

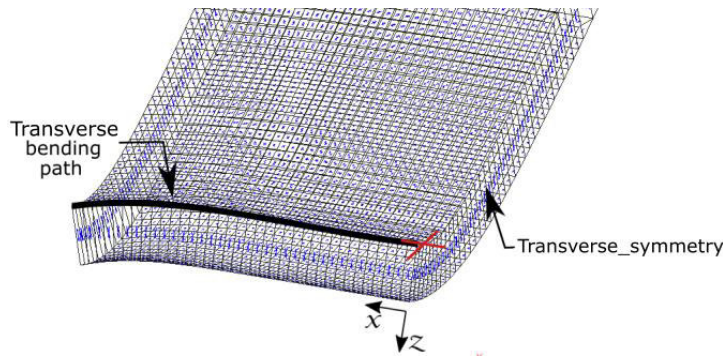


Figure 4.3 - Path used for the transverse bending representation.

The longitudinal bending geometry at the last increment of the penetration was represented using the path defined in Figure 4.2. Figure 4.4 illustrates this longitudinal bending geometry for the different mesh sizes modelled. The abscissa corresponds to the position y and the ordinate corresponds to the displacement w .

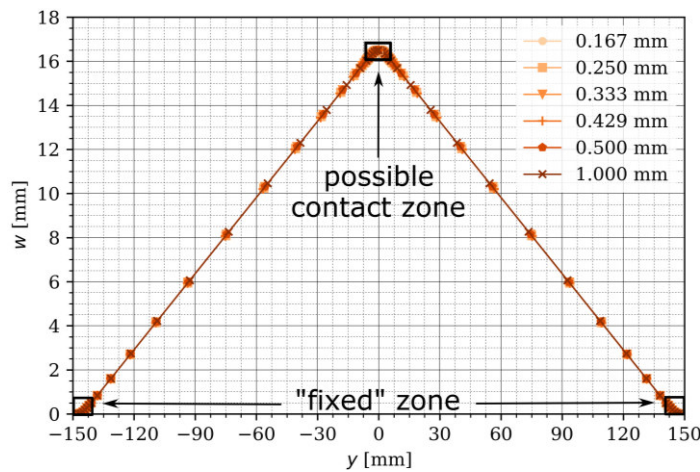


Figure 4.4 - Geometry of the longitudinal bending at the last increment of the penetration for the different mesh sizes.

In order to obtain a clearer representation of the longitudinal bending geometry, the critical zones, which are pointed out in Figure 4.4, are represented separately in Figure 4.5 and Figure 4.6. The first one illustrates the longitudinal bending for the possible contact zone and the second ones illustrates the longitudinal bending for the “fixed” zone.

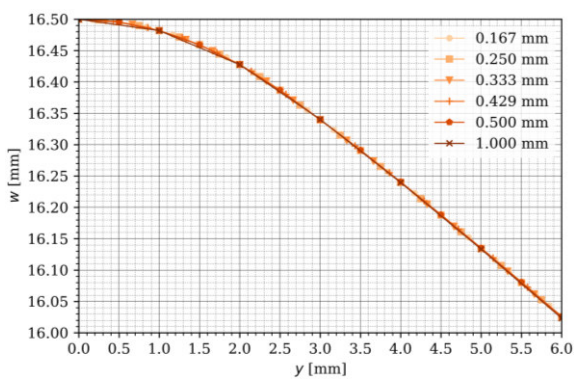


Figure 4.5 - Geometry of the longitudinal bending zone at the last increment of the penetration for the different mesh sizes; representation for the possible contact zone.

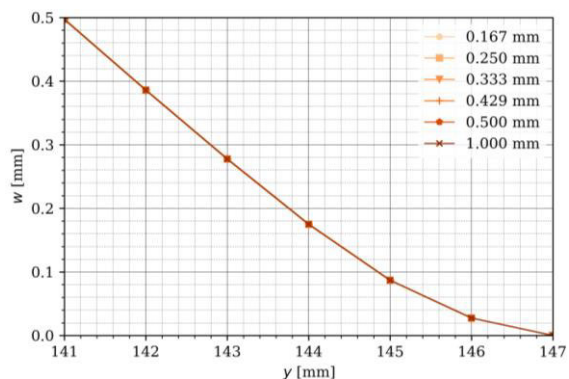


Figure 4.6 - Geometry of the longitudinal bending at the last increment of the penetration for the different mesh sizes; representation for the “fixed” zone.

A closer look to the bending geometry represented in Figure 4.5 and Figure 4.6 shows coincident lines for each mesh size. Therefore, the range of mesh sizes studied does not influence the bending geometry.

Using the path defined in Figure 4.3, a graphical representation of the transverse bending at the last increment of the penetration was created. Figure 4.7 illustrates this representation for the different mesh sizes. The abscissa corresponds to the position x and the ordinate corresponds to the displacement w of each node.

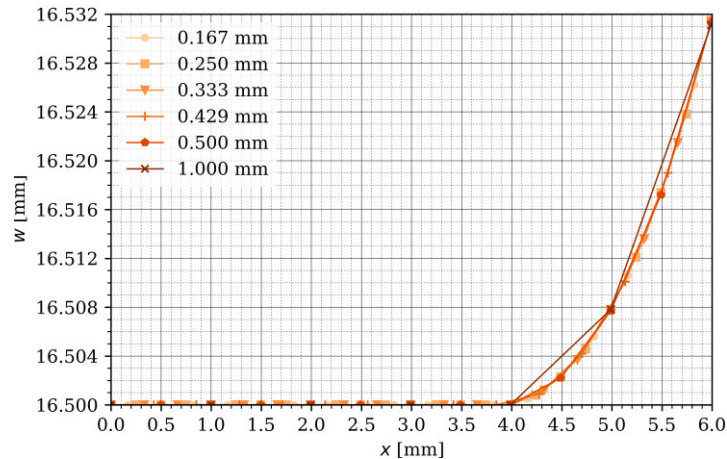


Figure 4.7 – Geometry of the transverse bending at the last increment of the penetration for the different mesh sizes.

An analysis of Figure 4.7 shows that when the different mesh sizes have nodes with a coincident position x , the displacement w are equal. However, the number of elements in the mesh size of 1 mm is not enough to represent a defined curvature.

The sheet bending results from the roll moving against it and, for the roll to move the prescribed displacement, a force needs to be applied on the roll (F_{roll}). The evolution of this force during the penetration was analysed for the different mesh sizes and its representation is shown in Figure 4.8. An observation of the data shows that the roll force needed to move the roll is not influenced by the mesh size.

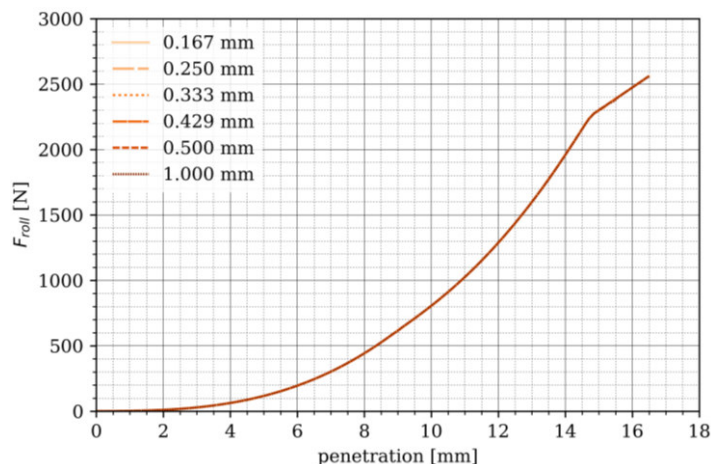


Figure 4.8 - Roll force during the penetration for the different mesh sizes.

The study continued with an analysis of the parameter influence on the contact representation. Key parameters of the contact representation are the contact area (A), contact normal stress (σ_n) and the dynamic torque (τ_d). Thus, a study of these parameters convergence with the mesh size was performed. Figure 4.9 represents the mesh dependency on the variables: contact area (A), maximum contact stress (σ_n^{max}), mean contact normal stress (σ_n^{mean}) and the dynamic torque (τ_d). The contact area, as well as the maximum and mean contact normal stress were calculated at the last increment of the penetration. The dynamic torque corresponds to the torque obtained when the roll rotates with a constant angular velocity. The mean contact normal stress was calculated by summing all values of each node over the contact area and dividing by the number of nodes in contact, as follows

$$\sigma_n^{mean} = \frac{1}{N} \sum_{i=1}^N \sigma_{n_i} \quad (4.1.1)$$

where

- σ_n^{mean} is the mean contact normal stress,
- N is the number of nodes in contact,
- σ_{n_i} is the contact normal stress of node i .

Each value in the graphical representation represents its relative error using the finer mesh as the reference value for this calculation. Negative relative errors represent values lower than the reference - 0.167 mm mesh size - and positive errors represent values higher than the reference.

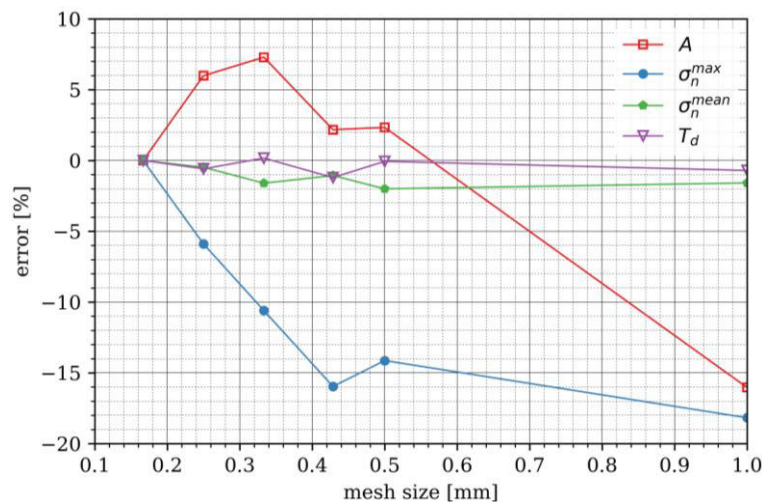


Figure 4.9 – Relative error of the contact area (A), maximum contact normal stress (σ_n^{max}), mean contact normal stress (σ_n^{mean}) and dynamic torque (T_d) using the finer mesh as the reference.

The dynamic torque was not influenced by the possible contact zone discretisation. This result was expected considering that the sliding velocity is constant along the cylinder width – transverse direction. For a mesh size equal or lower than 0.5 mm, the contact area relative error is lower than an absolute value of 7.3%. Therefore, a mesh size lower than 0.5 mm can be considered a reasonable approximation of the contact area.

The mean contact normal stress was within an error of 2 % absolute value, unlike its maximum value. This approximately constant value can be explained by the fact that the roll force pushing the roll against the sheet is the same in all simulations. Thus, it originates the same amount of contact pressure, even though the mesh size influences the contact pressure distribution. The maximum contact normal stress shows a tendency to increase when the size of the mesh decreases. This observed relation is, possibly, due to the contact normal stresses concentration in a small region and, therefore, a smaller discretisation provides a better representation of the high slopes in that region.

Contact normal stress's evolution during the penetration can be seen in Figure 4.10. The maximum contact normal stress increased until a peak was reached and decreased from this point. In that decreasing phase, the curves for a mesh size lower than 1 mm converged. The maximum contact normal stress showed a tendency to increase with smaller values of the mesh size, except for a 0.167 mm mesh size. It is visible that the curves of the 0,167 mm, 0,250 mm and 0,333 mm mesh size have a similar definition.

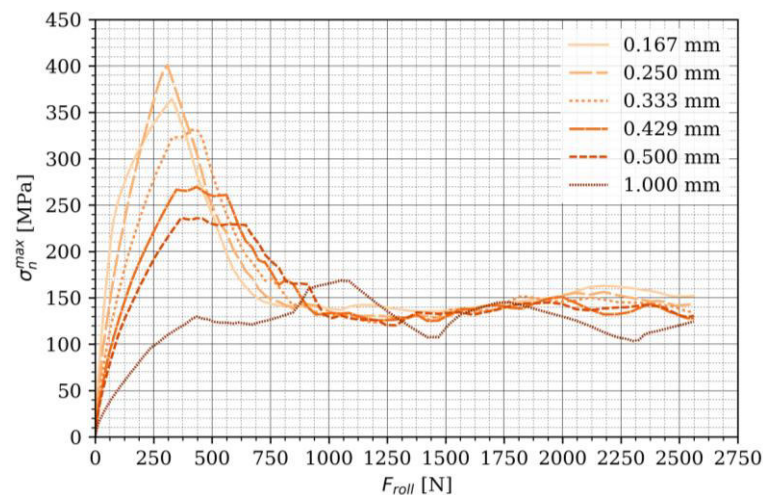


Figure 4.10 - Maximum contact normal stress during the penetration.

Given the importance of obtaining a good representation of the contact interaction between the roll and the sheet, the contact normal stress distribution was analysed in detail. Figure 4.11 shows the contact normal stress representation for the different mesh sizes. The maximum value node is indicated in black.

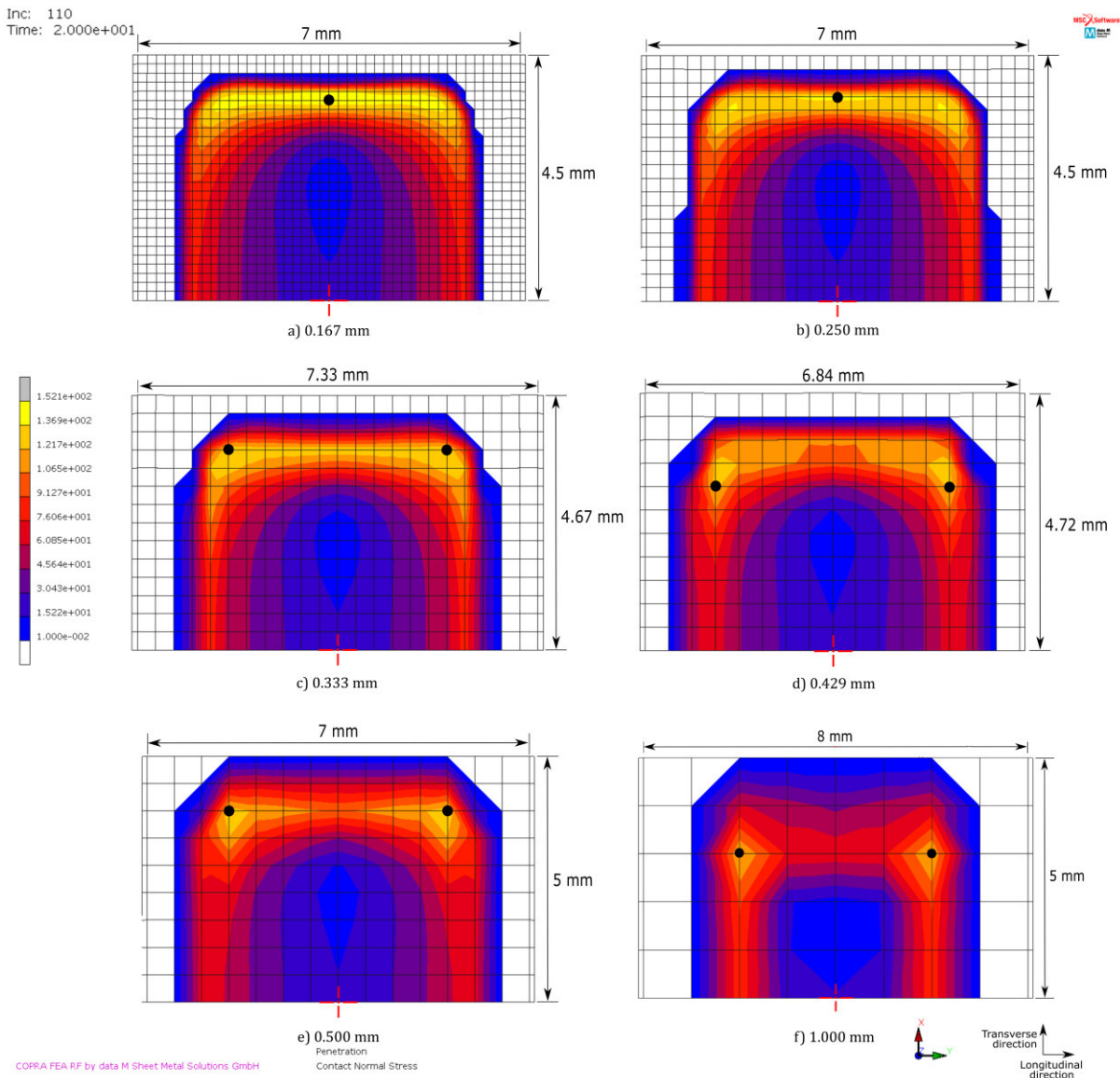


Figure 4.11 - Contact normal stress distribution in the contact area for different mesh sized and with the maximum value pointed out; calculated at the last increment of the penetration.

The contact normal stress distribution for a mesh size equal or lower than 0.333 mm shows similar distributions, except for the location of the maximum. For a mesh size equal or higher than 0.333 mm, the maximum contact normal stress is reached at the edges, exhibiting four points with the maximum contact normal stress – four-point contact. In the images of Figure 4.12 only two points are represented, however, these images represent only half of the sheet width. A different representation was observed in the finer meshes (0.167 mm and 0.250 mm) where the maximum value is located in the centre line. In these cases, the maximum contact normal stress is reached in two points – two-point contact. In order to better understand this difference, a representation of the contact normal stress along an axis passing through the location of the two maximum values (Figure 4.12) was calculated. Only the 0.167 mm mesh size was compared with the 0.333 mm mesh size given the fact that the second one has elements with a dimension double of the elements in the first one. Consequently, a line of nodes is coincident in both meshes. Other

combinations could have been used, however, the purpose of this investigation was to compare the distinct behaviours using the finest mesh as the reference for this comparison.

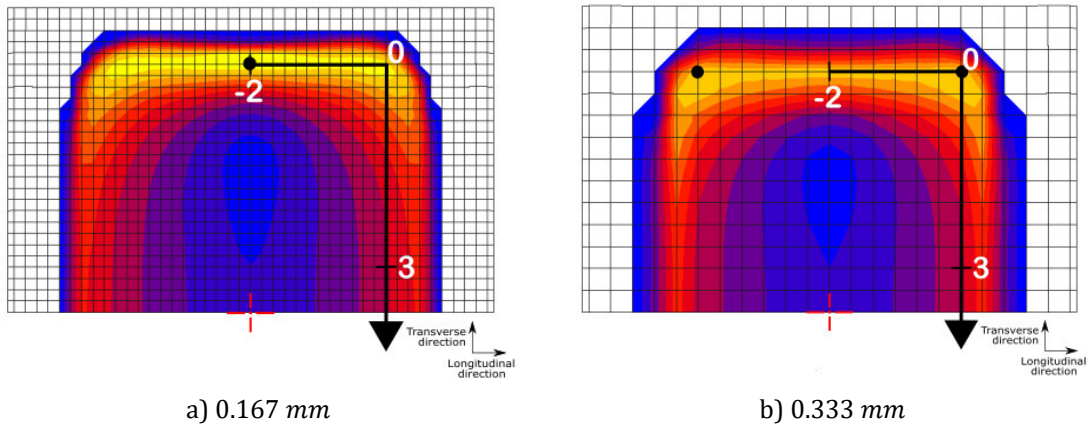


Figure 4.12 - Axis used for the contact normal stress graphical representation.

Figure 4.13 represents the contact normal stress along the axis illustrated in Figure 4.12. The abscissa represents the distance along the axis defined in Figure 4.12 and the ordinate represents the contact normal stress. It was observed that the contact normal stress is, approximately, the same along the transverse direction and only differed along sheet longitudinal direction. For the mesh size of 0.167 mm , the contact normal stress does not show a good definition, having oscillations along the longitudinal direction. The curve for the 0.333 mm mesh size has its maximum value in the corner of the contact area $-x = 0$ and decreased along the longitudinal direction towards the centre line $-x = -2$. Both curves tend to a maximum value in the centre line.

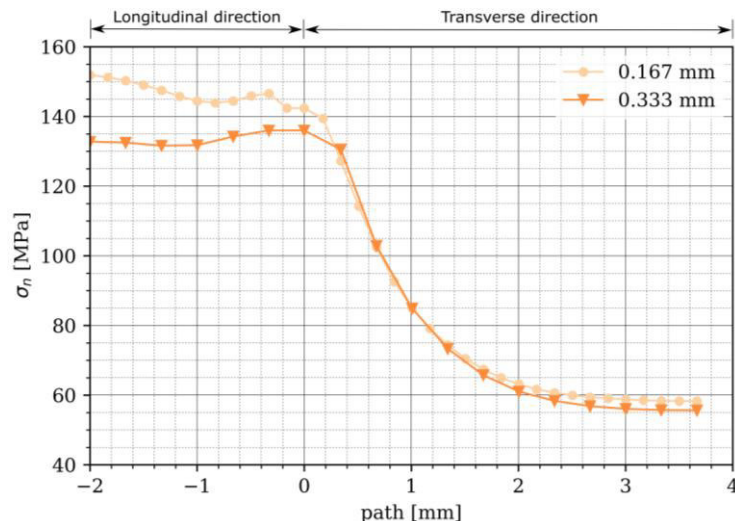


Figure 4.13 - Contact normal stress along the path crossing the nodes with the maximum normal stress.

In order to find a good relation between accuracy and computational cost, the computational time was also analysed. Figure 4.14 represents the computational time required for the simulations with different mesh sizes. A lower element size corresponds to a higher number of elements and, consequently, a higher computational cost.

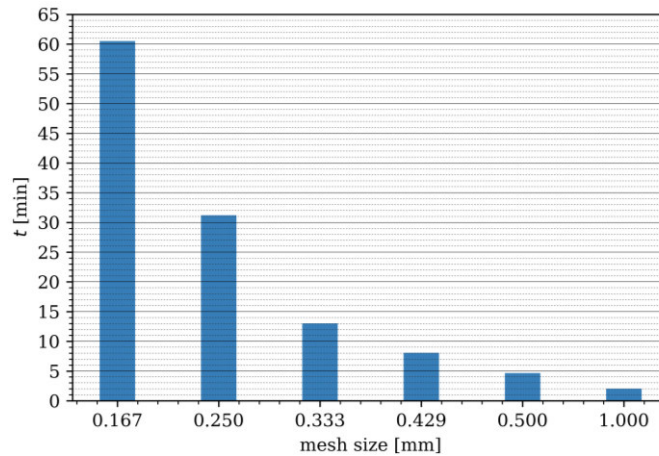


Figure 4.14 - Simulation computational time of the different sizes used in the possible contact zone.

The 0.250 mm mesh size took 31.2 min to simulate in contrast with the 0.333 mm that only took 13.0 min, which corresponds to a decrease of 58 % in the computational time. Even though the computational time continues to decrease with the increase mesh size, the decreasing slope is lower.

Recapping, the longitudinal bending geometry is not influenced by the discretisation of the possible contact zone in the longitudinal and transverse directions. Regarding the transverse bending geometry, only the 1 mm mesh size shows that the number of nodes it has along the transverse direction is not enough to represent the transverse curvature. The roll force is not influenced by this discretisation, either. However, when focusing on the contact different representations were observed for the different mesh sizes. In order to represent the contact area with an absolute relative error lower than 7.3 %, a mesh size equal or lower than 0.5 mm is needed. On the other hand, the maximum contact normal stress evolution only tends to converge for a mesh size lower or equal than 0.333 mm. Also, the contact normal stress distribution at the last increment of the penetration suggests that a mesh size equal or lower than 0.333 mm provides a good representation. However, a mesh size equal or higher than 0.333 mm exhibits a four-point contact and the 0.250 mm 0.167 mm mesh size exhibits a two-point contact.

Considering that the mesh sizes of 0.333 mm, 0.250 mm and 0.167 mm show similar results, differing only on the location of the maximum contact normal, the contact normal stress location was investigated. Taking in consideration also the computational time, the study proceeded using the mesh sizes of 0.333 mm and 0.167 mm.

4.1.2 INVESTIGATION OF THE MAXIMUM CONTACT NORMAL STRESS LOCATION

This section outlines the study of the maximum contact normal stress location and aims to investigate the difference between a two-point contact and a four-point contact by improving the thickness discretisation. The elements in the possible contact zone for the mesh size of 0.167 mm have a longitudinal and transverse dimension of 0.167 mm and a thickness dimension of 1 mm. This thickness dimension is six times higher than the square top face dimension and the high element aspect ratio was assumed as a possible cause for inaccurate results. Thus, six

elements along the thickness were used in order to have a low element aspect ratio (1:1 or almost cubic).

The bending geometry and the evolution of the roll force during the penetration phase were analysed at first. Then, the maximum contact normal stress evolution during the penetration phase was analysed, followed by a comparison of the contact normal stress distribution in each simulation.

The process described in the paragraph above was first executed for a comparison between a thickness discretisation of one element and six elements. For this comparison two models were created. Both models were modelled with the possible contact zone being discretised with a mesh size of 0.167 mm in the longitudinal and transverse directions. One model has the thickness discretised into one element and the other has six elements. Following, the process described above was also executed for a comparison between a mesh size of 0.167 mm and 0.333 mm . Two models were created and, this time, the thickness discretisation was maintained the same. Both models have six elements over the thickness and a possible contact zone discretised with a mesh size of 0.167 mm and 0.333 mm .

In all models used, only one-quarter of the metal sheet was modelled given the fact that it was only analysed the sheet behaviour during the penetration. To ensure symmetry in the transverse direction a boundary condition was added (Longitudinal_symmetry), as shown in Figure 4.15. The penetration load case was stopped when a roll force of 641.75 N was reached, which corresponds to one quarter of the experimental force.

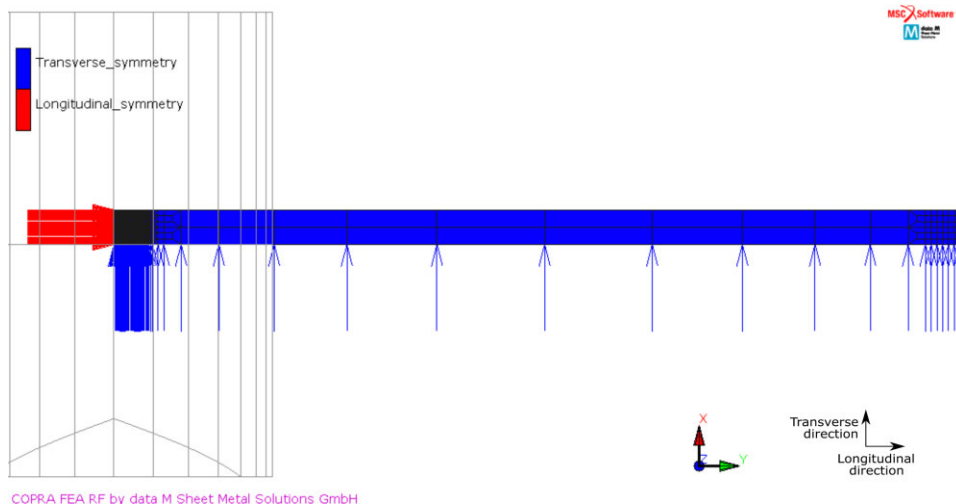


Figure 4.15 - Symmetry conditions used in the study of the maximum contact normal stress location.

The longitudinal and transverse bending geometry were characterised using the path previously illustrated in Figure 4.2 and Figure 4.3. Figure 4.16 compares the longitudinal bending in the contact zone, obtained in the last increment of the penetration.

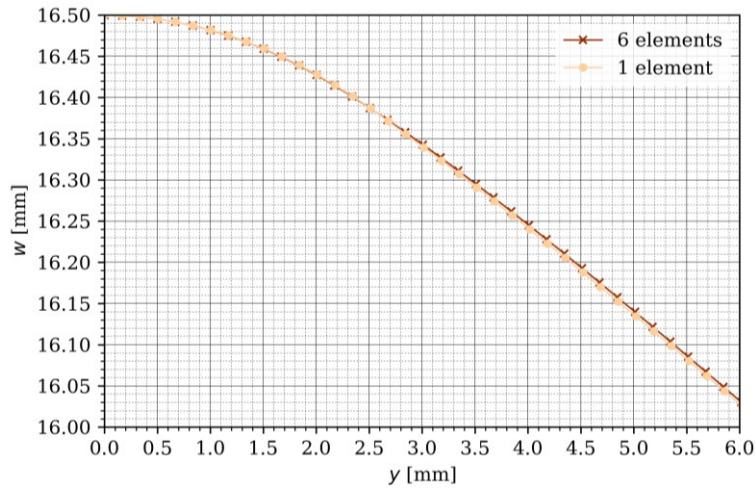


Figure 4.16 - Longitudinal bending geometry for the possible contact zone, at the penetration last increment, using different thickness discretisation and a 0.167 mm mesh size.

Figure 4.17 compares the longitudinal bending for the “fixed zone”, obtained at the penetration last increment.

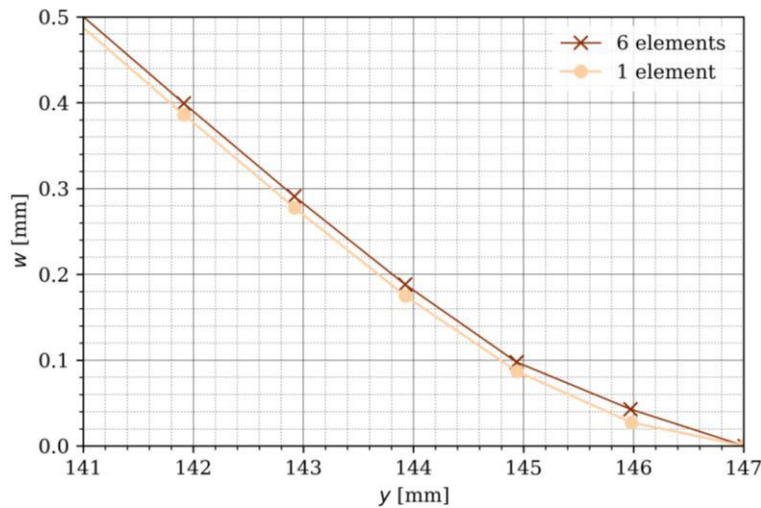


Figure 4.17 - Longitudinal bending geometry in the “fixed zone”, at the penetration last increment, using different thickness discretisation and a mesh size of 0.167 mm.

The points in Figure 4.16 and Figure 4.17 are not coincident, which suggests that the thickness discretisation influences the bending representation.

As seen in Figure 4.18, the geometry of the transverse bending also shows differences when the thickness was discretised into six elements. These differences suggest that a better thickness discretisation improves the bending representation.

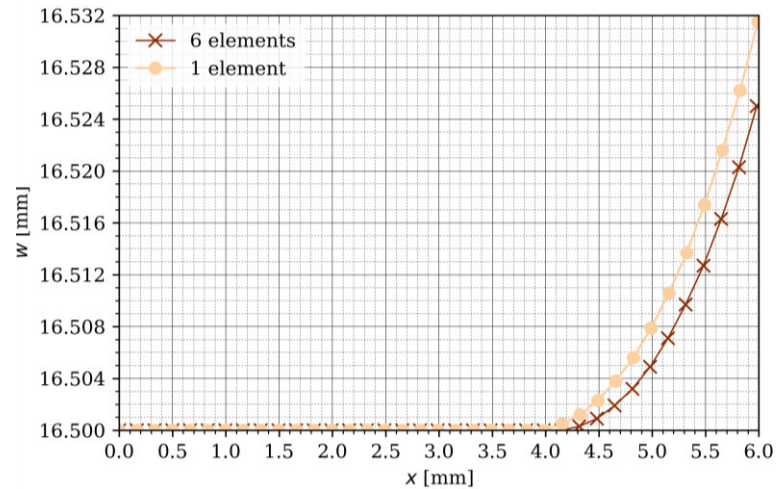


Figure 4.18 - Transverse bending geometry, at the last increment of the penetration, using different thickness discretisation and a mesh size of 0.167 mm .

Analysing the roll force during penetration, differences were observed. Figure 4.19 shows a slightly higher roll force for the simulation with six elements between a penetration of 10.31 mm and 14.44 mm .

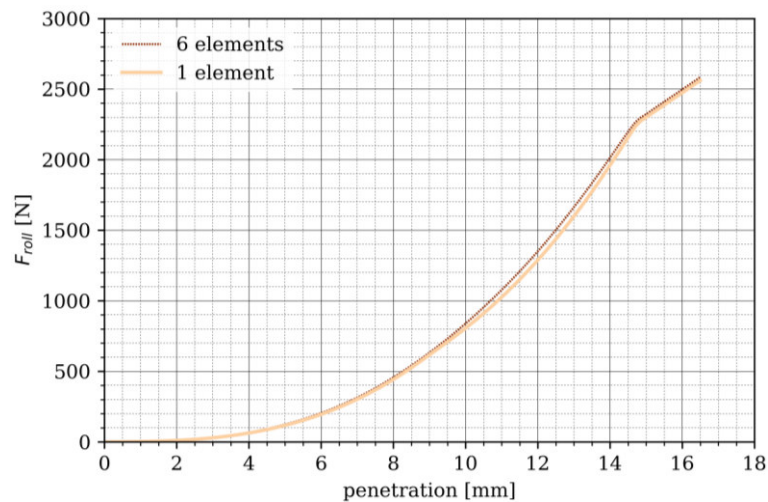


Figure 4.19 - Roll force during penetration for a mesh size of 0.167 mm .

As seen in Figure 4.20 the evolution of the maximum contact normal stress during the penetration differs when six elements through the thickness are used. This difference suggests a high influence of the bending representation in the contact normal stress. A better definition shows a smoother evolution of the maximum contact normal stress.

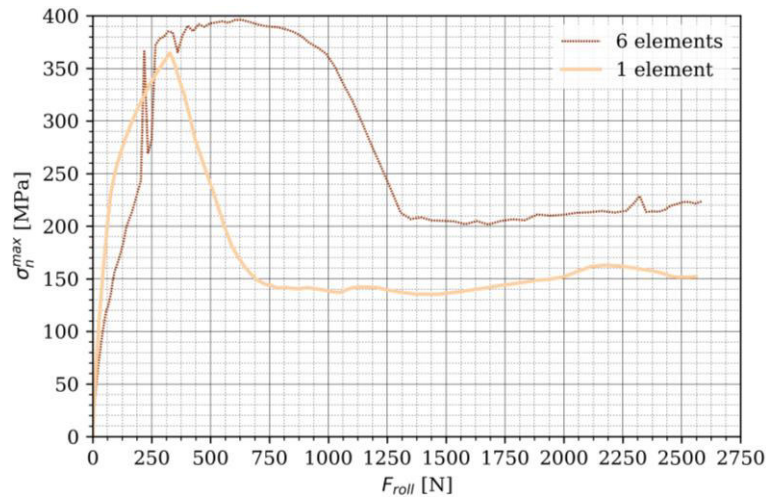


Figure 4.20 - Maximum contact normal stress during penetration for a mesh size of 0.167 mm and using different thickness discretisations.

For a roll force of 234 N and 360 N the evolution of the maximum contact normal stress shows a discontinuity. In these increments, nodes come in contact prematurely and separate again in the next increment.

Figure 4.21 illustrates the contact normal stress for the 0.167 mm mesh size when the thickness was discretised into one and six elements. These values correspond to the increment when the termination roll force was reached or, in other word, the penetration last increment. Discretising into six elements, the contact normal stress maximum value was reached near the corner of the contact area, and not in the centre line, archiving a four-point contact. This agrees with what was observed for a mesh size equal or higher than 0.333 mm (Figure 4.11).

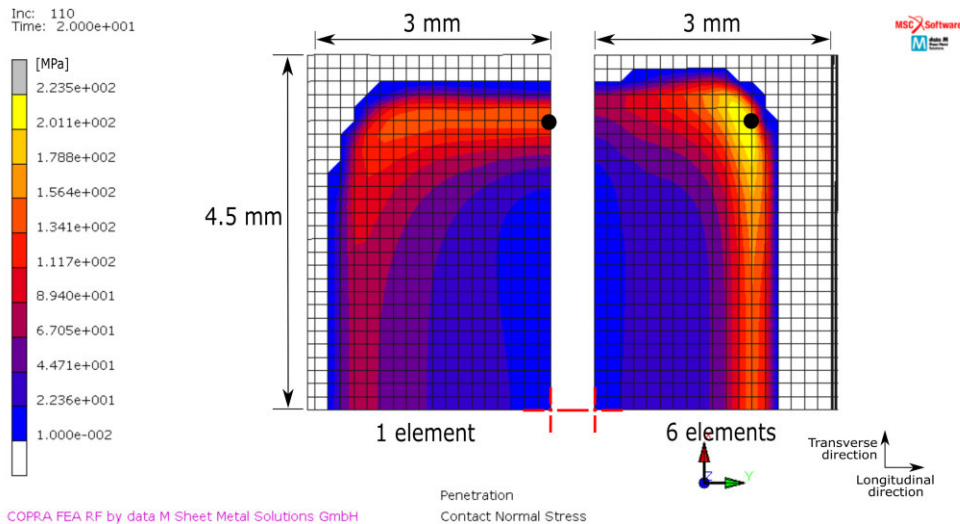


Figure 4.21 - Contact normal stress at the last increment of the penetration, discretising the thickness into one and six elements and using a 0.167 mm mesh size; the maximum value location is pointed out in black.

Table 4.1 compares the contact normal stress maximum value, reached in the last increment of the penetration, using a 0.167 mm mesh size and with a thickness discretisation of both six and one elements. The contact normal stress maximum value increased 71.4 MPa when the thickness was discretised with six elements, when comparing to only one element. This value corresponds to an increasing of 47 %.

Table 4.1 - Maximum contact normal stress calculated in the last increment of the penetration using a 0.167 mm mesh size.

Thick ness discretisation	σ_n^{max} [MPa]	Number of nodes
6 elements	223.5	4
1 element	152.1	2

The model with a thickness discretisation of six elements showed a four-point contact. In this case, the elements in the possible contact zone are cubic. Thus, with an improved element aspect ratio, the location of the maximum contact normal stress for a mesh size of 0.167 mm got close to what had been observed for a mesh size equal or higher than 0.333 mm.

In section 4.1.1 was observed that a discretisation of the possible contact zone with a mesh size of 0.333 mm, 0.250 mm or 0.167 mm has very similar results. The only difference is the two-point contact for a mesh size of 0.250 mm and 0.167 mm, in contrast with a four-point contact for a mesh size of 0.333 mm. Since it was proven that the two-point contact is due to a bad element aspect ratio, it is worth compare again the mesh size of 0.167 mm with the mesh size of 0.333 mm, but now using six elements over the thickness. As seen also in section 4.1.1, the mesh size of 0.167 mm has an extremely high computation cost when compared to the mesh size of 0.333 mm.

The longitudinal bending representation for a 0.167 mm mesh size and a 0.333 mm is represented in Figure 4.22 and Figure 4.23. An analysis of the graphics shows no differences in the longitudinal bending geometries.

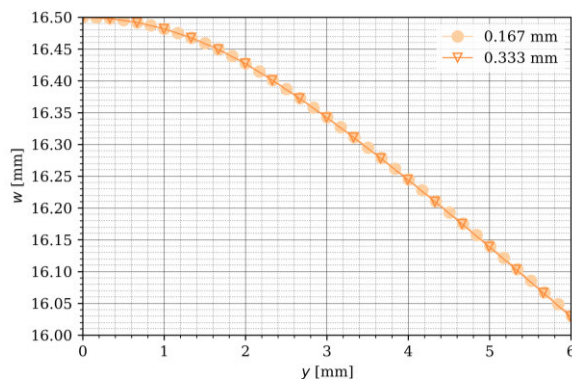


Figure 4.22 - Longitudinal bending geometry for the contact zone, at the last increment of the penetration and using six elements through the thickness.

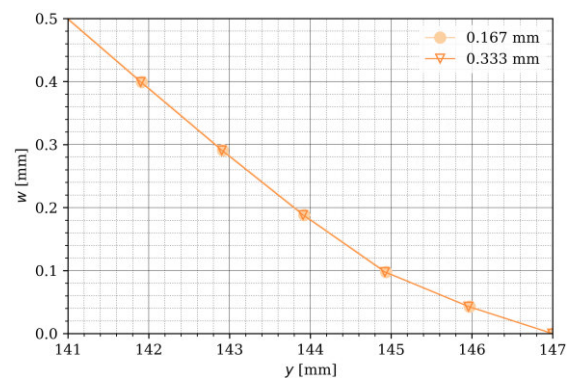


Figure 4.23 - Longitudinal bending geometry for the fixed zone, at the last increment of the penetration and using six elements through the thickness.

The transverse bending (Figure 4.24) was also coincident for both 0.167 mm mesh size and a 0.333 mm mesh sizes.

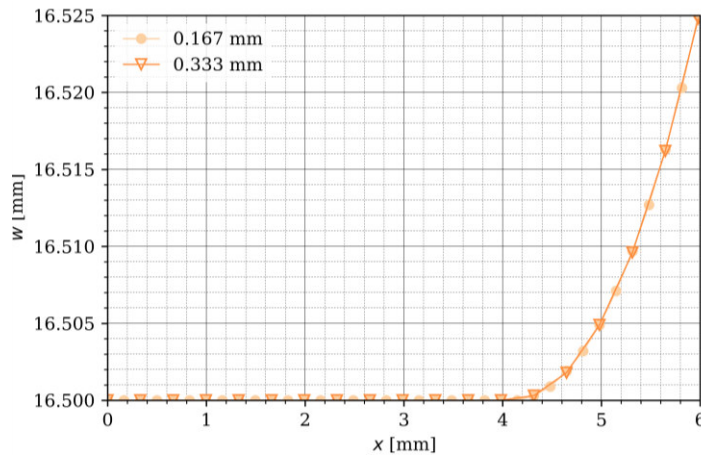


Figure 4.24 - Transverse bending geometry for the contact zone, using a thickness discretisation into six elements; calculated at the penetration last increment.

An analysis of the roll force during penetration (Figure 4.25) shows that there is practically no difference between the result obtained with a 0.167 mm mesh size and a 0.333 mm mesh size.

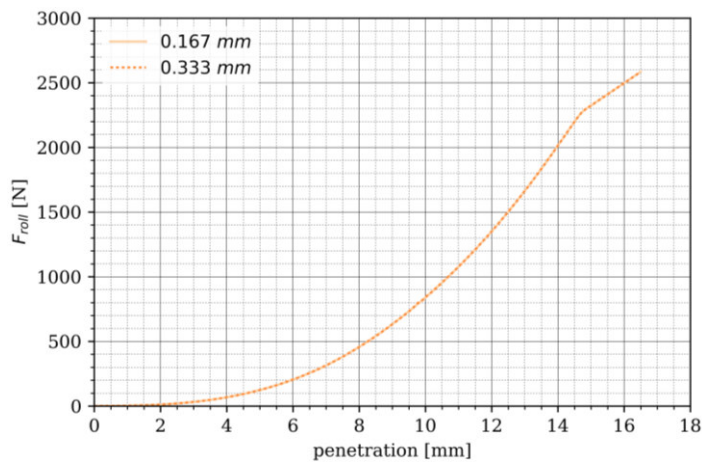


Figure 4.25 - Roll force during penetration using a thickness discretisation into six elements.

The maximum contact normal stress evolution during penetration is represented in Figure 4.26. The 0.333 mm mesh size shows very different values for a roll force lower than 900 N.

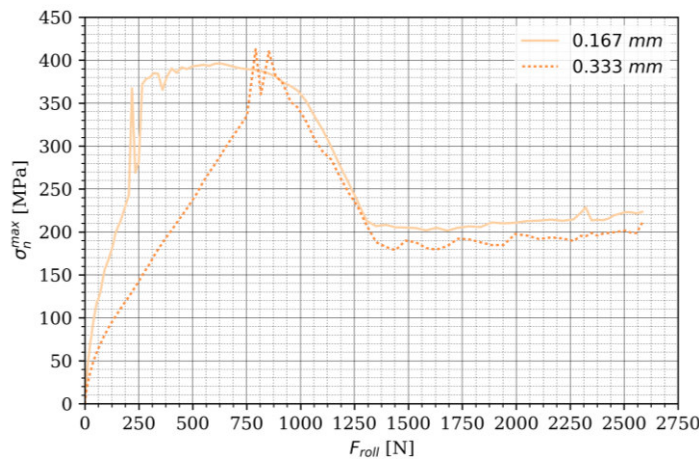


Figure 4.26 - Maximum contact normal stress during penetration using a thickness discretisation of six elements.

In order to understand the differences observed in Figure 4.26, an increment at the increasing stress phase was selected. In addition, the increments correspondent to the oscillation were also selected to study in more detail. These points are the increments 55 and increments 64 to 68 and are represented in Figure 4.27. At increment 55 the roll has moved 8.25 mm , at increment 64 has moves 9.6 mm and at increment 68 has moves 10.2 mm .

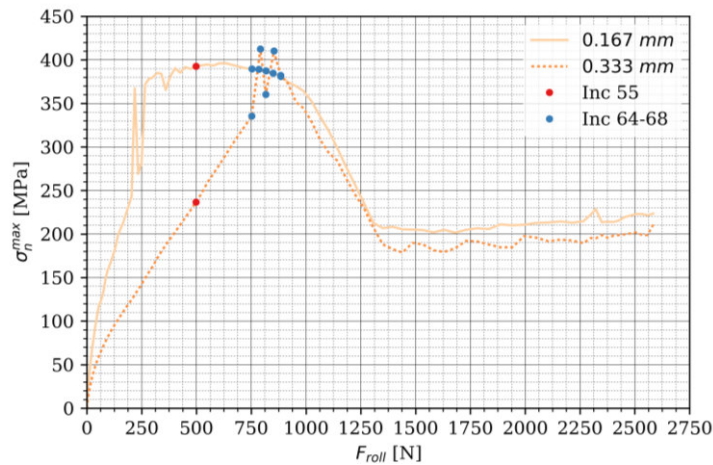


Figure 4.27 - Increments studied for the maximum contact normal stress during penetration using a thickness discretisation into six elements.

The roll force and maximum contact normal stress, for each mesh size, at increment 55 are summarised in Table 4.2.

Table 4.2 - Roll force and maximum contact normal stress at increment 55.

Mesh size [mm]	F_{roll} [N]	σ_n^{max} [MPa]
0.167	497.8	392.7
0.333	497.4	236.7

Figure 4.28 illustrates the contact normal stress distribution for 0.167 mm and 0.333 mm mesh size at increment 55.

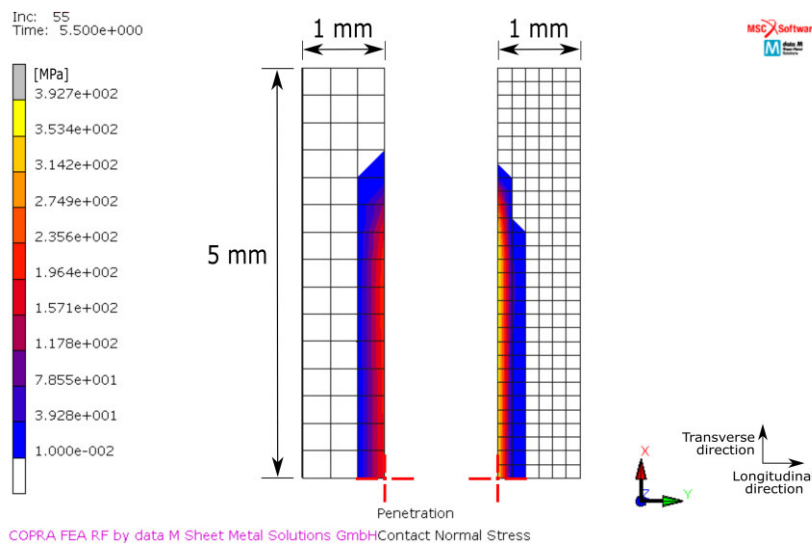


Figure 4.28 - Contact normal stress at increment 55 for 0.333 mm and 0.167 mm mesh size, respectively.

Observing Figure 4.28 is possible to conclude that until increment 55 there was, approximately, only one line of nodes in contact. In fact, the contact area has a width of approximately 0.333 mm , making it difficult to have a good representation of the real contact normal stress distribution in the longitudinal direction. With a 0.333 mm mesh size there was only one element in contact in the longitudinal direction, in contrast with the 0.167 mm mesh size where two elements are in contact. However, after an approximate 900 N roll force the values are in a good agreement. In fact, the contact normal stress at the last increment of the penetration are hardly distinguishable.

Regarding the discontinuity observed (Figure 4.27), Table 4.3 states the roll force and maximum contact normal stress for the increment when this is observed.

Table 4.3 - Roll force and maximum contact normal stress of the increments around the maximum contact normal stress discontinuity for 0.333 mm .

Increment	$F_{roll}\text{ [N]}$	$\sigma_n^{max}\text{ [MPa]}$
64	751.9	335.5
65	791.7	412.6
66	816.4	360.5
67	853.1	410.2
68	883.7	382.3

Figure 4.29 shows the nodes in contact for the increments specified in Figure 4.27. This data shows that this discontinuity is caused by nodes coming in contact prematurely and separating at the following increments.

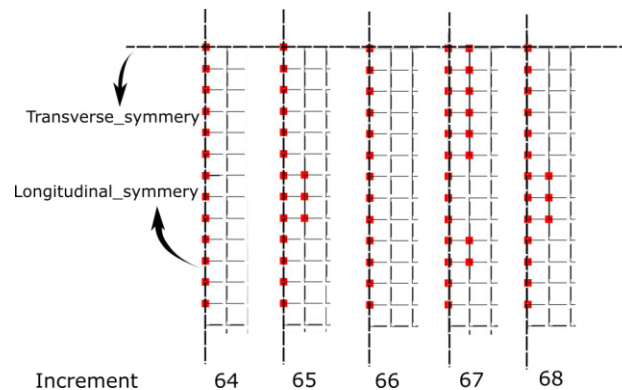


Figure 4.29 - Contacting nodes for several increments, around the maximum contact normal stress discontinuity, for a mesh size of 0.333 mm .

The differences observed for the maximum contact normal stress evolution before the peak is reached are related with the mesh size, however, after the peak the curves converge. The oscillations observed for the mesh size of 0.333 mm are due to nodes entering in contact prematurely. However, after the nodes separate again, the curve converges to the same value of the mesh size of 0.167 mm .

The contact normal stress distribution at the last increment for both mesh sizes is represented in Figure 4.30.

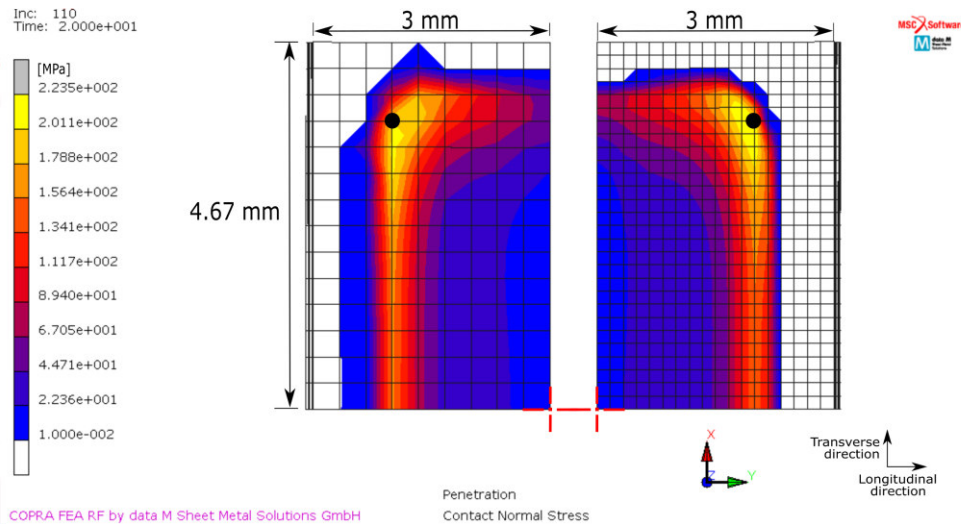


Figure 4.30 - Comparison of the contact normal stress for 0.333 mm and 0.167 mm mesh size using six a thickness discretisation into six elements; calculate at the penetration last increment.

Table 4.4 summarises the contact normal stress maximum value, whose locations are illustrated in Figure 4.30. The contact normal stress distributions of both mesh sizes are barely indistinguishable. The contact normal stress maximum value for each mesh size are also very close. The 0.333 mm mesh size was a 12.5 MPa lower maximum contact normal stress, which corresponds to only 0.3% of the maximum contact normal stress for a 0.167 mm mesh size.

Table 4.4 - Maximum contact normal stress at the last increment of the penetration for a mesh with thickness discretisation of six elements.

Mesh size [mm]	σ_n^{max} [MPa]
0.167	223.5
0.333	211.0

At this point is possible to sustain that the contact normal stress converges to a four-point contact. When the model with a 0.167 mm mesh size had the thickness discretised into six elements, the results showed a four-point contact. This suggests that the element aspect ratio influences the results. The longitudinal bending and transverse bending with a thickness discretisation of six elements have a different representation when compared with the discretisation with only one element. This suggests that the bending representation influences the contact normal stress distribution. Furthermore, a comparison of this representation with a model having also a thickness discretisation of six elements but a 0.333 mm mesh size showed a good correspondence. The contact normal stress distribution, longitudinal and transverse bending geometry, as well as the evolution of the roll force are hardly undistinguishable. Thus, in order to have a good compromise between contact representation and computation cost, the 0.333 mm mesh size was adopted.

The study proceeded with an attempt to reduce the computational cost by optimising the thickness discretisation, without compromising the results' accuracy.

4.1.3 OPTIMISATION OF THE THICKNESS DISCRETISATION

This section outlines the optimisation of the thickness discretisation. This optimisation is a continuity of the study presented in section 4.1.2 where it was proven that the thickness discretisation has a high influence on the bending representation and, consequently, on the contact representation.

Similarly to the previous sections, the study starts by analysing the bending geometry and the evolution of the roll force during the penetration phase. The maximum contact normal stress evolution during the penetration phase was, then, analysed, followed by a comparison of the contact normal stress distribution in each simulation.

Considering the results of section 4.1.2, was used a model with a mesh size of 0.333 mm for the possible contact zone. The parameter changed was the number of elements over the thickness. Six different models were created, with six, five, four, three and two elements over the thickness. Again, in this study only the penetration phase was simulated, having been modelled only one quarter of the sheet.

The longitudinal bending geometry is represented in Figure 4.31 and Figure 4.32. In the possible contact zone (Figure 4.31), no differences are observed. However, in the “fixed” zone (Figure 4.32) is observed a slight difference in the geometry for a discretisation with two elements.

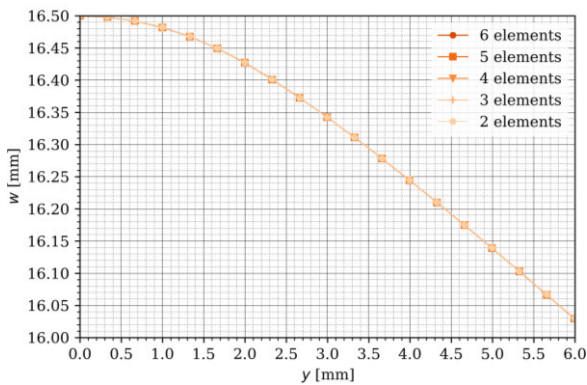


Figure 4.31 - Longitudinal bending geometry for the possible contact zone, at last increment of the penetration and using different thickness discretisation.

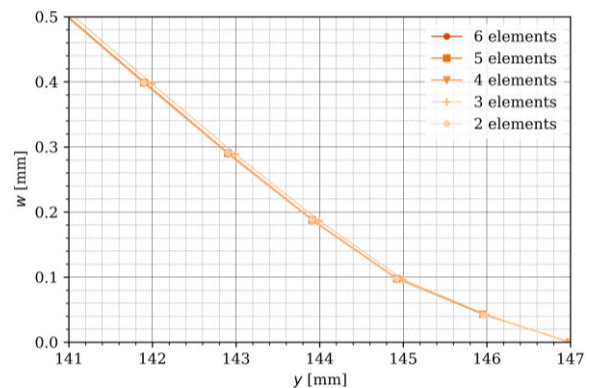


Figure 4.32 - Longitudinal bending geometry in the “fixed” zone, at last increment of the penetration and using different thickness discretisation.

In contrast, the transverse bending geometry is influenced by the thickness discretisation (Figure 4.33). Between the four, five and six elements discretisation there is no differences observed. However, the points correspondent to the thickness discretisation with two elements show higher displacement w for the same position x when compared with the other representations.

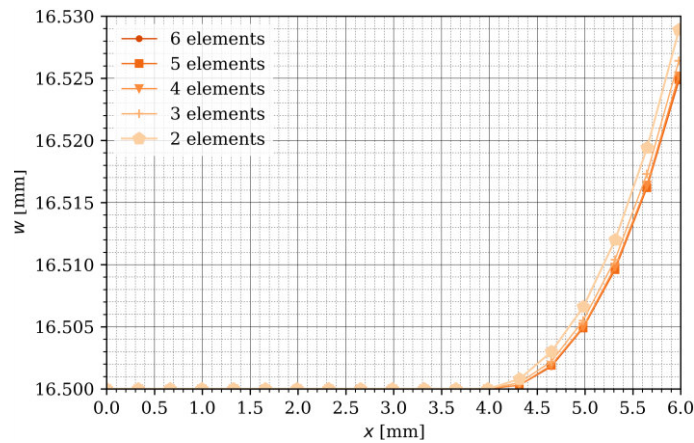


Figure 4.33 - Transverse bending geometry, at the last increment of the penetration, using different thickness discretisation and a mesh size of 0.333 mm .

An analysis of the roll force evolution during penetration (Figure 4.34), shows that the thickness discretisation does not influence the roll force needed to bend the sheet.

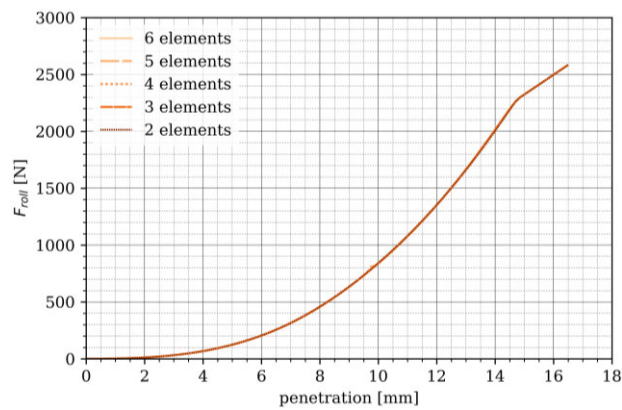


Figure 4.34 - Roll force during penetration for a mesh size of 0.33 mm with different thickness discretisations.

The maximum contact normal stress evolution during the penetration is represented in Figure 4.35. The curves show the same behaviour. However, the maximum contact normal stress for the two elements discretisations is lower than the other discretisations after the peak is reached.

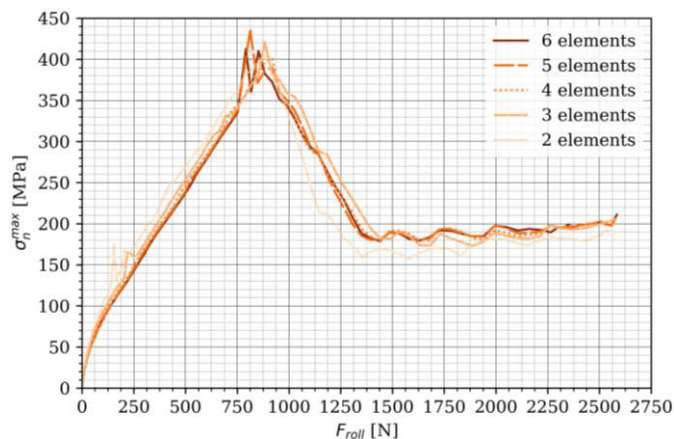


Figure 4.35 - Maximum contact normal stress during penetration using a different thickness discretisations.

Figure 4.36 represents the contact normal pressure distribution for the different thickness discretisations.

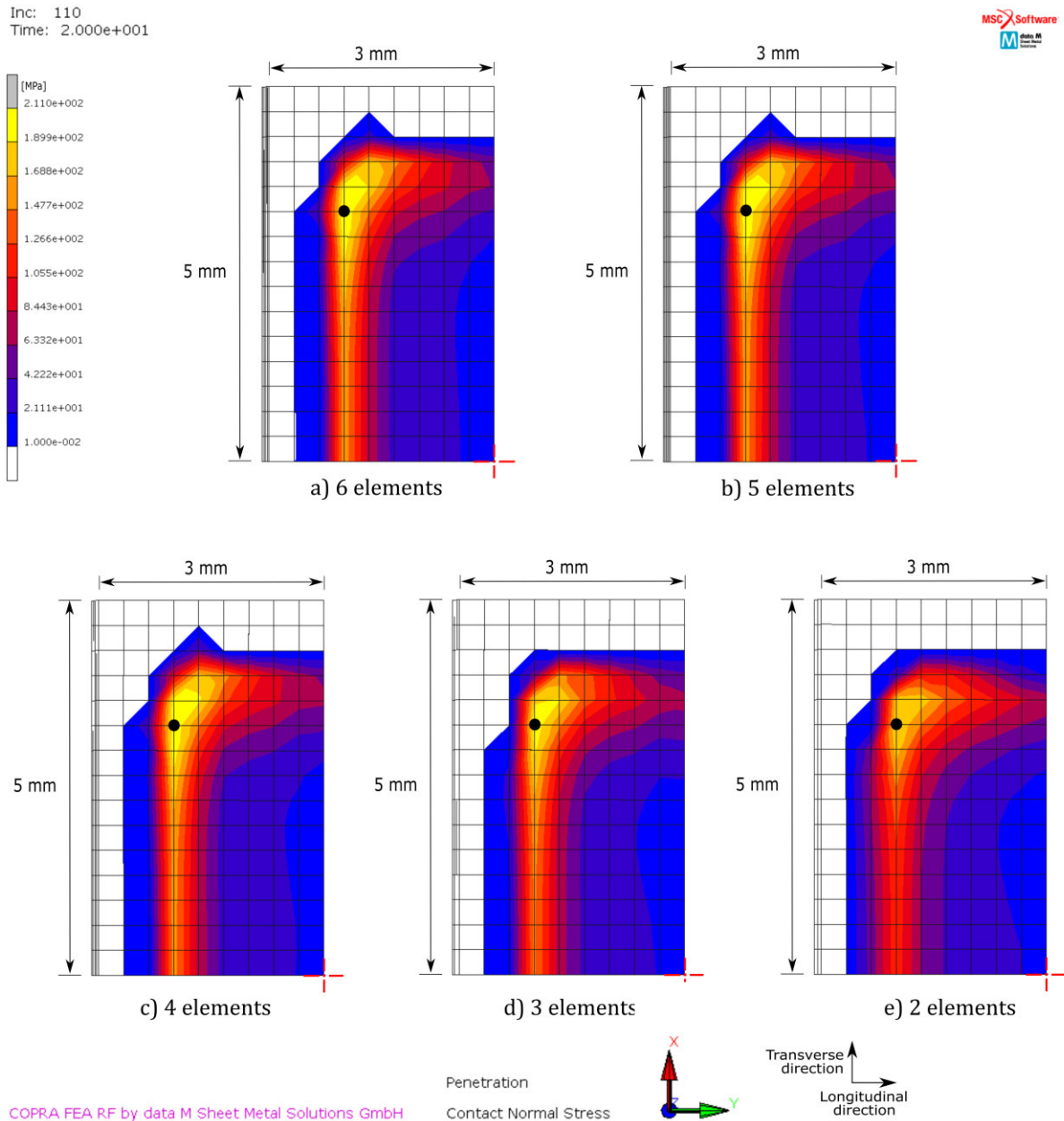


Figure 4.36 - Contact normal stress at the last increment of the penetration for different thickness discretisation and using a mesh size of 0.333 mm.

Observing Figure 4.36, is visible that the contact normal stress distribution is similar for the different thickness discretisations. In order to better analyse the contact normal stress distribution, a axis with the origin coincident with the maximum normal contact stress was used (Figure 4.37).

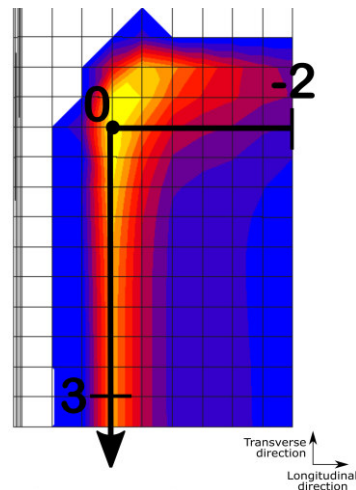


Figure 4.37 - Axis used to represent the contact normal stress distribution.

Figure 4.38 shows a representation of the contact normal stress along the axis defined in Figure 4.37. All curves show the same behaviour, however, the discretisation with two elements shows a clear lower contact normal stress distribution along the transverse direction.

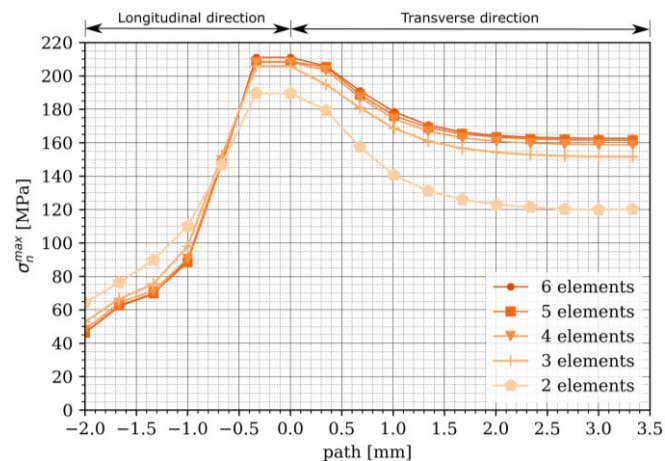


Figure 4.38 - Contact normal stress variation for different thickness discretisations.

Table 4.5 states the maximum contact normal stress of the points highlighted in Figure 4.36. The maximum contact normal stress variation with the thickness discretisation is negligible, except for the two elements. The difference between two and six elements is 10 % in contrast with only 2 % difference between three and six elements.

Table 4.5 - Maximum contact normal stress for the different number of elements along the thickness.

Thickness discretisation	σ_n^{max} [MPa]
6 elements	211.0
5 elements	208.5
4 elements	208.1
3 elements	205.9
2 elements	189.6

The computational cost is represented in Figure 4.39.

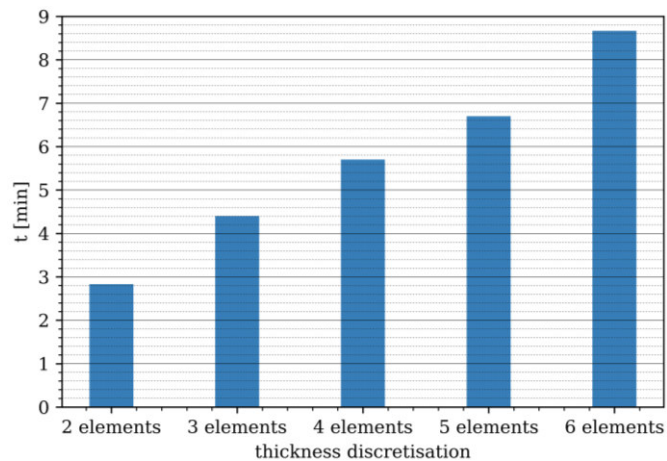


Figure 4.39 - Simulation computational time for the different thickness discretisation.

An analysis of the computation time shows that the computational cost decreases with less number of elements are used along the thickness. The analysis of the bending geometry, shows that this representation is influenced by the thickness discretisation, however, a similar representation is obtained when three or more elements are used. Similarly, the maximum contact normal stress evolution shows the same behaviour for different number of elements along the thickness, however, after the peak only the discretisation with three or more elements converge to the same value. Therefore, a thickness discretisation with three elements is the optimal solution.

4.1.4 VERIFICATION OF THE MESH TRANSITIONS

Before defining the optimised mesh discretisations, it is important to study the transitions influence on the results. In section 3.2.3 a possible contact zone and a “fixed” zone were defined (Figure 3.14) when modelling the sheet discretisation. These zones have a finer discretisation which results in the existence of transitions between the different discretisations. In this case, the sheet has a non-homogenous discretisation as represented in Figure 4.40.

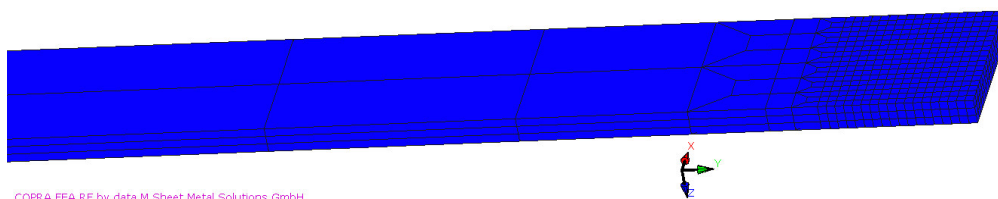


Figure 4.40 - Sheet discretisation with a transition mesh.

This section outlines the verification of the transitions influence on the results. The bending geometry and the evolution of the roll force during the penetration phase were analysed at first. Then, the maximum contact normal stress evolution during the penetration phase was analysed, followed by a comparison of the contact normal stress distribution in each simulation.

Two models were created. The first has the discretised with transitions, as used before (Figure 4.40). The possible contact zone has a mesh size of 0.333 mm and the thickness is discretised into three elements. The second model has a homogenous discretisation (Figure 4.41).

This homogenous mesh has cubic elements with a dimension of 0.333 mm . In both models only the penetration phase was simulated and only one quarter of the sheet was modelled.

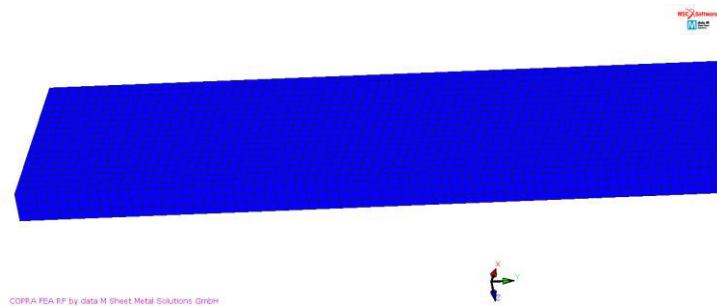


Figure 4.41 - Sheet discretisation with a homogenous fine mesh.

Figure 4.42 shows a representation of the longitudinal bending geometry in the contact zone and for the last increment of the penetration. This result shows consistency between the mesh with transition and the homogenous mesh.

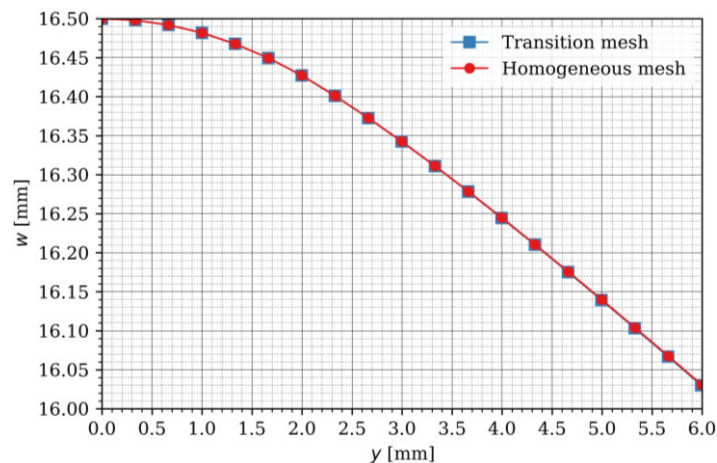


Figure 4.42 - Longitudinal bending geometry for the possible contact zone at the last increment of the penetration.

Figure 4.43 shows a representation of the longitudinal bending in the “fixed” zone at the last increment of the penetration. Unlike the possible contact zone, in the “fixed” zone the results are not consistent. In contrast with the possible contact zone discretisation, the “fixed” zone has elements with different sizes in each model. The homogenous mesh has cubic 0.333 mm elements in the “fixed” zone and the transitions mesh has elements with 1 mm dimension in the longitudinal and transverse direction and 0.333 mm in the thickness direction. Thus, the transition mesh does not have elements with a perfect element ratio and has less number of elements in the longitudinal and transverse direction. In the position $x = 141\text{ mm}$, the transition mesh has a displacement w only 4 % lower than the registered for the homogeneous mesh, therefore, the differences between the two models can be neglected.

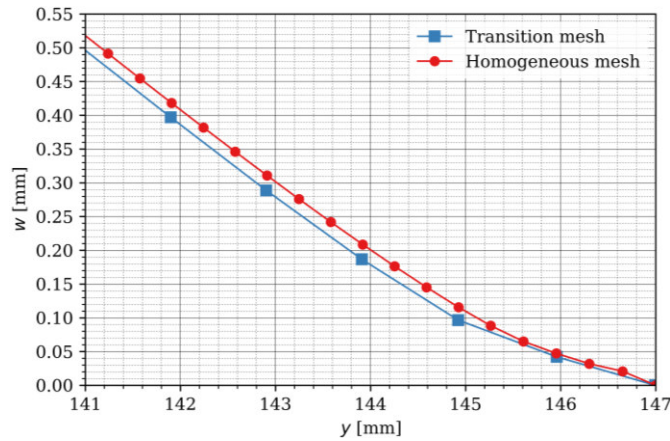


Figure 4.43 - Longitudinal bending geometry for the “fixed” zone at the last increment of the penetration.

The transverse bending geometry at the last increment of the penetration is represented in Figure 4.44. This representation shows that the discretisation with transitions used along the sheet length influences the representation of the transverse bending. However, in the extreme point ($x = 6\text{ mm}$) the transition mesh has only a displacement w 6% higher than the homogenous mesh.

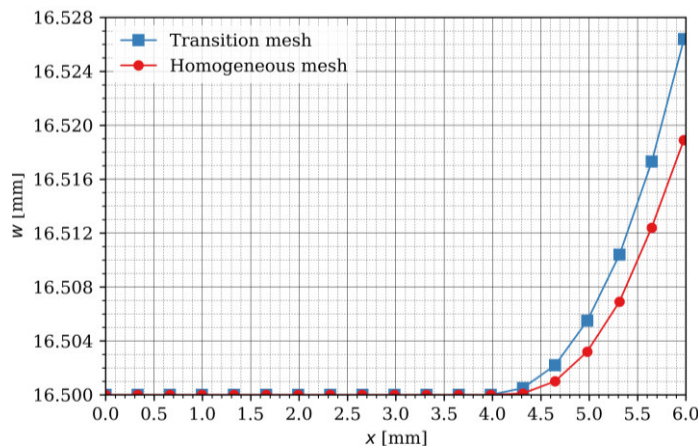


Figure 4.44 - Transverse bending geometry at last increment of the penetration.

Figure 4.45 shows the evolution of the roll force during penetration. The results of both discretisations are coincident.

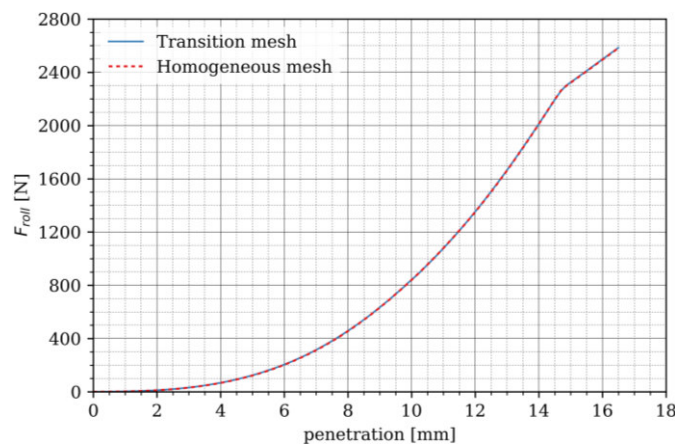


Figure 4.45 - Roll force during penetration for a mesh with transitions and a homogeneous fine mesh.

Figure 4.46 compares the maximum contact normal stress during penetration for both discretisations. It is observed a higher value with a homogenous mesh until a roll force of 1400 N. From this point, the curves show a tendency to converge to the same value.

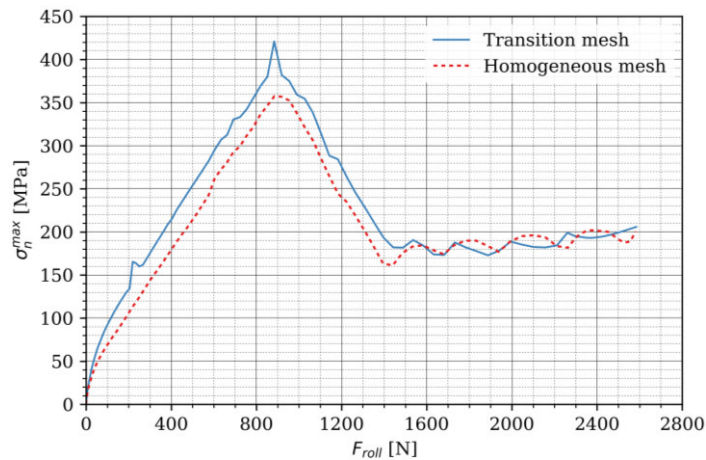


Figure 4.46 - Comparison of the maximum contact normal stress during penetration for a homogeneous mesh and a mesh with transitions.

The contact normal stress distribution at the last increment of the penetration is represented in Figure 4.47. Both models exhibit a similar distribution, having the maximum contact normal stress located in the same node.

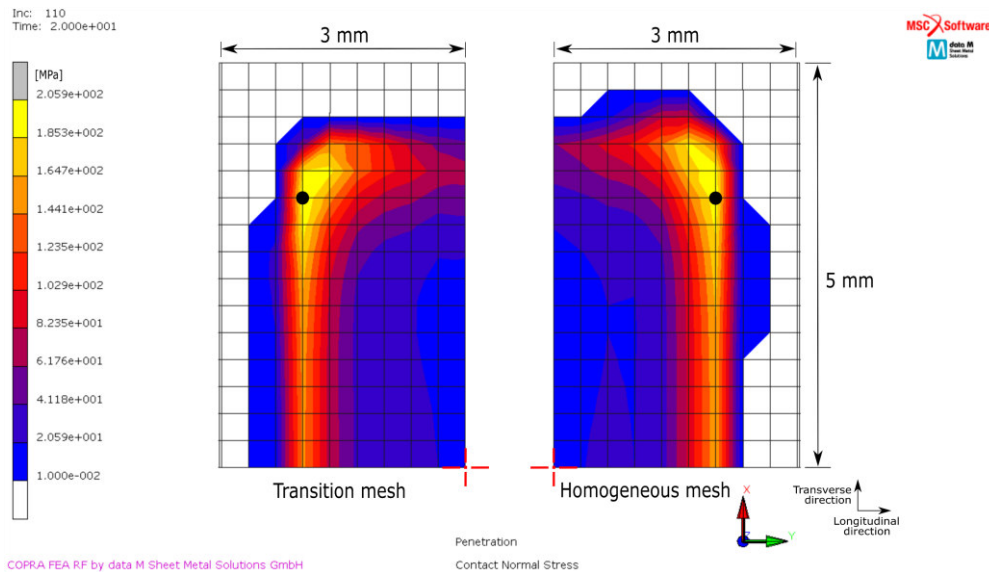


Figure 4.47 - Contact normal stress in the last increment of the penetration, with the maximum value location pointed out.

The values of the maximum contact normal stress are stated in Table 4.6. The difference between the maximum contact normal stress in the mesh with transitions and the homogeneous mesh is only 5.6 MPa.

Table 4.6 - Maximum contact normal stress at the last increment of the penetration for a mesh with transitions and a homogeneous fine mesh.

Discretisation	σ_n^{max} [MPa]
With transitions	205.9
Homogeneous	200.6

In order to confirm the similarities in the contact normal stress distribution, Figure 4.48 shows a representation of the contact normal stress along the same axis used in the previous section (Figure 4.37).

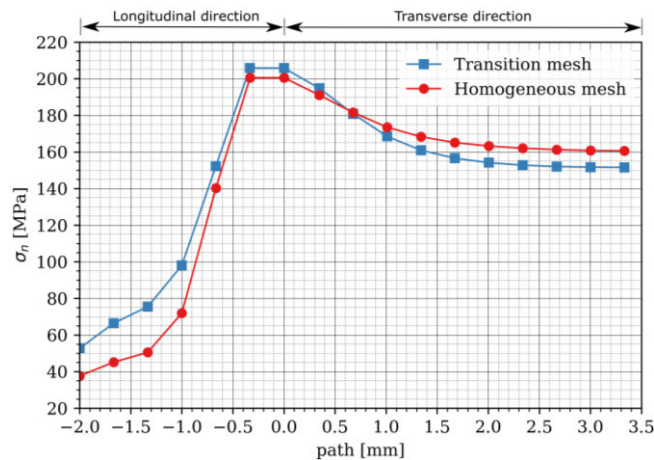


Figure 4.48 - Contact normal stress along a path with origin in the maximum value node.

An observation of Figure 4.48 confirms that the contact normal stress shows similar distributions in both cases, since the curves exhibit the same behaviour.

The homogeneous mesh took 81 *min* to simulate, in contrast with the mesh with transitions that only took 4 *min*. In other words, the use of a mesh with transitions reduces the computational cost in 95 %. Considering that the longitudinal and transverse bending shows similar representations, as well as the evolution of the roll force, the maximum contact normal stress evolution and contact normal stress distribution, the mesh with transitions is validated.

4.1.5 STUDY OF THE NODES LOCATION WITH THE ROLL AXIS

An analysis of the model without the longitudinal symmetry (half of the sheet modelled, instead of one quarter) showed instabilities in the torque acting on the roll during the simulation. Thus, this instability was studied by changing the position of the nodes with the roll axis.

First, the roll torque was analysed. Then, the displacement v (longitudinal direction) of the centre line nodes was also investigated. This was performed for different positions of the nodes with the roll axis. After eliminated the torque instability, the contact normal stress distribution was also analysed to confirm if this change had effects on the contact representation.

The roll torque during the penetration has a value different than zero, and oscillates (Figure 4.49). Even though it tends to converge to zero close to the end of the penetration, the reason behind this instability is important to investigate.

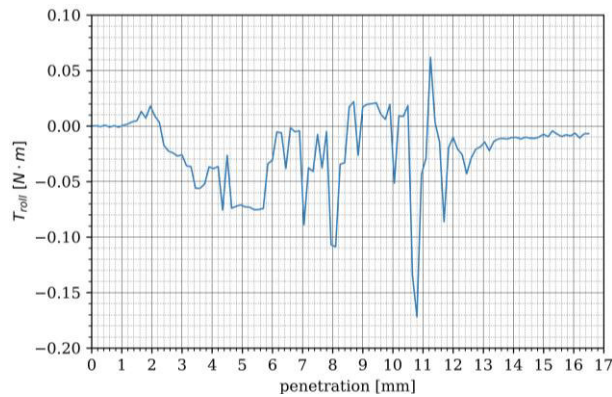


Figure 4.49 - Roll torque during penetration when the roll axis is in line with a line of nodes.

Similarly, the nodes of the inner surface centre line (same path defined in Figure 4.3, page 48) have displacements in the longitudinal direction different than zero. Figure 4.50 represents these displacements in the longitudinal direction (v) along the transverse direction (x) at the last increment of the penetration. The movement of the nodes in the centre line are causing a sliding between the surfaces that causes friction forces. These friction forces acting in the contact area create the torque instability (Figure 4.49).

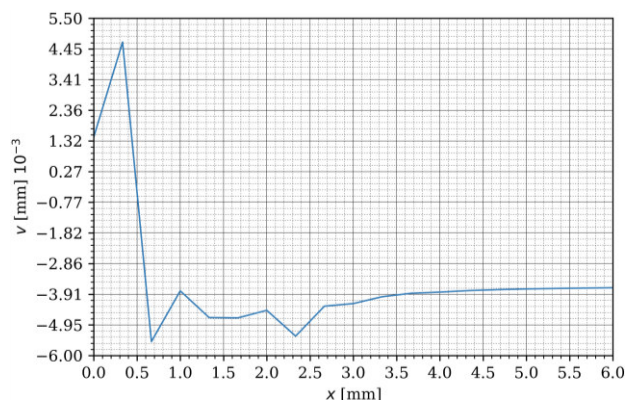


Figure 4.50 - Displacement in the longitudinal direction along the sheet centre line on the inner surface at the last increment of the penetration.

In order to eliminate this irregularity, the mesh was refined in the centre ensuring that the roll axis would be in line with the middle plane of elements, and not in line with a line of nodes. Within all possible combinations, the four centre nodes were changed by five nodes (Figure 4.51).

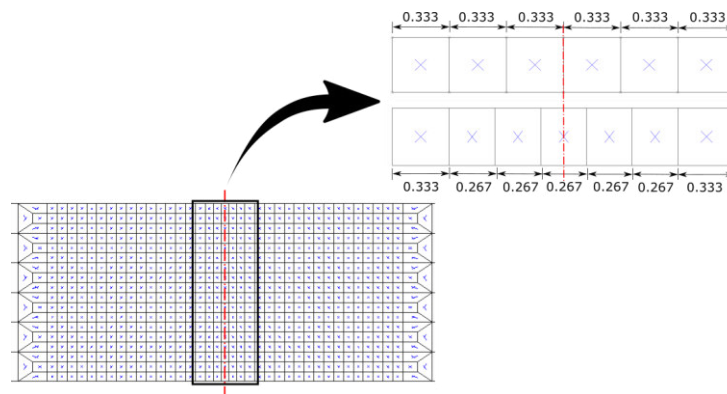


Figure 4.51 - Refinement of the mesh in the sheet centre.

This refinement eliminated the roll torque instability during the penetration. As seen in Figure 4.52, the torque is zero after the refinement.

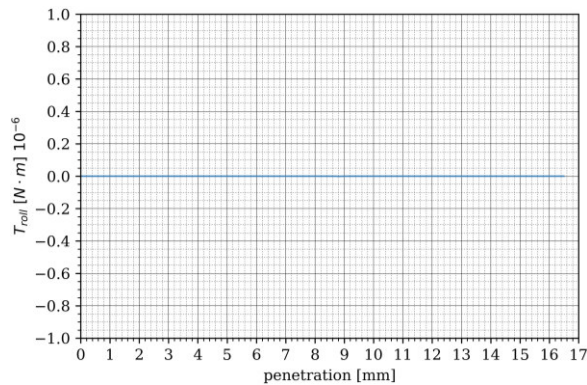


Figure 4.52 - Roll torque during penetration when the roll axis is in line with the elements middle plane.

The contact normal stress distribution for both cases is represented in Figure 4.53. An analysis of this figure shows that this change in the central elements did not have any effect on the contact normal stress.

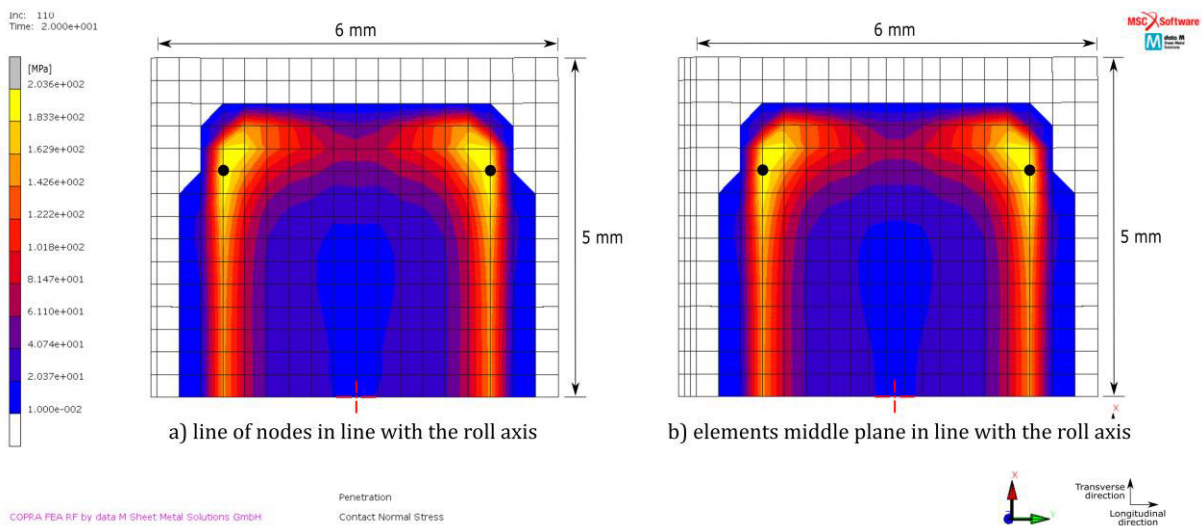


Figure 4.53 - Contact normal stress at the last increment of the penetration for different elements location with the roll axis.

The location of the nodes with the roll axis have an influence on the simulation stability. Specifically, when a line of nodes is aligned with the roll axis, the nodes are not stable and displacements in the longitudinal direction are visible in the simulation. This movements create a roll on the torque. Thus, in order to improve the torque calculated, should be avoid having nodes in line with the roll axis.

The study of the results sensitivity with the mesh discretisation proved that the contact represented in the simulations is highly influenced by the mesh discretisation. An analysis of the simulation behaviour with different discretisations allowed to improve the discretisation in the longitudinal and transverse direction, as well as the thickness discretisation and the location of the elements with the roll axis. The optimised discretisation is summarised in section 4.4.1.

4.2 CONTACT SEARCH DEFINITION

This section presents the study of the contact search influence on the contact representation. This study continues the optimisation of the FE model, using the optimised mesh discretisation resultant from the study outlined in section 4.1.

Contact search plays a fundamental role on the contact representation. It defines which nodes are in contact and when they enter into contact. Thus, the simulation stability is highly influenced by the contact search definition. In COPRA® FEA RF the contact search algorithm is based on a boundary tolerance (chapter 3.2.7 Contact). This algorithm allows the user to define the contact distance tolerance (Figure 3.23) and a bias factor (Figure 3.24). The contact distance tolerance defines the area at which a node is in contact with a segment. The bias factor defines the ratio between the distance in the inside and outside of the surface.

In this section, the contact distance tolerance and the bias factor were studied. In the contact search investigation, the model introduced in chapter 3.2 was used, except for the metal sheet discretisation. The discretisations was based on the results of the mesh sensitivity study outlined in section 4.1. Thus, the possible contact zone was discretised using elements with a 0.333 mm square top face, the thickness was discretised into three elements and the sheet centre elements were refined (Figure 4.51)

4.2.1 DISTANCE TOLERANCE

This section focused on the study of the distance tolerance parameter and aims to understand this parameter influence on the contact representation.

Given this parameter direct influence on the contact detection, firstly, was performed an analysis of the number of nodes in contact. Then, the stability of the roll rotation was confirmed, followed by an analysed of the forces acting on the roll (roll torque and the roll force). Lastly, the maximum contact normal stress evolution and the contact normal stress distribution were analysed.

The different distance tolerances in this study are: 0.01, 0.02, 0.03, 0.04 and 0.05. In all cases, the bias factor was maintained as 0.95.

As the roll is pushed against the metal sheet, a progressive bending is induced, and the contact area is continuously changing. Thus, the nodes are continuously entering in contact with the roll surface. Figure 4.54 represents the number of nodes in contact during the simulation for the different used distance tolerances. Until increment 110 the roll penetrates the metal sheet and after that initiates the rotation load case. Within this load case, the roll is maintained stopped until increment 118 and then rotates with a constant angular velocity until the end of the rotation load case -increment 639.

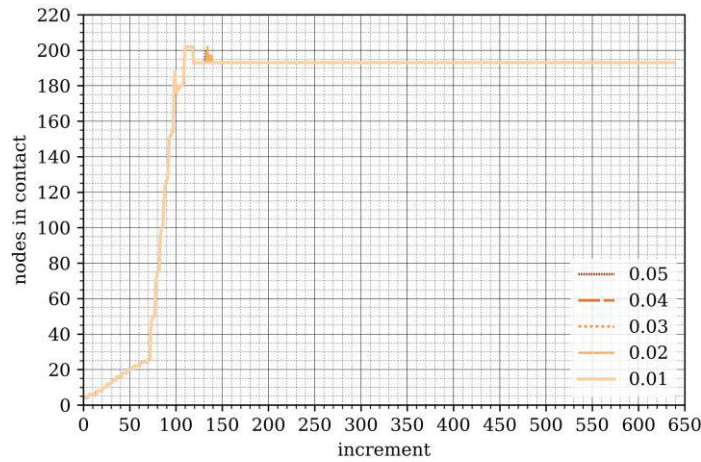


Figure 4.54 - Number of nodes in contact during the simulation for different contact distance tolerances.

A representation of the nodes in contact during the penetration is shown in Figure 4.55. When the end of the penetration is approached, nodes entering in contact and separating in the following increments is visible. Once a node is inside the tolerance defined by the contact distance tolerance, a contact force is applied to the node and convergence is checked. Thus, in order to understand this difference in the number of nodes in contact, a study of the solution convergence and increments recycling should be performed. This would be studied for different separation settings. However, it is out of the current project. A model with nodes coming in contact and separating, for example a roll rolling along a metal strip, would be more suitable for this investigation.

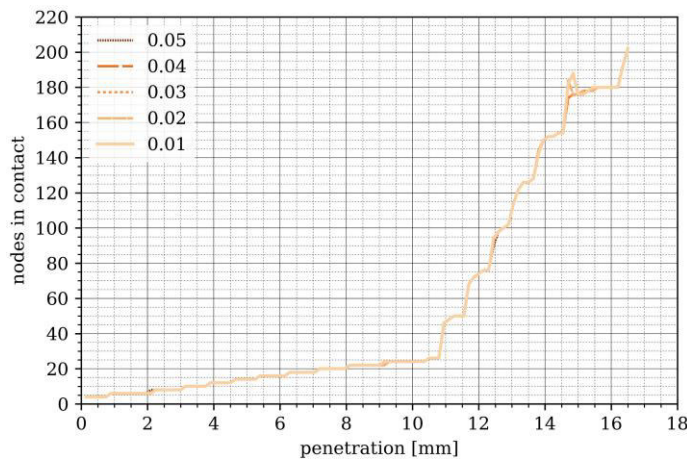


Figure 4.55 - Number of nodes in contact during the penetration for different contact distance tolerances.

Between a penetration of 14.5 mm and 15 mm, the number of nodes in contact is higher for a contact distance tolerance of 0.01 and 0.02. However, after a penetration of 15.5 mm the number of nodes in contact converges again to a constant value. During the rotation, the number of nodes in contact is maintained constant, without any node separating neither entering in contact. Until the roll rotates 0.5 rad, the number of nodes in contact is not constant. Thus, a deeper analysis for this part is needed.

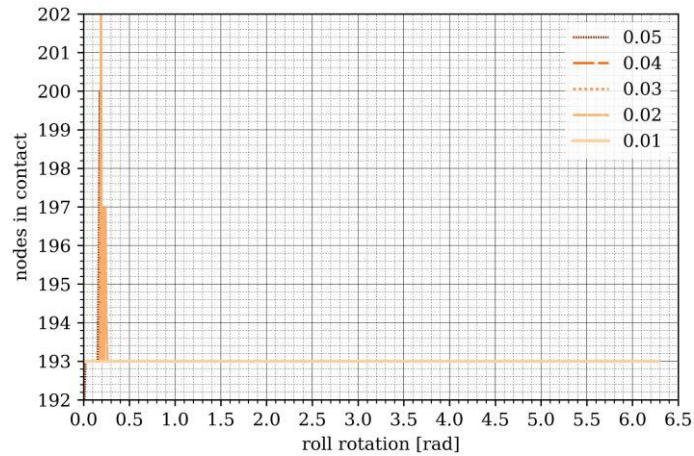


Figure 4.56 - Number of nodes in contact during the roll rotation.

In order to better analyse the rotation initial phase, Figure 4.56 represents the number of nodes in contact during the roll rotation between the position 0 rad and 0.5 rad . The contact distance tolerance of 0.02 and 0.05 show some instabilities, having nodes entering in contact and separating in the preceding increments. As stated before, further investigation of the separation criterion is needed to better understand this behaviour. Thus, the investigation precedes with the analysis of the simulation stability.

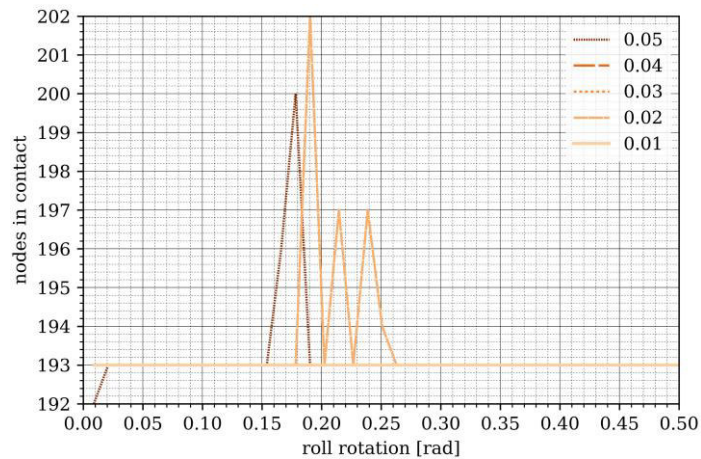


Figure 4.57 - Number of nodes in contact during the roll rotation instability.

A representation of the roll rotation during the simulation is shown in Figure 4.58. The rotation is constant during the penetration and increases with a constant slope when the roll starts rotating, being coincident for all contact distance tolerances studied. Thus, the roll rotation does not show any instability for the different distance tolerances tested.

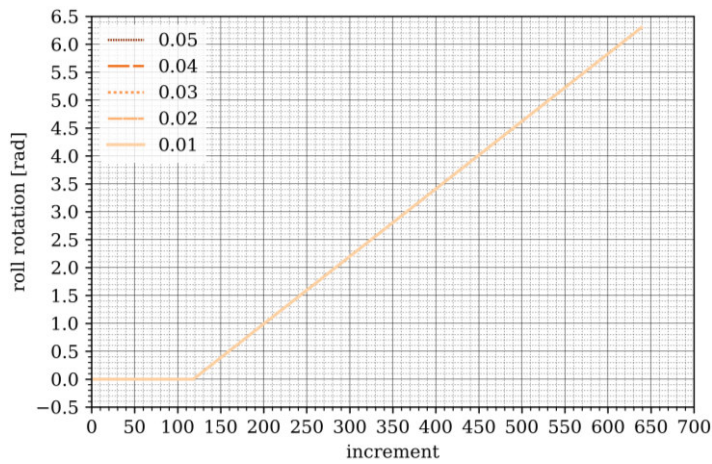


Figure 4.58 - Roll rotation during the simulation.

Figure 4.59 represents the roll torque during the simulation. Observing the roll torque during the penetration, was not found any imprecision. The roll torque is zero during the penetration and do not exhibit variation. However, when the roll starts rotating its torque oscillates until it converges to the dynamic torque. Therefore, it is needed to perform a deeper analysis of the torque during the rotation.

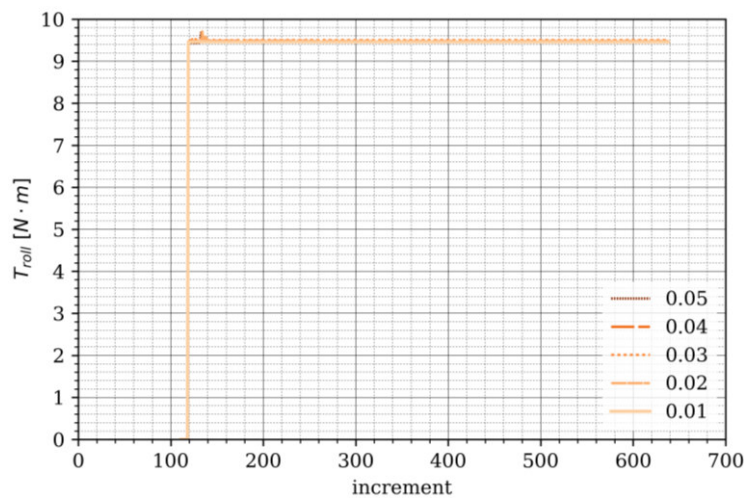


Figure 4.59 - Roll torque during the simulation.

The roll torque during the roll rotation is represented in Figure 4.60. For a defined contact distance tolerance of 0.02, 0.03, 0.04 and 0.05, the roll torque does not converge immediately to the dynamic torque. In addition, for the contact distance tolerance of 0.02 and 0.03 is visible an instability when the roll reached the position of, approximately, 1.6 rad.

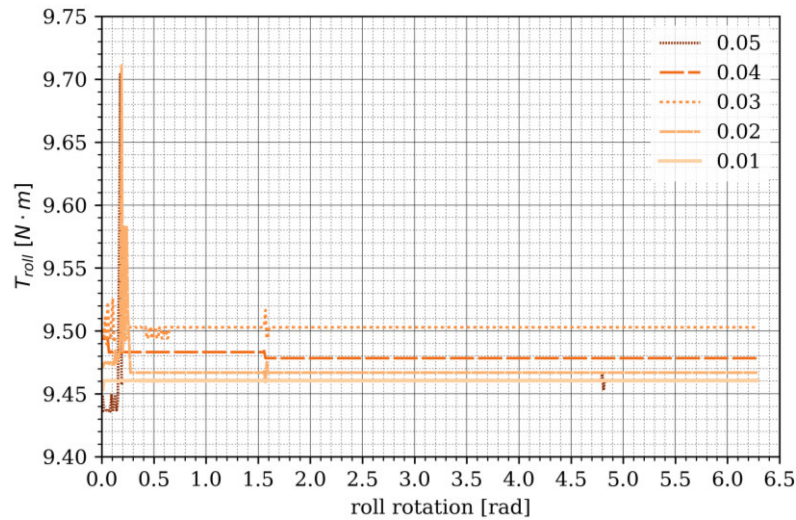


Figure 4.60 - Roll torque during the roll rotation.

Analysing in more detail the roll torque for a defined contact distance tolerance of 0.01 (Figure 4.61), it is observed that the simulation is searching for an equilibrium. Nevertheless, for a contact distance tolerance of 0.01 the torque appears to converge, having an oscillating amplitude lower than $0.001 \text{ N} \cdot \text{m}$.

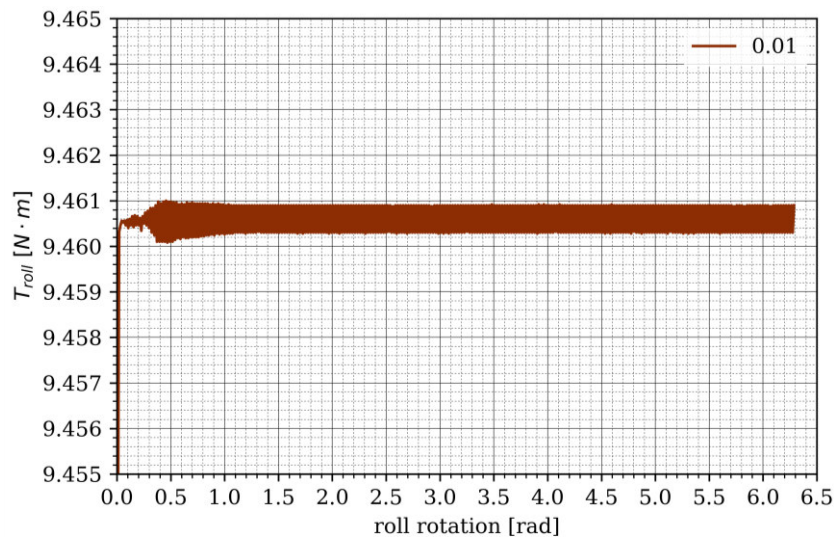


Figure 4.61 - Roll torque during the rotation phase for a contact detection of 0.01.

The roll force during the simulation (Figure 4.62) is consistent and, unlike the roll torque, does not show imprecisions for any of the contact distance tolerance studied.

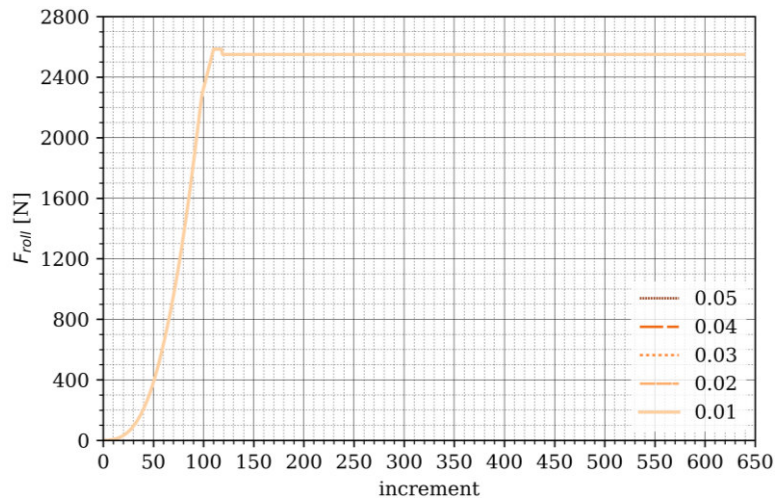


Figure 4.62 - Roll force during the simulation.

The maximum contact normal stress evolution during the simulation is shown in Figure 4.63. Similarly to the roll torque, the maximum contact normal stress is stable during the penetration and coincident for the different contact distance tolerances studied. During the rotation, a different behavior is observed.

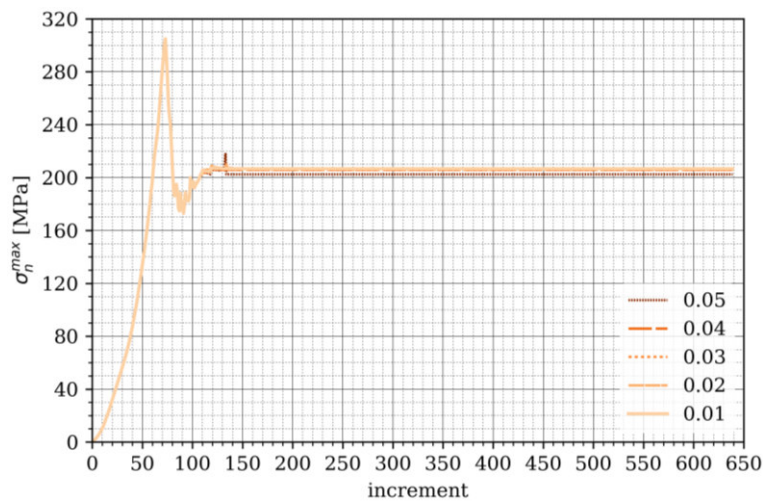


Figure 4.63 - Maximum contact normal stress during the simulation.

Figure 4.64 represents the maximum contact normal stress during the roll rotation. Oscillations are visible until the roll rotates, approximately, 0.2 rad . From this point, the contact normal stress is constant. These oscillations happened at the same increments as the oscillations in the torque.

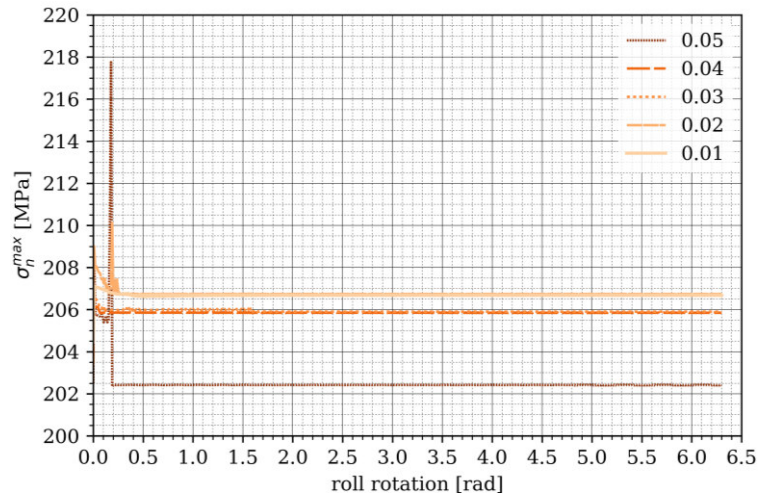


Figure 4.64 - Maximum contact normal stress during the roll rotation.

An analysis of the torque and the maximum contact normal stress during the rotation (Figure 4.60 and Figure 4.64) prove that the contact distance tolerance has a substantial influence on the numerical stability.

In order to study if these instabilities have implications in the contact normal stress distribution, Figure 4.65 and Figure 4.66 represent the contact normal stress distribution at the penetration last increment and at the rotation last increment, respectively.

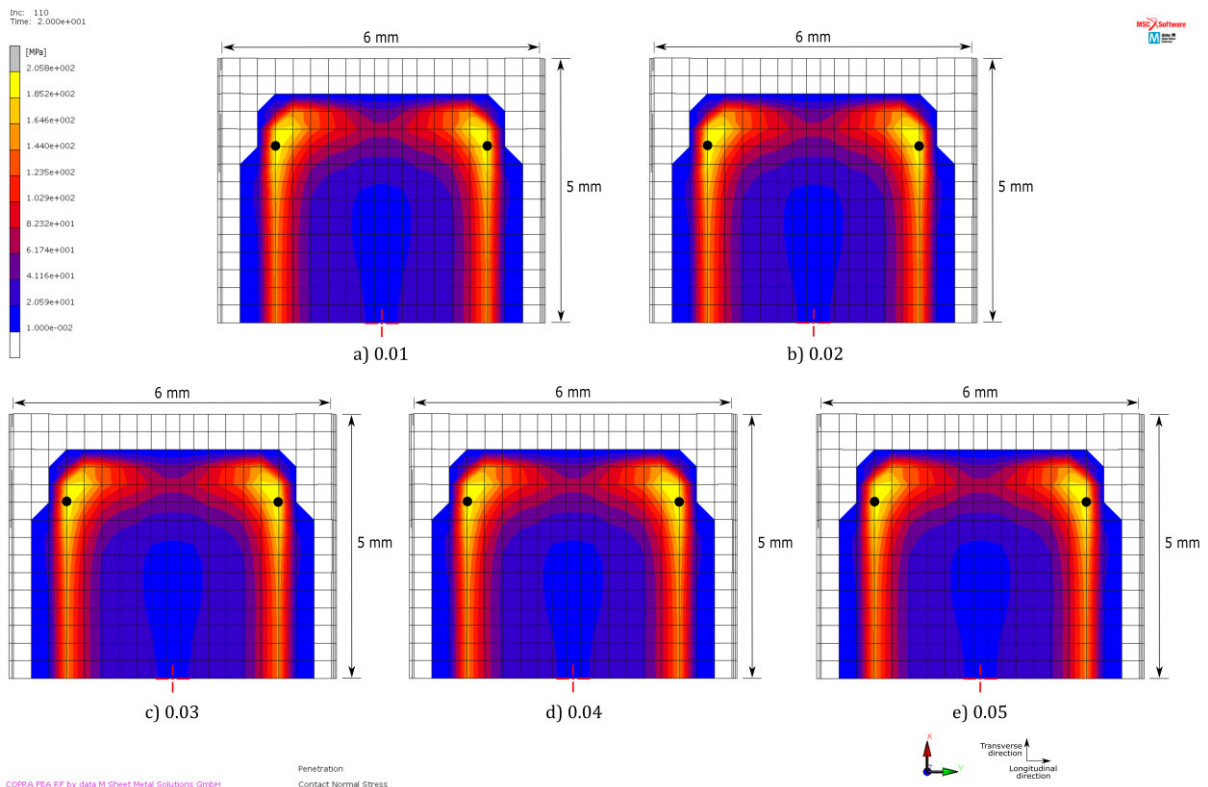


Figure 4.65 - Contact normal stress distribution in penetration last increment for different contact distance tolerances.

The contact normal stress distributions are barely indistinguishable. Table 4.7 states the maximum contact normal stress at the penetration last increment. The biggest difference

observed is between the contact distance tolerance of 0.02 and 0.04 and the second one is only 1 % lower than the first.

Table 4.7 - Maximum contact normal stress for the different contact distance tolerances at the penetration last increment.

Distance tolerance	σ_n^{max} [MPa]
0.01	205.0
0.02	205.8
0.03	203.7
0.04	203.5
0.05	203.6

Figure 4.66 represent the contact normal stress distribution at the rotation last increment. An analysis of Figure 4.66 shows that the contact normal stress is not influenced by the contact distance tolerance.

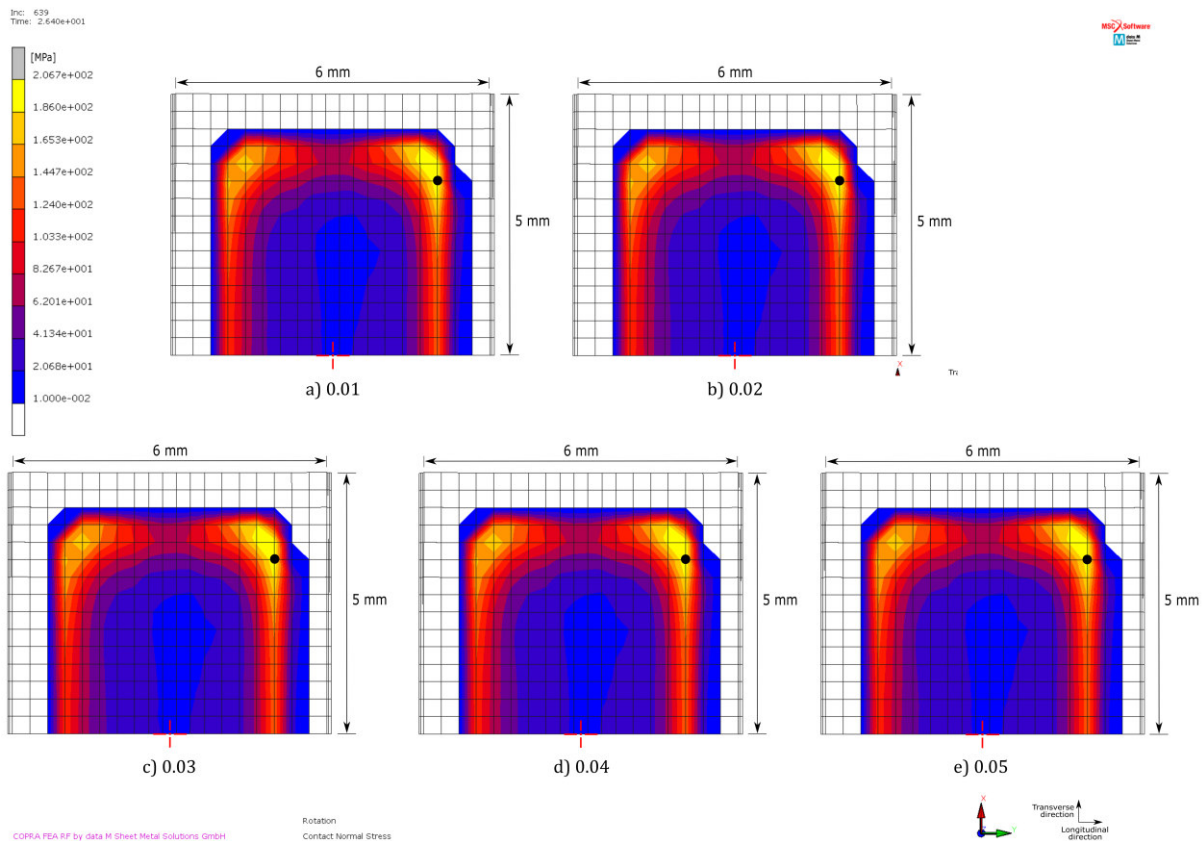


Figure 4.66 - Contact normal stress distribution in rotation last increment for different contact distance tolerances.

Again, at the rotation last increment the contact normal stress distributions are barely indistinguishable. In Table 4.8 the maximum contact normal stresses at the rotational last increment are stated. This time the biggest difference is observed between the contact distance tolerance of 0.01, 0.02 and 0.05. The lower maximum contact normal stress observed is only 2 % lower than the larger value observed. Thus, it is possible to conclude that the contact distance tolerance does not influence the contact normal stress distribution.

Table 4.8 - Maximum contact normal stress for the different contact distance tolerances at the rotation last increment.

Distance tolerance	σ_n^{max} [MPa]
0.01	206.7
0.02	206.7
0.03	205.9
0.04	205.9
0.05	202.4

The computational time for each contact distance tolerance studied is stated in Figure 4.67. A lower distance tolerance, corresponds to a lower computational time. Between a distance tolerance of 0.01 and 0.05 it is accomplished a reduction of 46 % of the simulation computation time.

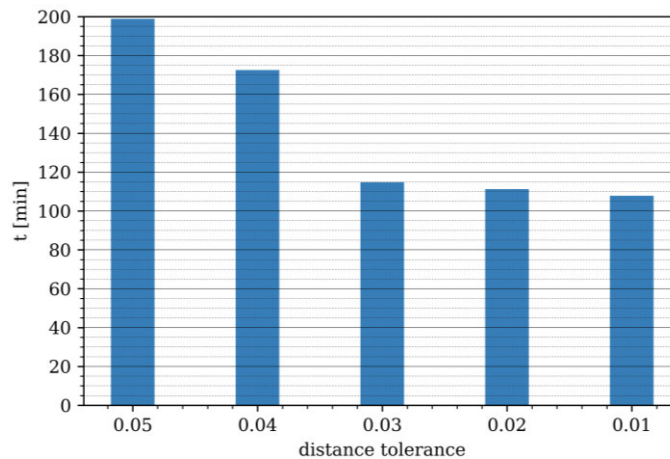


Figure 4.67 - Simulation computational time for different contact distance tolerances.

The number of nodes in contact is influenced by the contact distance tolerance. When the roll starts rotating some instabilities are observed. For a defined contact distance tolerance of 0.02, 0.03, 0.04 and 0.05, nodes enter in contact and separate again. Similarly, the roll torque does not converge immediately to the dynamic torque and the maximum contact normal stress also oscillates in the beginning of the rotation.,

The contact distance tolerance of 0.01 shows a better response in terms of torque and maximum contact normal stress during the rotation (Figure 4.60 Figure 4.64). The simulation with this value is not stable (Figure 4.61), even though the torque oscillates with an amplitude lower than $0.001 N \cdot m$. Thus, and considering the computational time, this parameter was adopted and a study of the bias factor was performed.

4.2.2 BIAS FACTOR

This section focused on the study of the bias factor parameter. It aims to understand this parameter influence on the contact representation and eliminate the instability observed for the torque calculation with a distance tolerance of 0.01.

Given this parameter direct influence on the contact detection, firstly, was performed an analysis of the number of nodes in contact. Then, the stability of the roll rotation was confirmed, followed by an analysis of the forces acting on the roll, namely the roll torque and the roll force. Lastly, the maximum contact normal stress evolution and the contact normal stress distribution were analysed.

In this study, the bias factor previously used - 0.95 - was compared with a bias factor of 0.90. As mentioned previously, the contact distance tolerance used was 0.01.

The number of nodes in contact during the different simulations is represented in Figure 4.68. In this representation is visible a consistent number of nodes in contact during the penetration (until increment 110). However, after increment 130 an irregularity is observed.

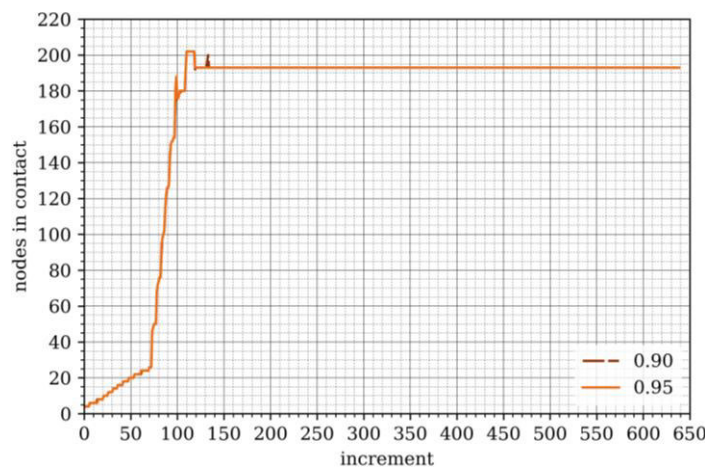


Figure 4.68 - Number of nodes in contact during the simulation for different bias factors.

Figure 4.69 represents the number of nodes in contact during the roll rotation. Between a rotation of 0.1 rad and 0.2 rad, for a bias factor of 0.90 seven nodes enter in contact at increment 138. Six elements separate at the increment 139 and the last one separates at increment 140. After this moment, both solutions converge to 193 nodes in contact.

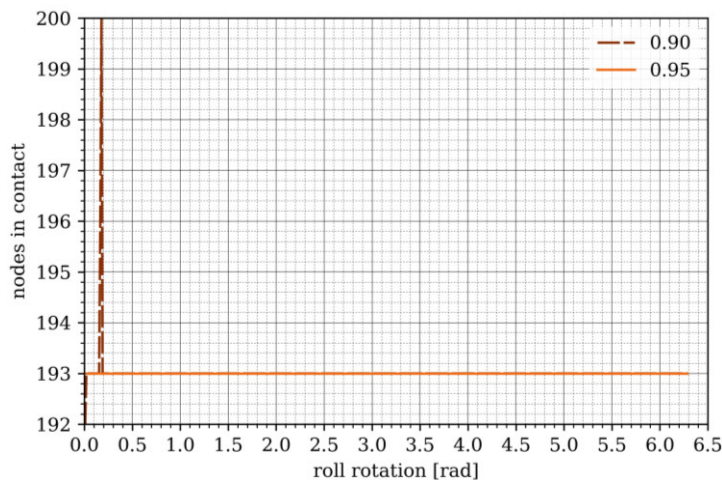


Figure 4.69 - Number of nodes in contact during the roll rotation for different bias factors.

In order to investigate if the nodes entering in contact and separating in the following increments have consequences in the contact representation, the contact normal stress at increment 140 was compared for the two simulations Figure 4.70.

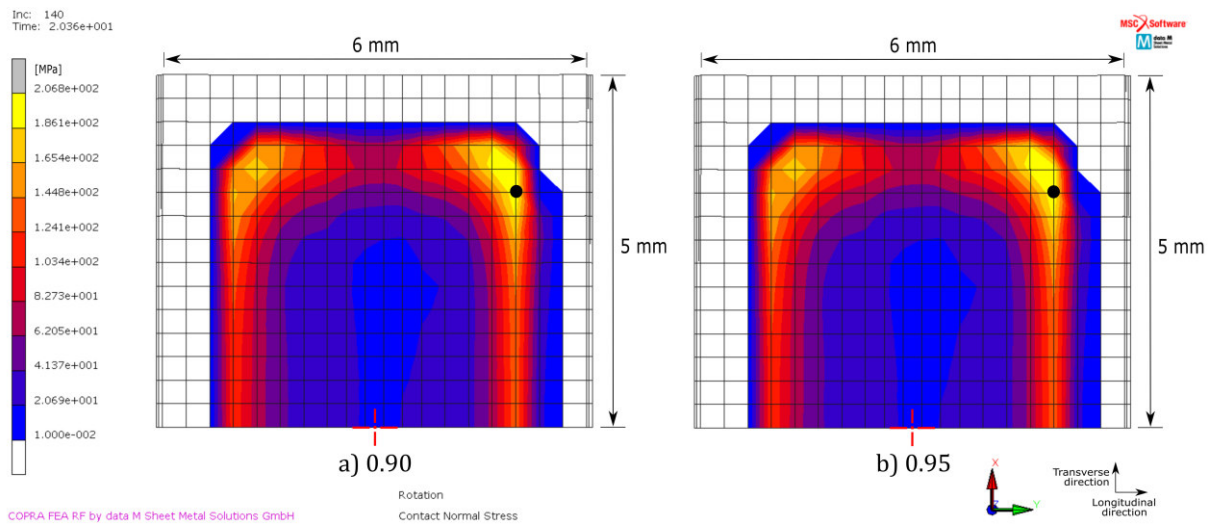


Figure 4.70 - Contact normal stress distribution at increment 140 for different bias factors.

The contact stress distributing for both cases are barely indistinguishable. In fact, the maximum contact normal stress for a bias factor of 0.90 and 0.95 are, respectively, 206.8 MPa and 206.7 MPa . This is equivalent to a difference less than 0.05 %. Therefore, the imprecision in the number of nodes in contact did not influenced the contact normal stress.

A representation of the roll rotation during the simulation is shown in Figure 4.71. The rotation is contact during the penetration and increases with a constant slope when the roll starts rotating, being coincident for all contact distance tolerances studied. Thus, the roll rotation does not show any instability for the different distance tolerances tested.

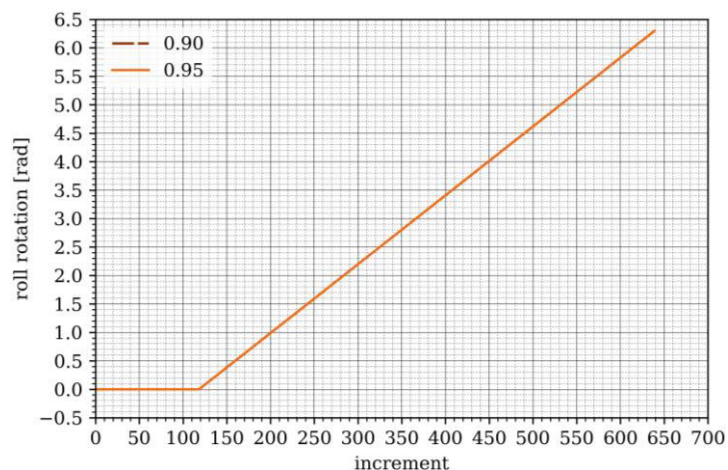


Figure 4.71 - Roll rotation during the simulation for different bias factors.

Figure 4.72 represents the roll torque during the simulation. Observing the roll torque during the penetration, it was not found any imprecision. However, when the roll starts rotating, the torque oscillates until it converges to the dynamic torque. Therefore, is needed to perform a deeper analysis of the torque during the rotation.

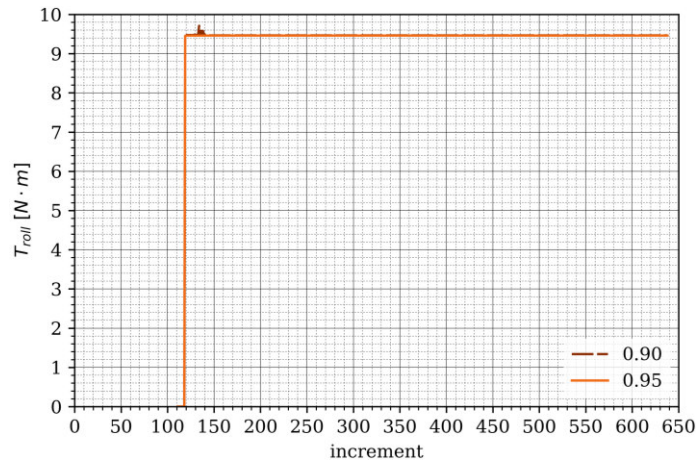


Figure 4.72 - Roll torque during the simulation for different bias factors.

The roll torque during the roll rotation is represented in Figure 4.73. For a defined bias factor of 0.90, the roll torque does not converge immediately to the dynamic torque.

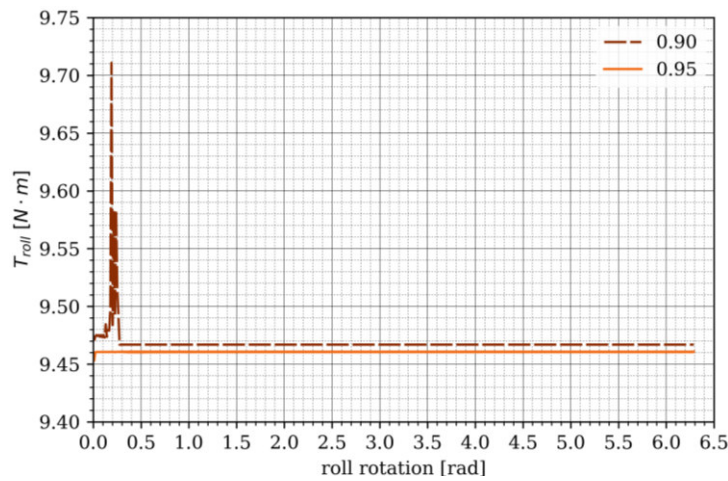


Figure 4.73 - Roll torque during the roll rotation for different bias factors.

Analysing in more detail the roll torque for both bias factors (Figure 4.74), is observed that the simulation is searching for an equilibrium only for the bias factor of 0.95. Thus, the bias factor of 0.90 eliminated the simulation instability.

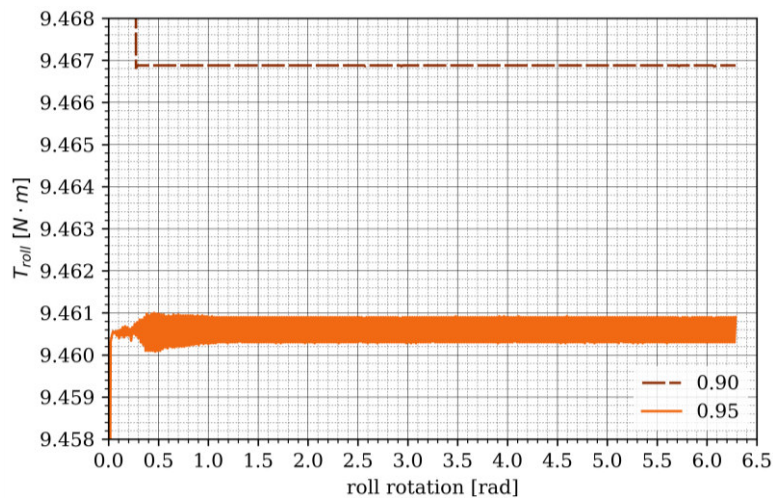


Figure 4.74 - Roll torque during the rotation phase for different bias factors.

The roll force during the simulation (Figure 4.75) is consistent and, unlike the roll torque, does not show imprecisions for both bias factors studied.

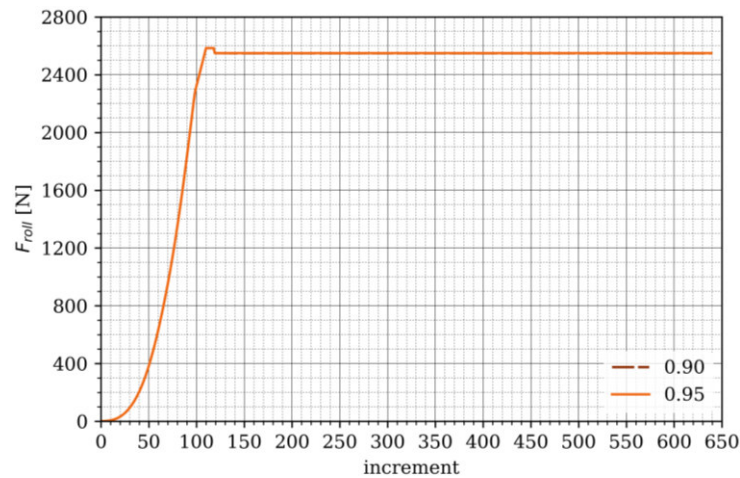


Figure 4.75 - Roll force during the simulation for different bias factors.

The maximum contact normal stress evolution during the simulation is shown in Figure 4.76. Similarly to the roll torque, the maximum contact normal stress is stable during the penetration and coincident for the different bias factors studied. During the rotation, a different behavior is observed.

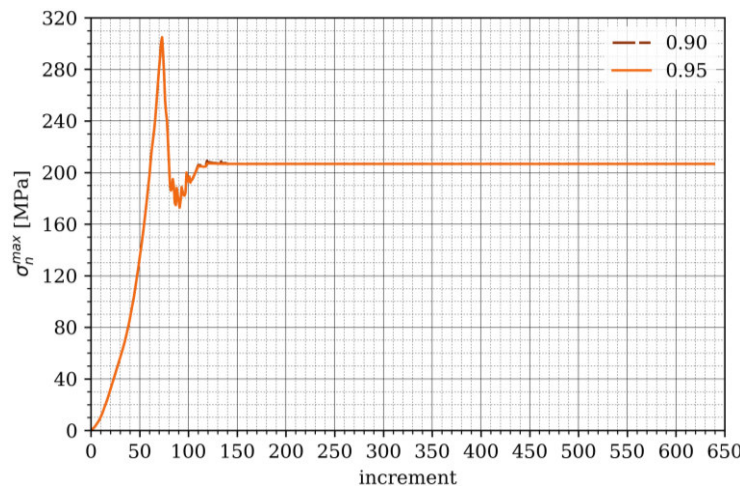


Figure 4.76 - Maximum contact normal stress during the simulation for different bias factors.

Figure 4.77 represents the maximum contact normal stress during the roll rotation. Oscillations are visible until the roll rotates, approximately, 0.2 rad . From this point, the maximum contact normal stress is maintained constant. Should be noticed that the amplitude of the oscillation corresponds only to 1% of the constant maximum contact normal stress. Besides, these oscillations happened at the same increments when nodes entered in contact and separated in the preceding increments. A study of the increment when the simulation reaches a constant value showed that this variations did not influenced the contact normal stress distribution.

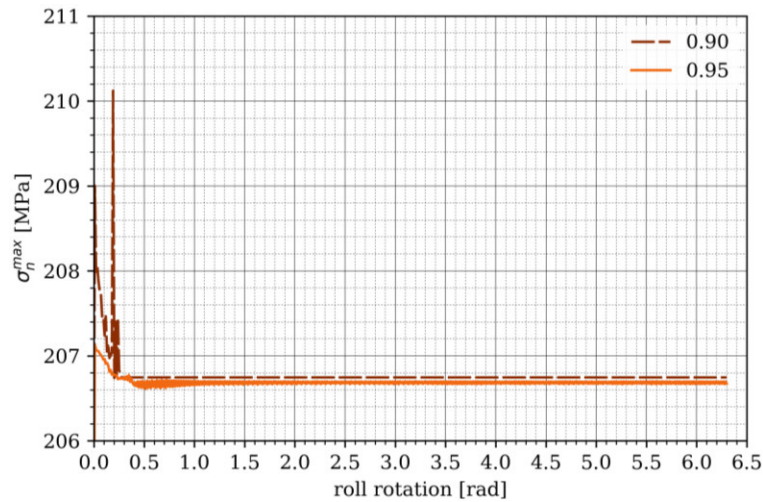


Figure 4.77 - Maximum contact normal stress during the roll rotation for different bias factors.

In order to confirm if these instabilities had implications in the contact normal stress distribution, Figure 4.78 and Figure 4.79 represent the contact normal stress distribution at the penetration last increment and at the rotation last increment, respectively

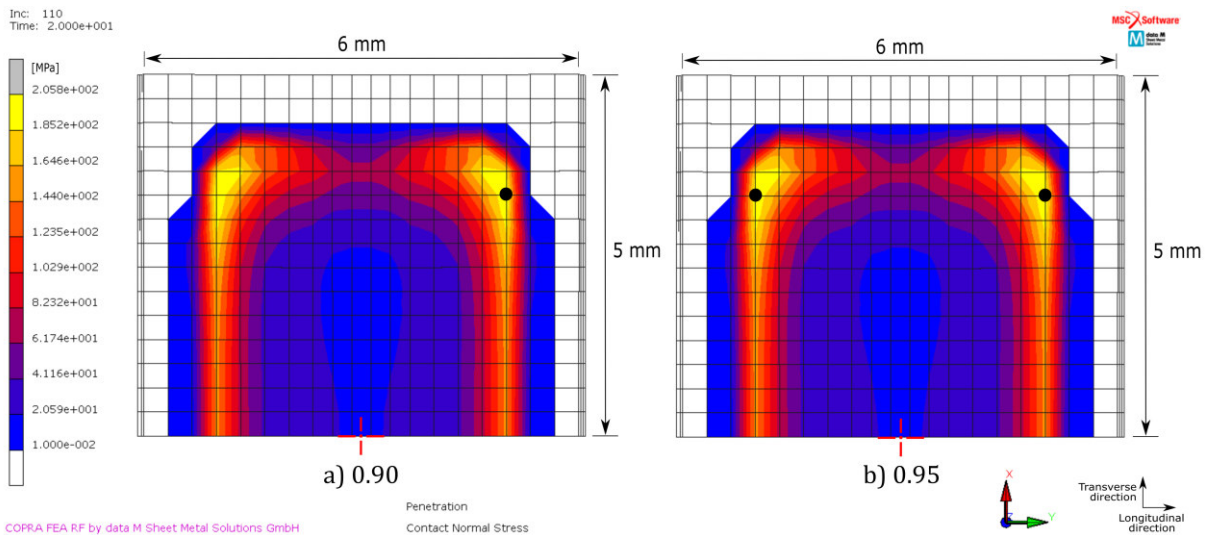


Figure 4.78 - Contact normal stress distribution in penetration last increment for different bias factors.

The contact normal stress distributions are barely indistinguishable. In fact, the maximum contact normal stress is the same. A similar analysis was performed for the rotation last increment. In Figure 4.79 is represented the contact normal stress distribution at the rotation last increment.

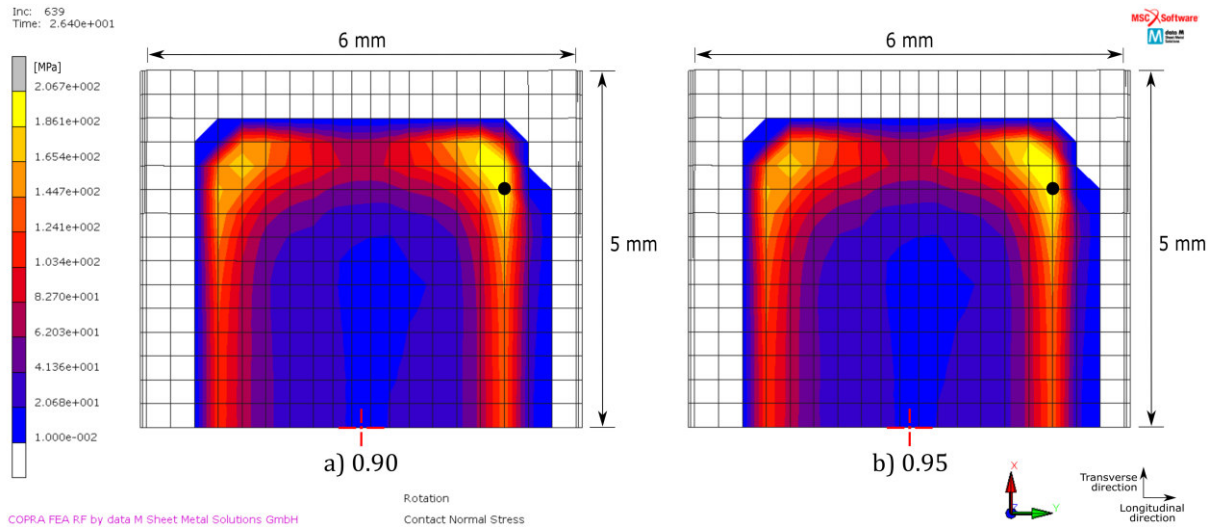


Figure 4.79 - Contact normal stress distribution in rotation last increment for different bias factors.

Again, at the rotation last increment the contact normal stress distributions are barely indistinguishable and the maximum contact normal stress is equal in both cases. Regarding the computational cost, the differences are substantial. A bias factor of 0.95 took 108 *min* to calculate, only 5 *min* less than the bias factor of 0.90.

Similarly to the distance tolerance, the bias factor also influences the number of nodes in contact. When the roll begins rotating, some nodes enter in contact prematurely when a bias factor of 0.90 is used. However, should be noticed that this is only observed in the initial increments of the rotations and the simulation immediately converges to a constant value. Besides, an analysis of the contact normal stress distribution after that discontinuity showed an indistinguishable distribution for both models with a bias factor of 0.95 and 0.90. The roll torque and maximum contact normal stress evolutions shows a similar behaviour, for a bias factor of 0.90 it increases in the beginning of the roll rotations and immediately falls to a constant value. A further analysis of the contact normal stress distribution in the end of the penetration phase and in the end of the rotation phase showed similar distributions. Even though, the bias factor of 0.90 exhibits instabilities in the initial increments of the roll rotation, the results converge immediately and a bias factor of 0.90 is stable after it converges. Thus, when a bias factor of 0.90 is combined with a distance tolerance of 0.01 the torque instabilities are eliminated.

4.3 FRICTION MODELING

This section presents the study of the friction modelling influence on the contact representation. This study continues the optimisation of the FE model, using the optimised mesh discretisation resultant from the study outlined in section 4.1 and the contact search definition resultant from the study outlined in section 4.2.

The friction models available in current FEA software are stated in Figure 4.80.

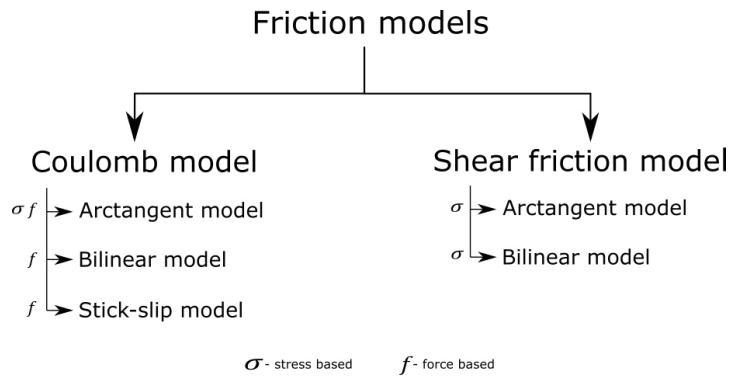


Figure 4.80 - Friction models and correspondent numerical implementation supported by COPRA® FEA RF.

Within the Coulomb friction law, the FEA software allows three different numerical implementations (Figure 4.81).

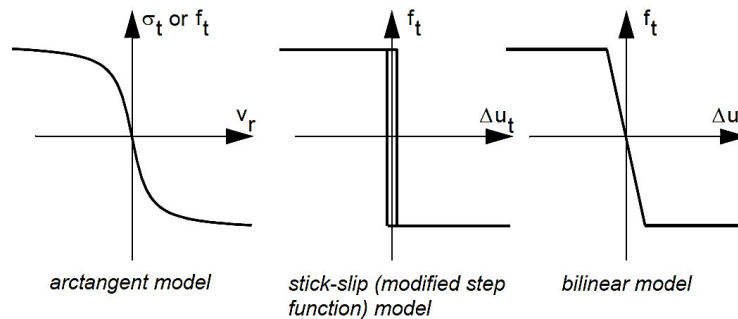


Figure 4.81 - Friction numerical models available in COPRA® FEA RF. Retrieved from [MSC SOFTWARE 2016A].

This study focusses on the bilinear and arctangent Coulomb models. Firstly, a study of the friction influence was performed. The metal sheet final geometry and the contact normal stress distribution were analysed. In this study, a model without friction was compared with a bilinear Coulomb model. Then, an arctangent numerical implementation was compared with the bilinear Coulomb model.

The possible contact zone was discretised into elements with a square top face dimension of 0.333 mm and the thickness was discretised into 3 elements. The contact distance tolerance was 0.01 with a bias factor of 0.90.

The roll was not set to rotate with a contact speed, but with different rotation speeds. With this change, a varying sliding velocity is accomplished, allowing to study the variation of the friction forces with changes in the sliding velocity. The angular displacement imposed to the roll is represented in Figure 4.82.

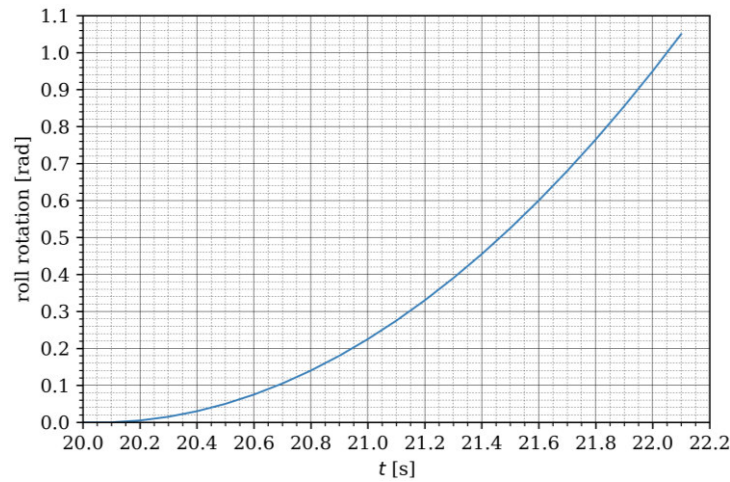


Figure 4.82 - Rotation imposed to the roll during the rotation phase for the friction study.

The resultant roll velocity is a step time dependent function that makes the roll rotate from $0 \text{ rad} \cdot \text{s}$ to $1 \text{ rad} \cdot \text{s}$, with increments of $0.05 \text{ rad} \cdot \text{s}$ and rotating at each rotational speed during 0.1 s (Figure 4.83).

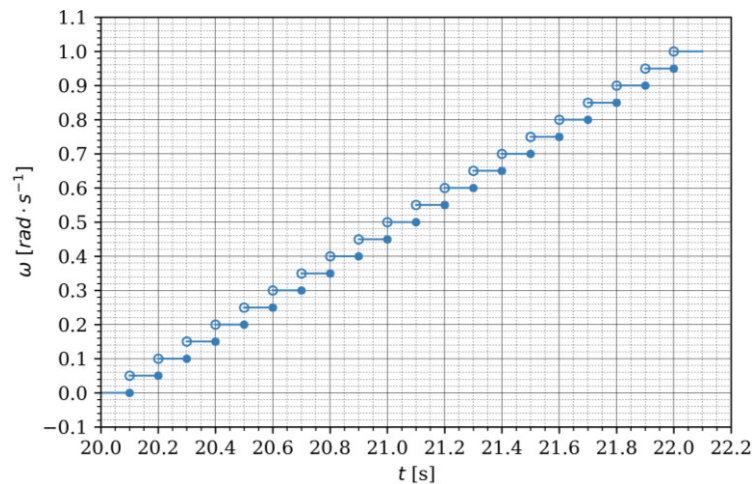


Figure 4.83 - Angular velocity imposed to the roll during the rotation phase for the friction study.

The integration time step was defined to 0.01 s , obtaining 10 increments for each rotation velocity.

4.3.1 FRICTION INFLUENCE

This section outlines the study of the friction influence on the bending representation and the contact characterisation.

Firstly, the bending geometry and the evolution of the roll force were analysed. Then, the maximum contact normal stress evolution was analysed, followed by a comparison of the contact normal stress distribution in each simulation.

Two different models were created: one without friction and other with a bilinear Coulomb friction model.

The longitudinal bending geometry for the possible contact zone at the penetration last increment is represented in Figure 4.84.

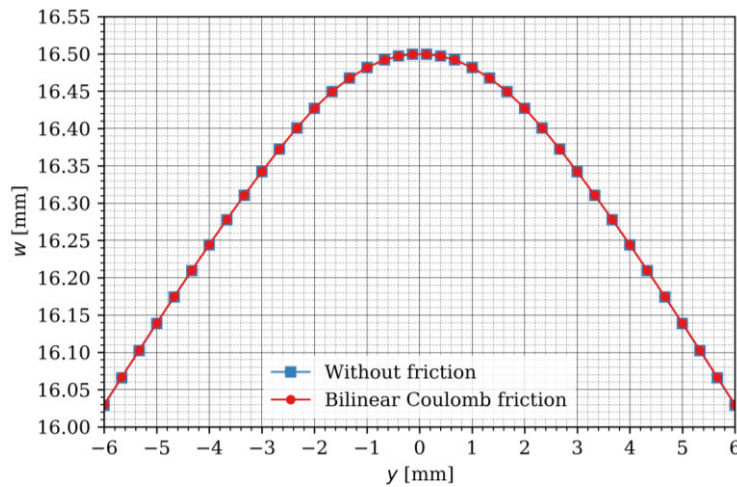


Figure 4.84 - Longitudinal bending geometry for the possible contact zone using a model without friction and a bilinear Coulomb model; calculated at the penetration last increment.

The longitudinal bending geometry for the “fixed” zone at the penetration last increment is represented in Figure 4.85.

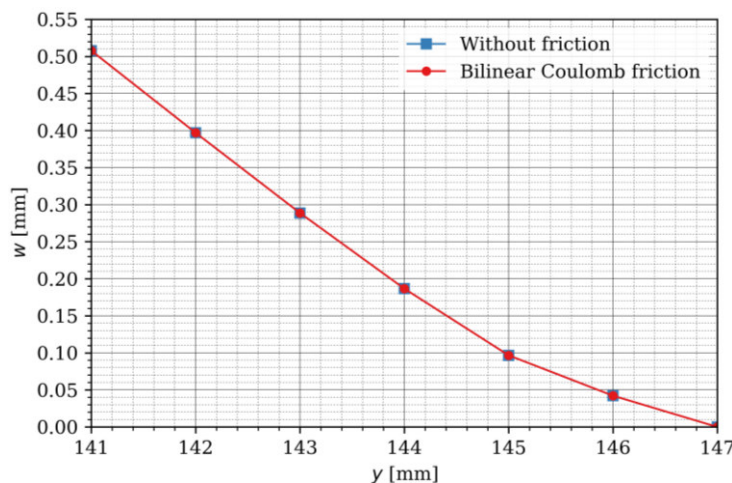


Figure 4.85 - Longitudinal bending geometry for the “fixed” zone using a model without friction and a bilinear Coulomb model; calculated at the penetration last increment.

The longitudinal bending geometry representation is coincident for both representations. During the penetration, there is no friction acting in the longitudinal direction. Thus, it was expected to have coincident lines.

The transverse bending geometry at the penetration last increment is represented in Figure 4.86. This representation is not coincident for both models. During the penetration, there is friction acting in the transverse direction due to the relative movement induced by the transverse bending. Thus, a different transverse bending geometry was expected. However, a comparison of the exterior node displacement in both models shows a difference of only 0.6 %.

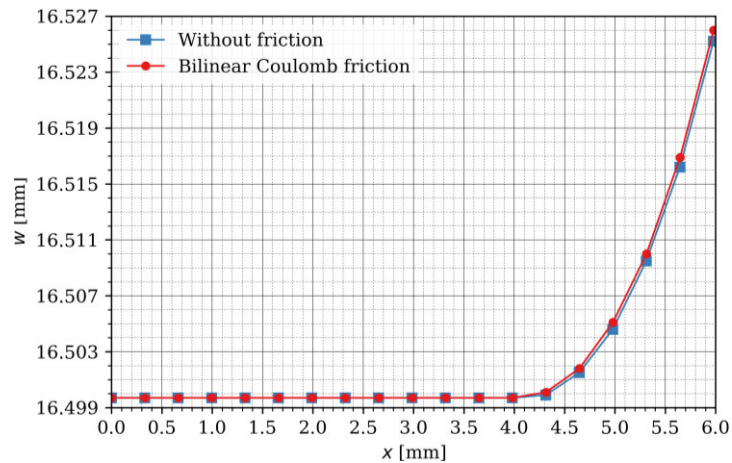


Figure 4.86 – Transverse bending geometry using a model without friction and a bilinear Coulomb model; calculated at the penetration last increment.

The longitudinal bending geometry for the possible contact zone at the rotation last increment is represented in Figure 4.87

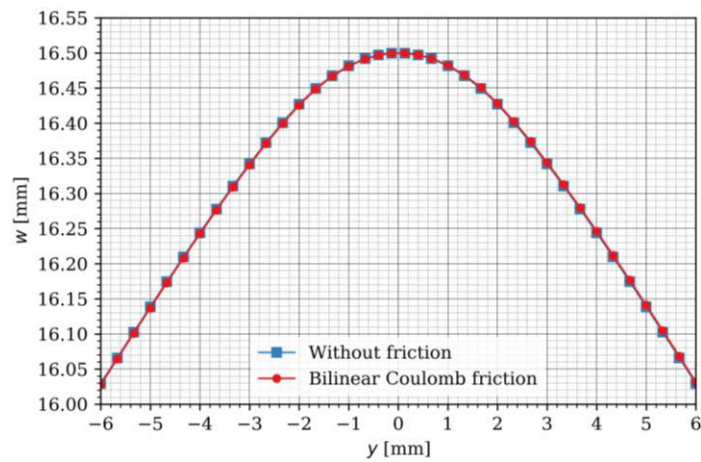


Figure 4.87 - Longitudinal bending geometry for the possible contact zone using a model without friction and a bilinear Coulomb model; calculated at the rotation last increment.

Figure 4.88 represents the longitudinal bending for the “fixed” zone at the rotation last increment. The longitudinal bending is barely indistinguishable for both representations.

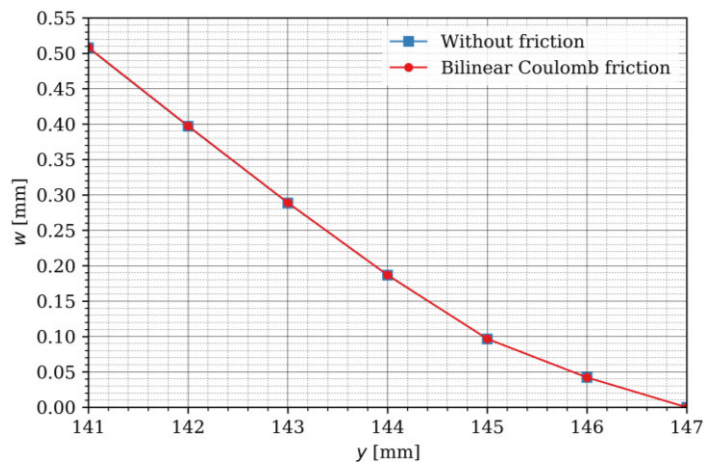


Figure 4.88 - Longitudinal bending geometry for the “fixed” zone using a model without friction and a bilinear Coulomb model; calculated at the rotation last increment.

The transverse bending geometry at the rotation last increment is represented in Figure 4.89. The difference observed in the transverse geometry is similar to the difference observed already at the penetration last increment.

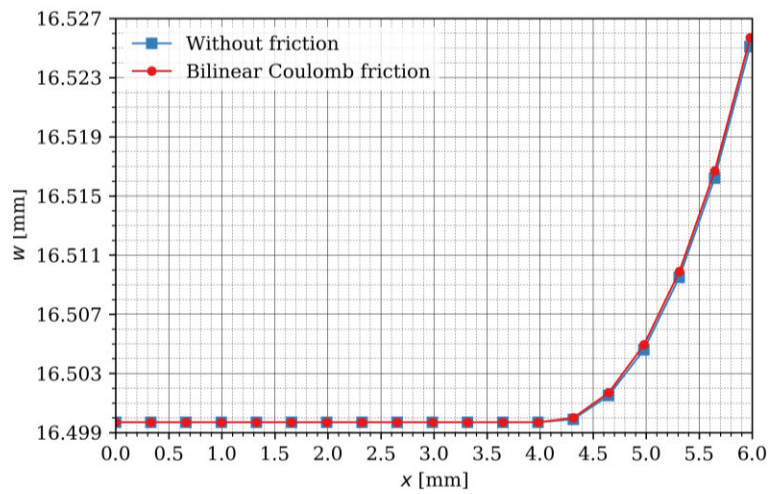


Figure 4.89 – Transverse bending geometry using a model without friction and a bilinear Coulomb model; calculated at the rotation last increment.

Figure 4.90 illustrates the roll force evolution during the simulation. This analysis shows that the roll force has a minimal influence in the friction, however, once the roll starts rotating the roll force decreases in the model with friction.

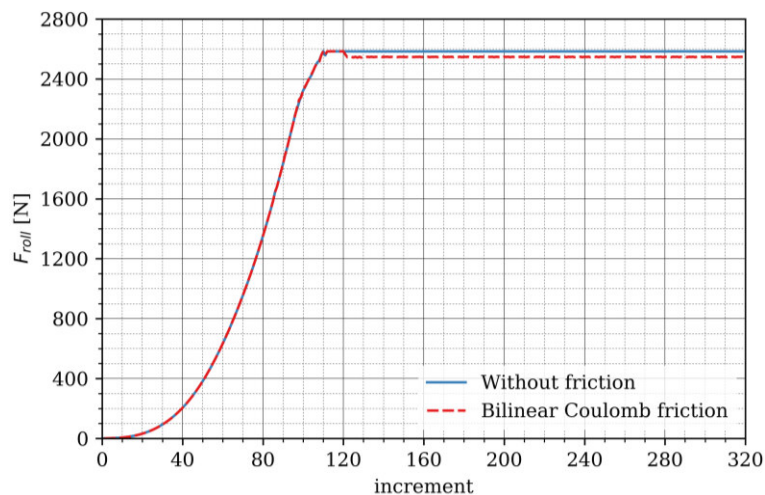


Figure 4.90 - Roll force during the simulation for a model without friction and a model with a bilinear Coulomb friction model.

A representation of the maximum contact normal stress evolution during the simulation (Figure 4.91) shows the same evolution for both models. This suggests that the friction does not influence the contact normal stress at the contact area.

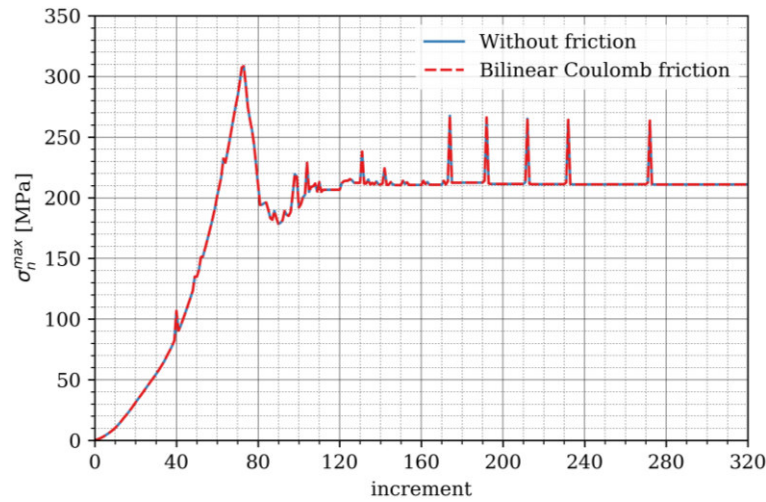


Figure 4.91 - Maximum contact normal stress during the simulation for a model without friction and a model with a bilinear Coulomb friction model.

Contact normal stress distribution for both models at the penetration last increment is represented in Figure 4.92. The representations are barely indistinguishable. In fact, the maximum contact normal stress for the model without friction is only 2 % higher than the correspond value in the model with a bilinear Coulomb friction model.

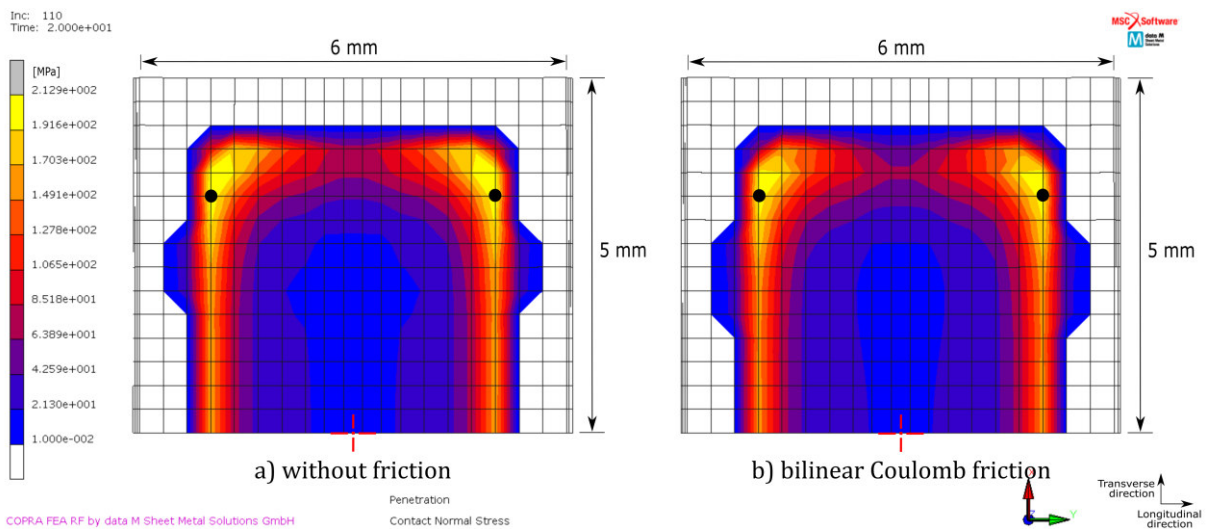


Figure 4.92 - Contact normal stress distribution for a model without friction and a model with a bilinear Coulomb friction model; calculated at the penetration last increment.

Figure 4.93 represents the contact normal stress distribution for both models at the rotation last increment. In this case, a different distribution is observed. After the rotation, the contact normal stress is no longer symmetric in the longitudinal direction and goes from a four-point contact to a two-point contact.

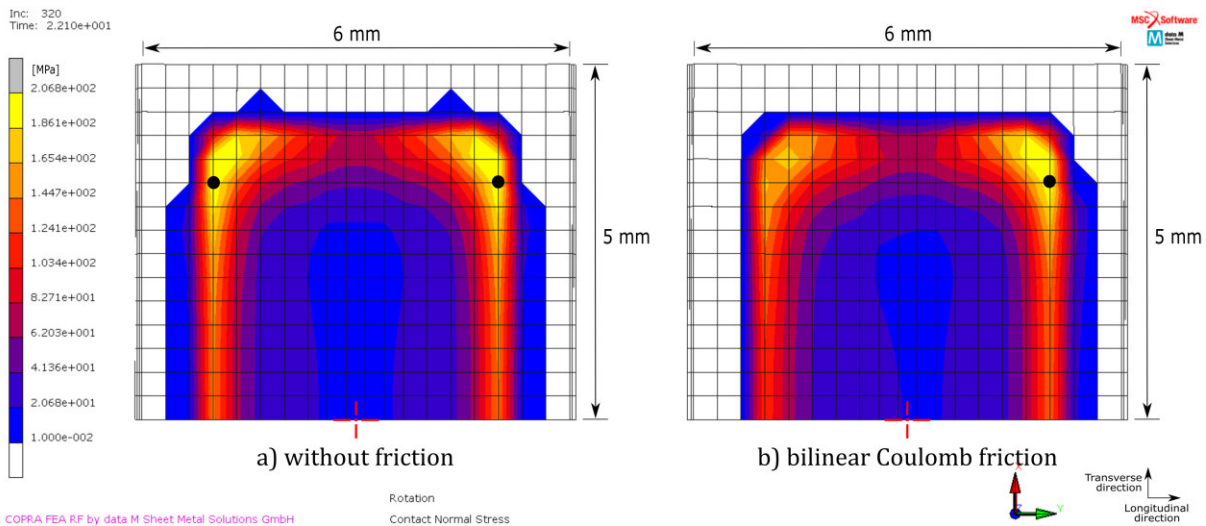


Figure 4.93 - Contact normal stress distribution for a model without friction and a model with a bilinear Coulomb friction model; calculated at the rotation last increment.

The longitudinal bending is not influenced by friction, however, the same is not valid for the transverse bending. This shows a slightly different geometry when friction is taken into account in the calculations. The roll force is also coincident during the penetration phase, even though it exhibits a slight lower roll force in the model with friction when the roll begins rotating. In the end of the rotation phase, the contact normal stress does not show differences, however, in the end of the rotation phase the same is not valid. The contact normal stress has a different distribution when friction is taken into account. Thus, the friction influences mainly the contact representation and has a minimal influence on the bending geometry.

4.3.2 NUMERICAL IMPLEMENTATION

This section outlines the comparison of two different numerical implementation of the friction model.

Initially, the evolution of the roll force and the roll torque were analysed. Then, the maximum contact normal stress evolution was analysed, followed by a comparison of the contact normal stress distribution in each simulation.

The arctangent Coulomb friction model was compared with the bilinear Coulomb friction law. The arctangent model [MSC SOFTWARE 2013] is usually used to avoid discontinuity problems and is stated as:

$$\begin{aligned}
 F_t &= \mu \cdot F_n \cdot \left[\frac{2}{\pi} \cdot \tan^{-1} \frac{v_r}{C} \right] \\
 \sigma_t &= \mu \cdot \sigma_n \cdot \left[\frac{2}{\pi} \cdot \tan^{-1} \frac{v_r}{C} \right]
 \end{aligned}
 \tag{4.3.1}$$

where

F_t is the friction force

F_n is the contact normal force

C is the user defined relative sliding velocity at which full friction occurs

v_r is the sliding velocity

σ_t is the friction stress

σ_n is the contact normal stress.

The arctangent Coulomb model relative velocity threshold was set to its default value of 1.

Figure 4.94 represents the frictional model implemented.

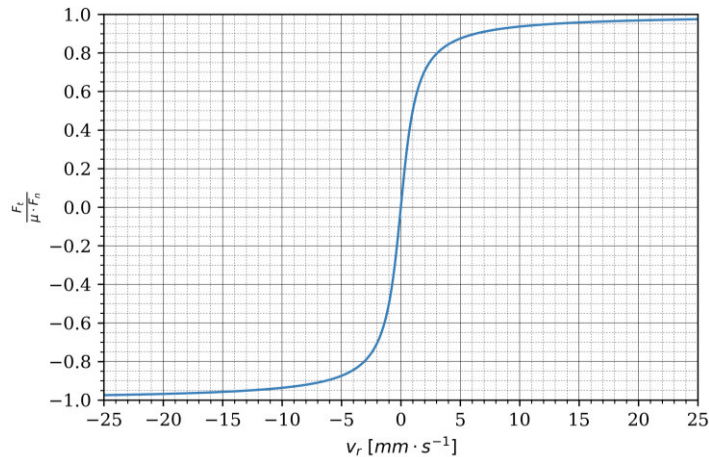


Figure 4.94 - Arctangent Coulomb friction law implemented in the model.

The sliding velocity at the contact area during the rotation is represented in Figure 4.95.

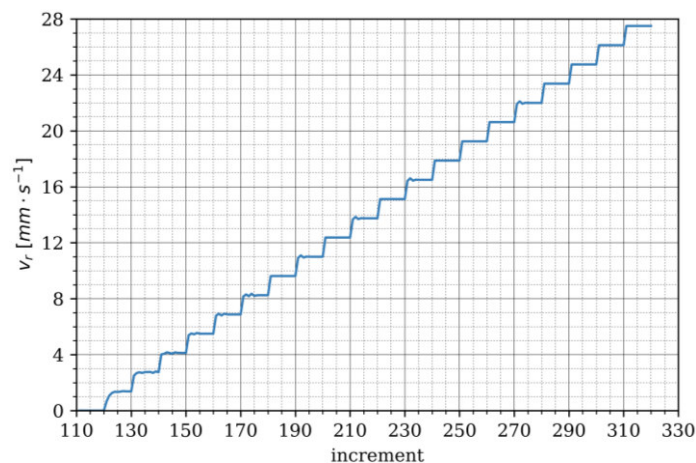


Figure 4.95 - Sliding velocity at the contact area during the rotation.

In order to study the friction numerical implementation influence on the contact representation, the rotation load case was analysed looking the roll force, roll torque, bending geometry, contact normal stress and friction stresses.

Figure 4.96 represents the roll force evolution during the rotation of the roll. It is visible that the roll force is coincident for both friction models.

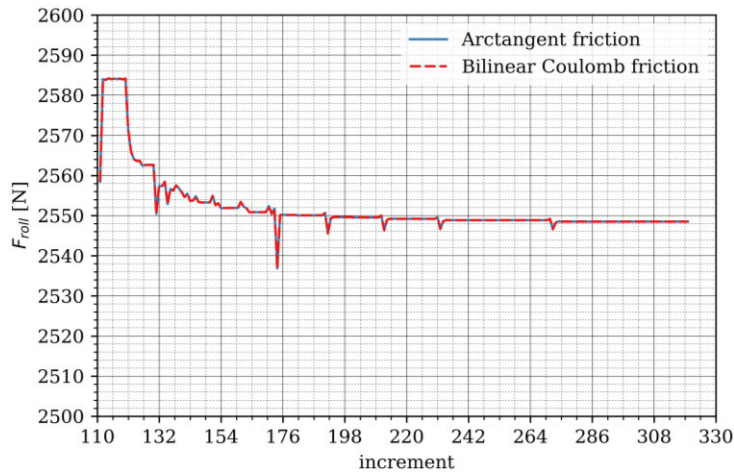


Figure 4.96 - Roll force during rotation for different friction numerical implementations.

The roll torque evolution during the rotation is shown in Figure 4.97. The roll torque calculated was not influenced by the friction model. However, a visible dependence on the sliding velocity is visible.

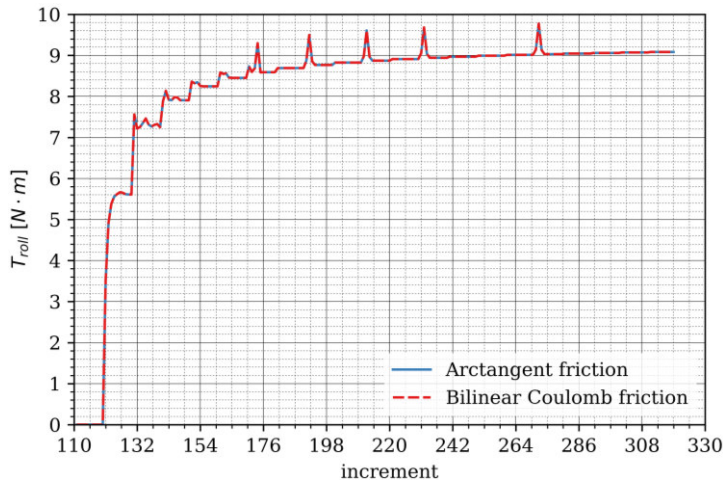


Figure 4.97 - Roll torque during rotation for different friction numerical implementations.

The maximum contact normal stress evolution is shown in Figure 4.98. Similarly, the friction model did not influence the maximum contact normal stress evolution. A bilinear model has, also, a friction stress dependent on the sliding velocity. Since the slip threshold calculation was being calculated automatically, it is possible that this calculation has led to friction model similar to the one implemented with the arctangent model.

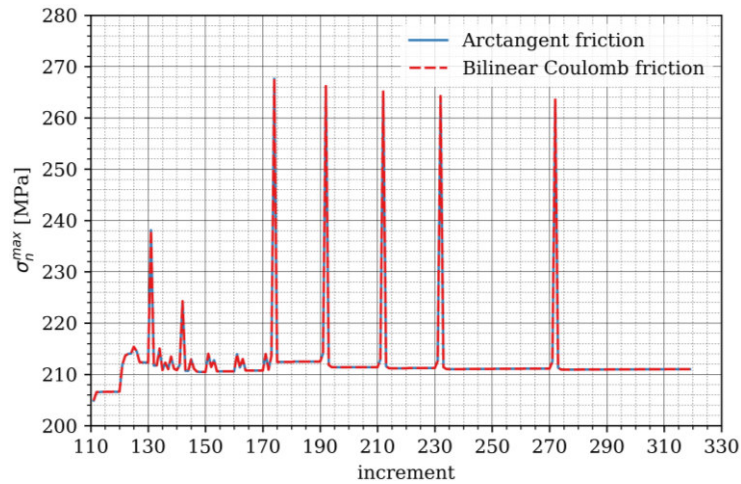


Figure 4.98 - Maximum contact normal stress during rotation for different friction numerical implementations.

The contact normal stress distribution at the last increment of the rotation is represented in Figure 4.99. The bilinear model has a contact normal stress distribution different from the contact normal stress distribution previously observed at the penetration last increment. On the other hand, the arctangent model has a contact normal stress distribution more similar to the distribution observed at the penetration last increment – a distribution with symmetry in the longitudinal direction. This difference is possibly related to a smoother transition verified in the arctangent model.

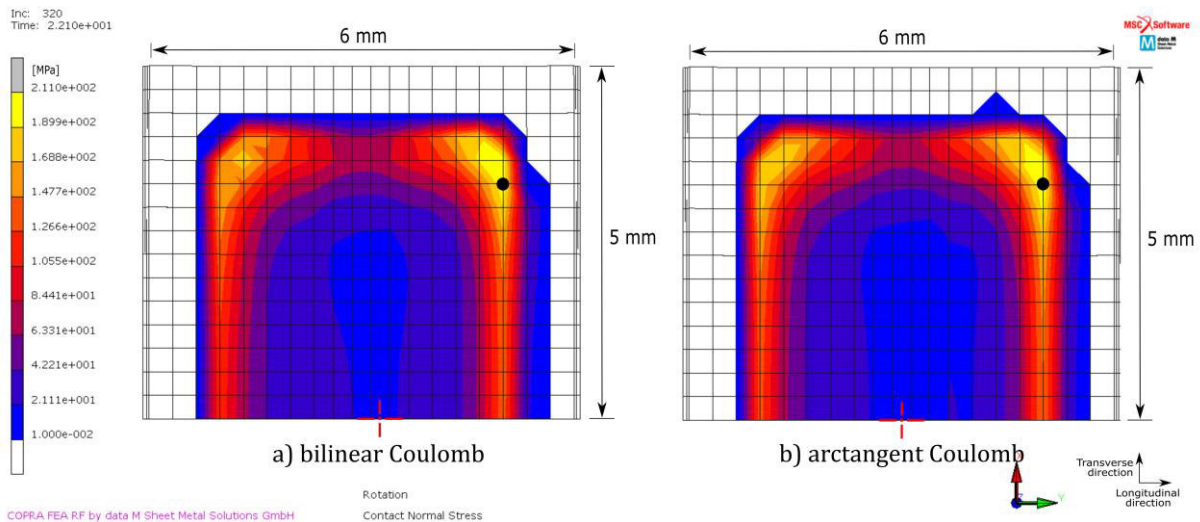


Figure 4.99 - Contact normal stress distribution for the different friction models; calculated at the rotation last increment.

Figure 4.100 represents the friction stress at the rotation last increment for the bilinear and arctangent Coulomb friction model. The friction stress distribution is similar to the contact normal stress distribution.

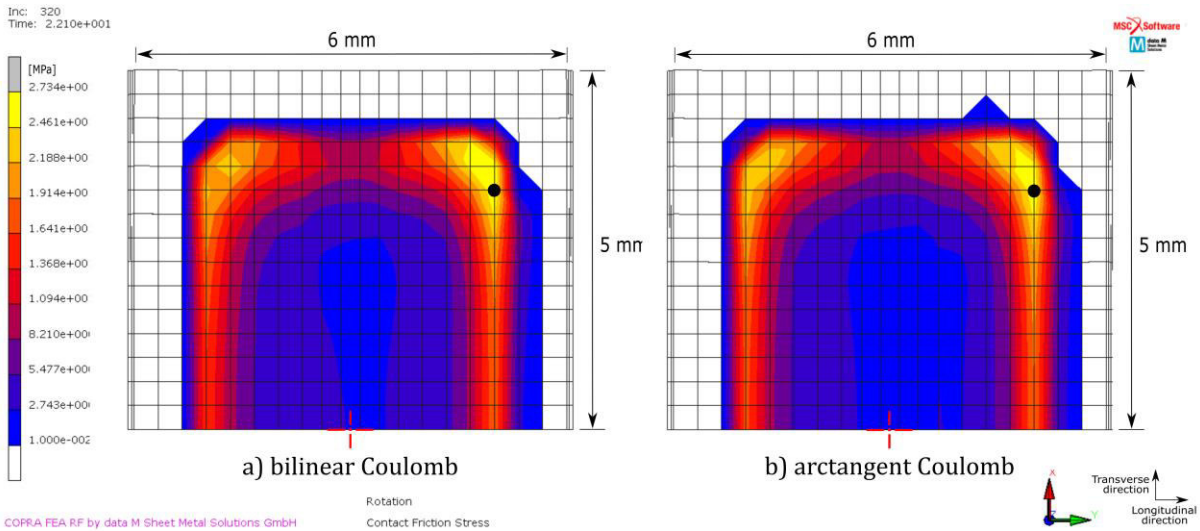


Figure 4.100 - Contact friction stress distribution for the different friction models; calculated at the rotation last increment.

The bilinear Coulomb model and the arctangent Coulomb model did not show differences during the rotation in terms of roll force, roll torque and maximum contact normal stress. However, different contact normal stress and friction stress distribution were observed in the end of the rotation. This suggests that the friction model influences the contact normal stress.

4.4 OPTIMISED FE MODEL

In this section is presented the optimal parameters that resulted from the study outlines in sections 4.1, 4.2 and 4.3. Section 4.4.1 presents the final sheet discretisation and section 4.4.2 presents the final conditions, considering the contact search and friction model.

4.4.1 METAL SHEET DISCRETISATION

Roll penetration results in a longitudinal and transverse sheet bending that need to be described with accuracy. Because of that bending, three elements through the thickness were used, as shown in Figure 4.101. The number of elements used results from the study presented in Chapter 4.1.3.

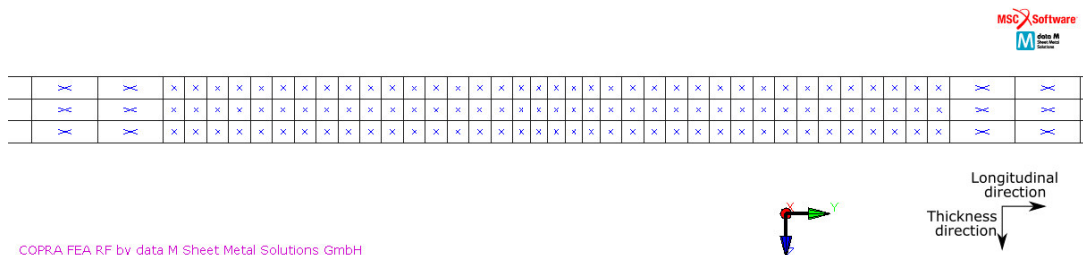


Figure 4.101 - Sheet discretisation in its thickness.

The contact zone needs a good discretisation since the contact is this investigation scope and pays a key role in the sheet final shape. In the zone predicted to be in contact – referred as

possible contact zone – were used elements with a size of 0.333 mm . The elements size results from the study outlined in chapter 4.1.1. This contact zone refinement and the transition mesh are represented in Figure 4.102.

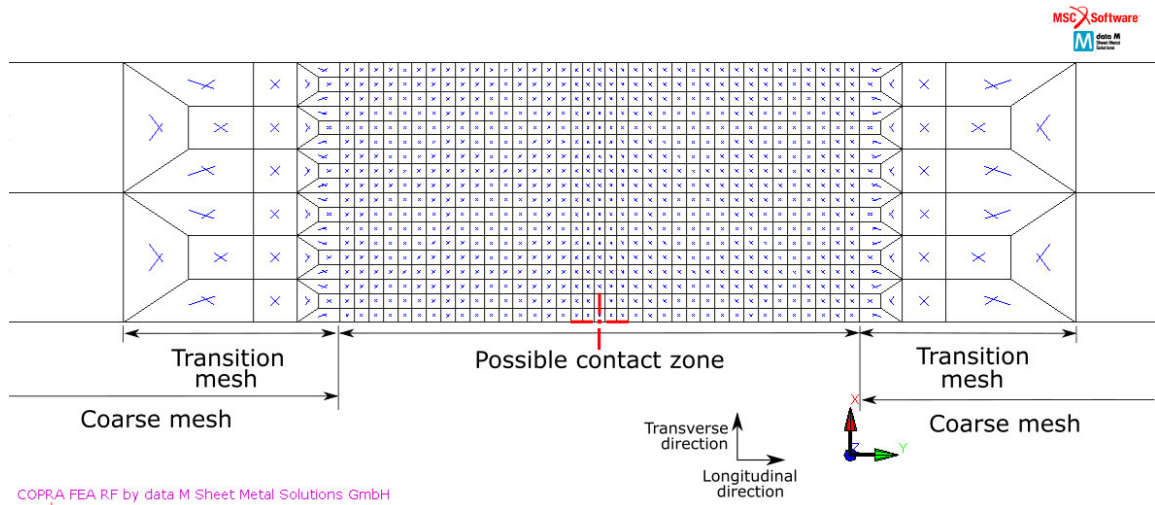


Figure 4.102 - Contact zone mesh refinement and correspondent transition

To improve the location of the node related to the roll axis, a refinement was made in the centre of the sheet. As a result of this refinement, the nodes are not in line with the roll axis and a finer mesh is obtained in the centre. This refinement results from the study outlined in chapter 4.1.5. The four nodes in the centre are changed by five nodes leading to a length size of 0.267 mm for the five nodes in the centre. This refinement and the dimension of the nodes in the centre are shown in Figure 4.103.

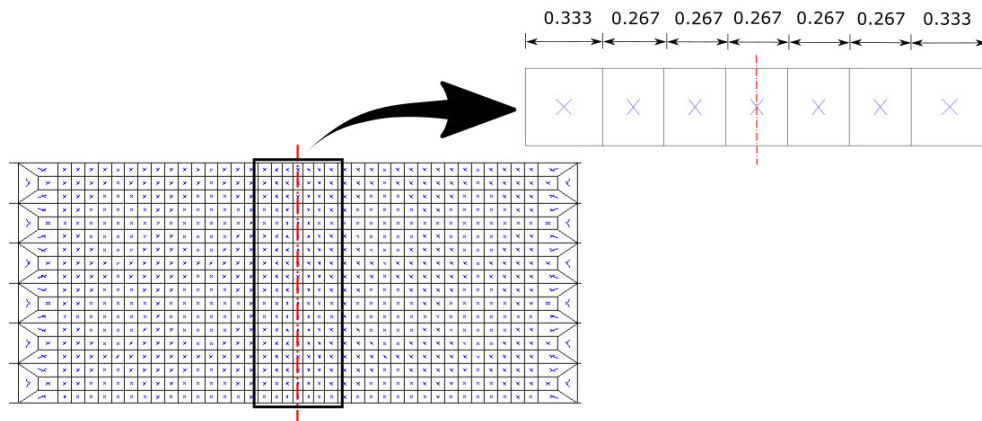


Figure 4.103 - Sheet centre mesh refinement.

4.4.2 CONTACT CONDITIONS

The contact conditions are divided into contact search and friction modeling. The contact search parameters were studied in chapter 4.2 Contact search definition and a final contact distance tolerance of 0.01 and a bias factor of 0.90 were defined. The friction model adopted was an arctangent Coulomb model with a relative velocity threshold of 1 (Figure 4.104).

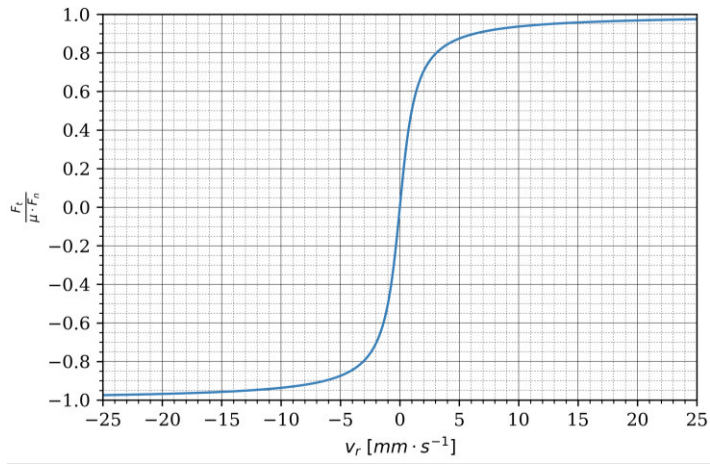


Figure 4.104 - Arctangent Coulomb friction law implemented in the model.

5 CONCLUSIONS AND FUTURE PERSPECTIVES

A main purpose of this work has been the study and the numerical representation of the contact interaction between rolls and sheet in the tribological experiment. This chapter presents the conclusions of the study carried out.

5.1 CONCLUSIONS

The mesh discretisation, the contact search and the friction modelling influence the contact representation in different ways. The mesh discretisation has a major influence on the contact normal stress distribution. The longitudinal and transverse bending geometry is not influenced by the discretisation of the possible contact zone in the longitudinal and transverse directions. The roll force is not influenced by this discretisation, either. However, the contact normal stress is highly influenced. The maximum contact normal stress evolution only tends to converge for a mesh size lower or equal than 0.333 mm and it is only represented accurately when a mesh equal or lower than 0.333 mm is used.

The longitudinal bending and transverse bending are highly influenced by the thickness discretisation. In turn, the bending representation influences the contact normal stress distribution and the roll force needed to move the roll against the sheet. When more elements are used along the thickness, a clear different bending curvature is observed. Similarly, the contact normal stress distribution also shows differences. However, these differences are barely indistinguishable when at least three elements are used along the thickness. Additionally, a clear improvement of the contact normal stress distribution is accomplished when low aspect ratio elements are used in the discretisation of the possible contact zone. Thus, the optimal discretisation should minimize the differences between the longitudinal, transverse and thickness dimensions of the elements.

The nodes location with the roll axis has a significant influence on the results. The nodes in the sheet central line - consequently in line with the roll axis - are not stable and displacements

in the longitudinal direction occur. These displacements create a relative motion between the surfaces that originates a torque on the roll. A location of the elements with its middle plane in line with the roll axis ensure the longitudinal symmetry, and no torque is induced by the nodes instability.

The contact search influences the numerical stability and the computation time. The distance tolerance and bias factor that define the contact search algorithm has an important influence on the number of nodes in contact. Within all different studied contact distance tolerances and bias factors, the number of nodes in contact converged to the same value. However, when the roll starts rotating the torque does not converge immediately, neither the maximum contact normal stress. This behaviour is observed for a distance tolerance between 0.02 and 0.05 with a bias factor of 0.95, and a distance tolerance of 0.01 with a bias factor of 0.90. After these initial oscillations, the value converges immediately. These oscillations do not influence the contact normal stress distribution, which suggests that the contact search influences mainly the numerical stability and would have a bigger influence if the sliding velocity was not constant.

The friction does not influence the longitudinal bending, however, the same is not valid for the transverse bending. This shows a slightly different geometry when friction is taken into account in the calculations. The roll force is also coincident during the penetration phase, even though it exhibits a slight lower roll force in the model with friction when the roll begins rotating. On the other hand, the contact normal stress is significantly influenced by the friction. Thus, the friction influences mainly the contact representation and has a minimal influence on the bending geometry. When comparing a Coulomb bilinear model with an arctangent model it was concluded that the friction model influences mainly the contact normal stress and the friction stress.

5.2 FUTURE PERSPECTIVES

The outlined conclusions are an essential first step for the numerical representation of the contact in a roll forming process. However, further investigation needs to be developed. Regarding the contact search, a model with nodes entering in contact and separating should be developed to further investigate this topic. Thus, a similar model, but with rolling along the sheet should be used to check the simulation stability and to study the separations criterion.

In order to implement the studied mesh discretisations, implementation schemes need to be developed. The sheet geometry is already represented with accuracy with a standard roll forming mesh and only torque calculations are the target. Thus, a feasible alternative would be to stop the simulation and remesh the sheet. A certain number of increments would run with a finer mesh in order to calculate the roll torque. After the calculation, the simulation would proceed with the standard roll forming mesh. Elements with higher interpolation functions should also be investigated. Higher interpolation functions, ensure a better boundary continuity, therefore, a smaller number of elements could be enough to represent the contact with accuracy.

As previously mentioned in section 2.2.4, ideally the friction coefficient would be calculated as a function of the contact normal stress, relative sliding velocity and temperature. In roll forming the temperature is not important, however, the contact normal stress and the relative velocity are continuously changing. Thus, if an accurate torque calculation is required, these parameters need to be taken into account and a friction coefficient calculation model needs to be implemented. A subroutine needs to be developed and implemented.

Given the complexity of the roll forming process and the contact interaction, validation is difficult to perform. However, without a validation it is not possible to be sure if the results are accurate. Thus, once the mesh discretisation has been implemented, the friction models need to be validated. For that purpose, one station process would be experimentally studied. The roll torque and sheet velocity would be measured and compared with the torque and velocity calculated numerically in order to validate and define an accurate friction model.

6 REFERENCES

- ABEE, ANDRÉ, ALBERT SEDLMAIER, AND CARL STEPHENSON. 2010. "Development of New 3D Roll Forming Applications by Means of Numerical Analysis as a Part of a Quality Control Methodology". *CBM Metal Matters*, no. 18: 21–24
- APOSTOLOS, FYSIKOPOULOS, PAPACHARALAMPOPOULOS ALEXIOS, AND PASTRAS GEORGIOS. 2013. "Energy Efficiency of Manufacturing Processes: a Critical Review". *Procedia CIRP* 7. Elsevier B.V.: 628–33
- BOMAN, R., L. PAPELEUX, AND J. P. PONTHOT. 2007. "A General Arbitrary Lagrangian Eulerian Formulation for the Numerical Simulation of 3D Forming Processes". In *NUNIFORM '07, Materials Processing and Design: Modeling, Simulation and Applications*, edited by J. M. A. Cesar de Sá and Abel D. Santos. American Institute of Physics
- BUI, Q. V., AND J. P. PONTHOT. 2008. "Numerical Simulation of Cold Roll-Forming Processes". *Journal of Materials Processing Technology* 202 (1–3): 275–82
- DATA M SMS. 2012. "History of Data M: Data M". Accessed July 2017. <http://www.datam.de/en/about-data-m/history-of-data-m/>.
- DUGGAL, NITIN, MUSTAFA A. AHMETOGLU, GARY L. KINZEL, AND TAYLAN ALTAN. 1996. "Computer Aided Simulation of Cold Roll Forming — a Computer Program for Simple Section Profiles". *Journal of Materials Processing Technology* 59 (1–2): 41–48
- FERREIRA, PEDRO B. 2016. "Roll Forming - a Study on Machine Deflection by Means of Experimental Analysis and Numerical Developments". MSc Thesis. Faculty of Engineering, University of Porto
- FERREIRA, PEDRO B., MIGUEL S. PEREIRA, THOMAS DIETL, ALBERT SEDLMAIER, AND ABEL D. SANTOS. 2016. "Perfilagem a Frio e a Importância do Uso de Software Especializado na Indústria". *Tecnometal*
- FILZEK, J., AND M. LUDWIG. 2013. "Berücksichtigung Der Reibung in Der FEM-Simulation". *Tagungsband TB-036 Des EFBKolloquiums Blechverarbeitung*
- FLOW SCIENCE. 2017. "Implicit vs Explicit Numerical Methods". Accessed July 2017. <https://www.flow3d.com/resources/cfd-101/numerical-issues/implicit-versus-explicit-numerical-methods/>.
- GALDOS, L., U. ULIBARRI, E. SAENZ DE ARGANDOÑA, J. MENDIGUREN, AND A. ZABALA. 2017. "Friction Coefficient Identification in Roll Forming Processes". *Manufacturing Integrated Design - Final Colloquium CRC 666*
- GÜLÇEKEN, E., A. ABEE, A. SEDLMAIER, AND H. LIVATYALI. 2007. "Finite Element Simulation of Flexible Roll Forming : A Case Study on Variable Width U Channel". In *4th International Conference*

and Exhibition on Design and Production of Machines and Dies/Molds, 21–23. Turkey

- HALMOS, GEORGE T. 2006. *Roll Forming Handbook (Manufacturing Engineering and Materials Processing)*. Edited by Geoffrey Boothroyd. CRC Press Taylor & Francis Group
- HOL, J., J.H. WIEBENGA, M. HÖRNING, F. DIETRICH, AND C. DANE. 2016. “Advanced Friction Simulation of Standardized Friction Tests: A Numerical and Experimental Demonstrator”. *NUMISHEET 2016: 10th International Conference and Workshop on Numerical Simulation of 3D Sheet Metal Forming Processes*. Journal of Physics: Conference Series
- HONG, SUKMOO, SEUNGYOON LEE, AND NAKSOO KIM. 2001. “A Parametric Study on Forming Length in Roll Forming”. *Journal of Materials Processing Technology* 113 (1–3): 774–78
- INGARAO, GIUSEPPE. 2017. “Manufacturing Strategies for Efficiency in Energy and Resources Use: The Role of Metal Shaping Processes”. *Journal of Cleaner Production* 142. Elsevier Ltd: 2872–86
- JOHNSON, K. L. 1985. *Contact Mechanics*. Cambridge: Cambridge University Press
- JOUN, M. S., H. G. MOON, I. S. CHOI, M. C. LEE, AND B. Y. JUN. 2009. “Effects of Friction Laws on Metal Forming Processes”. *Tribology International* 42 (2): 311–19
- KIM, NAM-HO. 2015. *Introduction to Nonlinear Finite Element Analysis*. Springer
- KLOCKE, F., D. TRAUTH, A. SHIROBOKOV, AND P. MATTFELD. 2015. “FE-Analysis and in Situ Visualization of Pressure-, Slip-Rate-, and Temperature-Dependent Coefficients of Friction for Advanced Sheet Metal Forming: Development of a Novel Coupled User Subroutine for Shell and Continuum Discretization”. *International Journal of Advanced Manufacturing Technology* 81 (1–4): 397–410
- LAURSEN, T. A. 2002. *Computational Contact and Impact Mechanics: Fundamentals of Modeling Interfacial Phenomena in Nonlinear Finite Element Analysis*. Berlin: Springer-Verlag
- LINDGREN, MICHAEL. 2007. “Experimental Investigations of the Roll Load and Roll Torque When High Strength Steel Is Roll Formed”. 191: 44–47
- data M. 2015. *COPRA® RF and COPRA® FEA RF Workbook*. Manual. Munich: data M Sheet Metal Solutions GmbH.
- MARCINIAK, Z., J. L. DUNCAN, AND S. J. HU. 2002. *Mechanics of Sheet Metal Forming*. Second edi. London: Butterworth-Heinemann
- MSC SOFTWARE. 2013. “Contact Analysis Using MSC.Marc”. Santa Clara, CA: MSC Software Corporation
- MSC Software. 2016a. “Marc® 2016 User Manual Volume A: Theory and User Information” Manual. Santa Clara, CA: MSC Software Corporation. Manual
- MSC Software. 2016b. “Marc® 2016 User Manual Volume B: Element Library”. Manual. Santa Clara, CA: MSC Software Corporation
- NETO, D.M. 2014. “Numerical Simulation of Frictional Contact Problems Using Nagata Patches in Surface Smoothing.” PhD Thesis, University of Coimbra
- NOELS, L., L. STAINIER, AND J. P. PONTHOT. 2004. “Combined Implicit/explicit Time-Integration Algorithms for the Numerical Simulation of Sheet Metal Forming”. *Journal of Computational and Applied Mathematics* 168 (1–2): 331–39
- OLIVEIRA, M.C. 2005. “Algoritmos E Estratégias de Gestão Do Problema de Contacto Com Atrito Em Grandes Deformações - Aplicação à Estampagem de Chapas Metálicas”. PhD Thesis. University of Coimbra
- OLIVER, J., A. E. HUESPE, AND J. C. CANTE. 2008. “An Implicit/explicit Integration Scheme to Increase Computability of Non-Linear Material and Contact/friction Problems”. *Computer Methods in Applied Mechanics and Engineering* 197 (21–24): 1865–89

- OÑATE, EUGENIO. 2009. *Structural Analysis with the Finite Element Method. Linear Statics. Volume 1. Basis and Solids*. Springer
- RODRIGUES, JORGE, AND PAULO MARTINS. 2010. *Tecnologia Mecânica Vol. 2 - Tecnologia Da Deformação Plástica*. Escolar Editora
- SANTOS, A., MAKINOUCI A. 1995. "Contact Strategies to Deal with Different Tool Descriptions in Static Explicit FEM for 3D Sheet Metal Forming Simulation". *Journal of Materials Processing Technology* 50 (1-4): 277-291
- SERVROLL. 2017. "SERVROLL - Innovative Research Project." Accessed June 2017. <https://www.servroll.eu/>.
- SHROUF, F, J ORDIERES, AND G MIRAGLIOTTA. 2014. "Smart Factories in Industry 4 . 0: A Review of the Concept and of Energy Management Approached in Production Based on the Internet of Things Paradigm". In *2014 IEEE International Conference on Industrial Engineering and Engineering Management*, 697-701
- SWIFT, H. W. 1952. "Plastic Instability under Plane Stress". *Journal of Mechanics and Physics of Solids* 1: 1-18
- TAYLOR, R., AND P. PAPADOPOULOS. 1991. "On a Patch Test for Contact Problems in Two Dimensions". *Computational Methods in Nonlinear Mechanics*. Springer-Verlag
- TIMOSHENKO, STEPHEN P., AND JAMES M. GERE. 1991. *Mechanics of Materials*. Third edit. Champman & Hall
- WRIGGERS, P. 2006. *Computational Contact Mechanics*. Second edition. Springer
- WRIGGERS, P., T. VU VAN, AND E. STEIN. 1990. "Finite Element Formulation of Large Deformation Impact-Contact Problems with Friction". *Computers & Structures* 37 (3): 319-31
- YASTREBOV, VLADISLAV A. 2013. *Numerical Methods in Contact Mechanics*. John Wiley & Sons
- ZENG, G., S. H. LI, Z. Q. YU, AND X. M. LAI. 2009. "Optimization Design of Roll Profiles for Cold Roll Forming Based on Response Surface Method". *Materials and Design* 30: 1930-38